

TOWARDS MODELLING PHYSICAL AND CHEMICAL
EFFECTS DURING WETTABILITY ALTERATION IN
CARBONATES AT PORE AND CONTINUUM SCALES

YAN ZARETSKIY

A thesis submitted for the degree of
Doctor of Philosophy

Heriot-Watt University
Institute of Petroleum Engineering
May 2012

The copyright in this thesis is owned by the author. Any quotation from the thesis or use of any of the information contained in it must acknowledge this thesis as the source of the quotation or information.

To my wife Inga and our son Anton

ABSTRACT

Understanding what controls the enhanced oil recovery during water-flooding of carbonate rocks is essential as the majority of the world's remaining hydrocarbon reserves are contained in carbonate rocks. To further this understanding, in this thesis we develop a pore-scale simulator that allows us to look at the fundamental physics of fluid flow and reactive solute transport within the porous media. The simulator is based on the combined finite element – finite volume method, it incorporates efficient discretization schemes and can hence be applied to porous domains with hundreds of pores. Our simulator includes the rule-based method of accounting for the presence of the second immiscibly trapped fluid phase. Provided that we know what chemical conditions initiate enhanced oil recovery, our simulator allows us to analyse whether these conditions occur, where they occur and how they are influenced by the flow of the aqueous phase at the pore scale. To establish the nature of chemical interactions between the injected brines and the carbonate rocks, we analyze the available experimental data on the single-phase coreflooding of carbonate rocks. We then build a continuum scale simulation that incorporates various chemical reactions, such as ions adsorption and mineral dissolution and precipitation. We match the output of the continuum scale model with the experimental data to identify what chemical interactions the ions dissolved in seawater are involved in.

PUBLICATIONS

Besides unpublished material this thesis contains excerpts from the following peer-reviewed papers:

1. Y. Zaretskiy, S. Geiger, K. S. Sorbie, and M. Förster. Efficient flow and transport simulations in reconstructed 3D pore geometries. *Advances in Water Resources*, 33(12):1508-1516, 2010.
2. Y. Zaretskiy, S. Geiger, and K. S. Sorbie. Direct numerical simulation of pore-scale reactive transport: applications to wettability alteration during two-phase flow. *International Journal of Oil, Gas and Coal Technology*, in press.
3. S. Geiger, K. S. Schmid, and Y. Zaretskiy. Mathematical analysis and numerical simulation of multi-phase multi-component flow in heterogeneous porous media. *Current Opinion in Colloid and Interfacial Sciences*, in press.

Nothing in the world can take the place of persistence. Talent will not; nothing is more common than unsuccessful men with talent. Genius will not; unrewarded genius is almost a proverb. Education will not; the world is full of educated derelicts. Persistence and determination alone are omnipotent.

— CALVIN COOLIDGE

ACKNOWLEDGMENTS

The past nearly four years have been a tough journey. I have questioned myself on numerous occasions as to whether I am doing the right thing retaining my student status for so long. Now I finally see the fruits of my labour and I realize that it was a path worth taking. But I could not have done it without the help of all the wonderful people around me.

First and foremost, I wish to express my deepest gratitude to Sebastian Geiger. Your guidance and occasional therapeutical discussions helped me not to let the bitterness of the CSMP++ coding get the best of me! I admire your willingness to get to the tiniest scientific details of your students' problems when they sometimes get stuck. There is a reason why you are the only professor at the Heriot-Watt University with a fan club!

I am also grateful to Ken Sorbie, a mastermind behind this thesis, setting the directions of my research ventures. Your advice on how to write the rebuttal letters to angry reviewers was invaluable!

I thank Andrey Ryazanov and his wife Tanya for giving me a tour around Edinburgh during my first day in this wonderful city. I thank Vasily Demyanov for leaving his business card at my desk on my first day at the IPE. I thank Khafiz Muradov for giving me an opportunity to be a tutor for the Well Completion course.

I was honoured to share my office with some truly amazing chaps. Karen, I would not have been able to keep my working standards high without you. Claudia, thank you for inviting me to all those parties and gatherings that you have been organizing and I am sorry for being such a bore! Christine, you are the best coffee mate ever! And I am so glad you share a fondness for heavy metal music with me. Robert, it is a pleasure to exist on the same planet as you, your optimism is boundless. I sure hope to have another Super Street Fighter IV session with you. Shanti,

thank you for your kindness and revealing to me the existence of lassi. Adnan, as promised – I am sorry for periodically not letting you meditate over your code. You demonstrated a great mastery of patience in bearing me! Mohamed, thank you for listening to all my political rants. I wish the best to your child! Chen, thank you for your mind-boggling stories about the computer hackers. Good luck with that Chinese-English dictionary you keep, I have been keeping mine for almost two years before I gave up trying to learn every new English word I came across! Matteo, it is a pity you left Edinburgh before my graduation, you've been a wonderful friend and a mood-setter of our office ambiance.

While doing a PhD course in Edinburgh, I was given an opportunity to have a four months break in Houston, Texas, to do an internship at ExxonMobil. This was a timely offer, reminding me of what lies ahead of a PhD path. For this I am indebted to Thomas Willingham, who made this internship possible. I thank Lindsey Gulden and Stephen Kaczmarek for turning it into a truly wonderful experience. I thank Susan Agar for constantly reminding me to think about the business applications of my project! This work would not have seen the light of day without the funding by the FC² Research Alliance that Susan leads.

Literally nothing in my life would have been possible without the care and affection of my parents. Thank you for giving me the opportunity to become who I am.

My life since what now seems like time immemorial has been inextricably linked with my amazing wife Inga. It is impossible to thank you enough and I humbly dedicate this thesis to you and our baby Anton.

Edinburgh, March 2012

ACADEMIC REGISTRY

Research Thesis Submission



Name:	Yan Zaretskiy		
School/PGI:	IPE		
Version: <i>(i.e. First, Resubmission, Final)</i>	First	Degree Sought (Award and Subject area)	PhD in Petroleum Engineering

Declaration

In accordance with the appropriate regulations I hereby submit my thesis and I declare that:

- 1) the thesis embodies the results of my own work and has been composed by myself
- 2) where appropriate, I have made acknowledgement of the work of others and have made reference to work carried out in collaboration with other persons
- 3) the thesis is the correct version of the thesis for submission and is the same version as any electronic versions submitted*.
- 4) my thesis for the award referred to, deposited in the Heriot-Watt University Library, should be made available for loan or photocopying and be available via the Institutional Repository, subject to such conditions as the Librarian may require
- 5) I understand that as a student of the University I am required to abide by the Regulations of the University and to conform to its discipline.

* Please note that it is the responsibility of the candidate to ensure that the correct version of the thesis is submitted.

Signature of Candidate:		Date:	16/03/2012
-------------------------	--	-------	------------

Submission

Submitted By <i>(name in capitals)</i> :	Yan Zaretskiy
Signature of Individual Submitting:	
Date Submitted:	16/03/2012

For Completion in the Student Service Centre (SSC)

Received in the SSC by <i>(name in capitals)</i> :			
Method of Submission <i>(Handed in to SSC; posted through internal/external mail):</i>			
E-thesis Submitted (mandatory for final theses)			
Signature:		Date:	

Please note this form should bound into the submitted thesis.

Updated February 2008, November 2008, February 2009, January 2011

CONTENTS

1	INTRODUCTION	1
1.1	Waterflooding efficiency as a function of brine composition	3
1.2	Pore-scale modelling	12
1.3	Structure of the thesis	21
2	PORE-SCALE MODELLING OF INERT TRANSPORT	23
2.1	Introduction	23
2.2	Numerical methods	25
2.2.1	Continuous formulation of fluid flow equations . .	25
2.2.2	Weak form of Stokes equation	27
2.2.3	Discrete form of Stokes equations	29
2.2.4	Benchmarking against analytical solution	31
2.2.5	Combined FE-FV method for advection-diffusion equation	33
2.2.6	Algebraic multigrid method	36
2.2.7	Parallel discretization	39
2.2.8	Mesh generation	40
2.3	Method application	43
2.3.1	Reconstructed 3D meshes	43
2.3.2	Pressure and velocity profiles	44
2.3.3	Solute transport	47
2.4	Summary	54
3	PORE-SCALE MODELLING OF REACTIVE TRANSPORT	56
3.1	Introduction	56
3.2	Numerical method	59
3.2.1	Chemical reactions	60
3.2.2	Distance field calculation	62
3.3	Example application	73
3.4	Summary	79
4	CONTINUUM-SCALE MODELLING OF REACTIVE TRANSPORT	82
4.1	Introduction	82
4.2	Review of published experimental data	83

4.2.1	Remarks on the published data	91
4.3	Numerical model	92
4.3.1	Aqueous chemistry	92
4.3.2	Surface adsorption	94
4.3.3	Mineral dissolution and precipitation	96
4.4	Modelling results	97
4.4.1	Fixed parameters	98
4.4.2	Fitting parameters and numerical breakthrough curves	99
4.4.3	Outlook for two-phase flow problems	111
4.5	Summary	112
5	SUMMARY, CONCLUSIONS AND FUTURE WORK	116
5.1	Summary and conclusions	116
5.2	Future work	119
	BIBLIOGRAPHY	122

LIST OF FIGURES

Figure 1.1	Oil recovery during spontaneous imbibition experiments	5
Figure 1.2	Conjectural oil recovery mechanisms in sandstones and carbonates	6
Figure 1.3	Idealized representation of the mechanism of oil recovery due to calcite dissolution	8
Figure 1.4	Experimental oil recovery during coreflooding in carbonates	9
Figure 1.5	A 2D slice from the CT image of a sandstone sample	13
Figure 1.6	A 3D CT image of a porous rock and a corresponding pore network	17
Figure 1.7	Organization of the thesis	22
Figure 2.1	Solution of the Poiseuille flow in 2D	25
Figure 2.2	Velocity and pressure error in L_2 -norm versus characteristic element size h	32
Figure 2.3	A simple 2D finite element mesh with the complementary finite volume facets	34
Figure 2.4	Criterion for choosing the time step for the transport calculations	36
Figure 2.5	Schematic representation of a multigrid cycle	37
Figure 2.6	Partitioning of a finite element mesh in 2D	39
Figure 2.7	Partitioning of a 3D tetrahedral mesh	40
Figure 2.8	Conversion of computed tomography data into a finite element tetrahedral mesh	41
Figure 2.9	Two-manifold and non-manifold surfaces	42
Figure 2.10	Relation between initial and smooth isosurfaces	43
Figure 2.11	Fluid pressure and velocity profiles in 3D	44
Figure 2.12	Velocity magnitude distribution across a 2D model of a grainstone sample	46
Figure 2.13	Flux-weighted breakthrough curves corresponding to low and high Peclet numbers	49
Figure 2.14	Dimensionless dispersivity plots	51

Figure 3.1	A 2D finite element mesh with 1D “surface” elements and complementary finite volume facets . .	59
Figure 3.2	Distance field computed as a solution of various numerical cases	66
Figure 3.3	Plot of distance field along a line for different numerical methods	67
Figure 3.4	Solutions of Eikonal equation on a 1D domain $\Omega = [0; 1]$	68
Figure 3.5	Distance and radii fields for a 2D model	72
Figure 3.6	Phase distribution snapshot for a 2D model	73
Figure 3.7	Solute concentration profiles within the 3D pore space	74
Figure 3.8	Effects of adsorption of concentration profile and surface coverage	75
Figure 3.9	A distribution of the solute concentration together with the oil blobs	76
Figure 3.10	Breakthrough curves for reactive transport with and without the presence of oil	78
Figure 4.1	Experimental SO_4^{2-} and Ca^{2+} breakthrough curves as reported by Strand et al. (2006)	85
Figure 4.2	Experimental SO_4^{2-} breakthrough curves for various $\text{Ca}^{2+}/\text{SO}_4^{2-}$ ratios as reported by Strand et al. (2006)	86
Figure 4.3	Experimental Ca^{2+} breakthrough curves as reported by Zhang et al. (2007)	88
Figure 4.4	Experimental Ca^{2+} breakthrough curves during seawater injection as reported by Zhang et al. (2007)	89
Figure 4.5	Experimental breakthrough curves as reported by Madland et al. (2011)	90
Figure 4.6	Experimental and modelled SO_4^{2-} and Ca^{2+} breakthrough curves	102
Figure 4.7	Simulated evolution of surface potential	103
Figure 4.8	Experimental and modelled SO_4^{2-} breakthrough curves for various $\text{Ca}^{2+}/\text{SO}_4^{2-}$ ratios	104
Figure 4.9	Experimental and modelled Ca^{2+} and Mg^{2+} breakthrough curves during CF-M brine injection	105
Figure 4.10	Experimental and modelled Ca^{2+} breakthrough curves during seawater injection	106

Figure 4.11	Experimental and modelled breakthrough curves during MC brine and seawater injection	107
Figure 4.12	[>COO ⁻][>CaOH ⁺] product for calcite/seawater system and varying SO ₄ ²⁻ levels	112

LIST OF TABLES

Table 1.1	Summary of controlled-salinity experiments	10
Table 1.2	Summary of controlled-salinity experiments (cont.)	11
Table 1.3	Summary of controlled-salinity experiments (cont.)	12
Table 2.1	Permeability values obtained experimentally and from different numerical models.	47
Table 4.1	Ionic compositions of brines used for coreflood experiments by Strand et al. (2006).	84
Table 4.2	Ionic compositions of brines used for coreflood experiments by Zhang et al. (2007)	87
Table 4.3	Ionic compositions of brines used for coreflood experiments by Madland et al. (2011)	91
Table 4.4	Coefficients in Eq. 4.11 for the relevant thermodynamic solubility products.	99
Table 4.5	Summary of fitting parameters of the continuum-scale reactive transport model	100

INTRODUCTION

Production of hydrocarbons from oil reservoirs typically occurs in up to three distinct phases: primary, secondary and tertiary, or enhanced, recovery. During primary recovery, the oil flow is driven by the natural reservoir energy, such as gravity drainage or waterdrive, into the wellbore and is brought up to the surface with artificial lift techniques, i.e. pumps. Typically, only about 4-8% of the reservoir's original oil in place (OOIP) is produced during this stage. During the secondary recovery stage an external fluid, such as water, is injected into the reservoir through injection wells to maintain the system pressure and displace oil toward the production well, resulting in the recovery of 20-40% of the OOIP. The limit of this stage is reached when the injected fluid is produced in considerable amounts from the production wells, rendering the production of oil uneconomical. The final stage, which can in fact be initiated even before the secondary recovery is over, includes sophisticated methods that alter the oil or rock properties in a way that further improves the recovery of hydrocarbons.

Naturally fractured carbonate reservoirs comprise a particularly challenging group of reservoirs to produce, while containing more than 60% of the world's oil reserves (Schlumberger, 2007). About 90% of carbonate reservoirs are characterized as neutral-wet to preferentially oil-wet. Moreover, the carbonate matrix permeability usually lies in the millidarcy (mD) range. As a consequence, conventional waterflooding of extensively fractured carbonate rocks can recover as low as 10% of the OOIP. This is because water bypasses matrix blocks due to the typically high permeability contrast between them and the fractures. At the same time, spontaneous imbibition of water into the matrix blocks is slow in mixed-wet or non-existent in oil-wet rocks due to the unfavourable pore-scale capillary pressure, $P_c < 0$, which has to be overcome for water to displace oil from the oil-wet pores. It is, therefore, particularly important to develop enhanced oil recovery (EOR) techniques that can be utilized to improve the performance of carbonate reservoirs, for example

by increasing the spontaneous imbibition rate which will lead to a better sweep of the reservoir during the waterflooding process.

One of the more popular EOR techniques in carbonates is CO₂ flooding (Manrique et al., 2004). CO₂ is miscible with oil above a certain pressure and reduces its viscosity during the flooding process. The key problem in applying this technique is the fact that CO₂ projects are usually tied to the availability of natural CO₂ sources and transporting pipelines relatively close to the oilfields subject to this procedure.

Alternative EOR methods include improving the outcome of the waterflooding itself, which usually implies modification of the composition of injected fluid in a way that triggers the liberation of oil from the rock. This may happen due to brine-rock interactions that engender local wettability changes towards more water-wet conditions. As will be discussed in more detail below, existing experimental evidence suggests that the presence of certain ionic species in the injected water facilitates the oil recovery. However, little work has been done to formalize these results and infer the exact link between the ionic transport and the two-phase flow properties of the rock. Therefore, in this work we aim, as a first step, to determine exactly what physicochemical mechanisms lead to the enhancement of oil recovery during the waterflooding procedure. Secondly, we wish to evaluate how these mechanisms are translated into the continuum-scale description of the two-phase fluid flow, i.e. their influence on the capillary pressure and relative permeability curves.

Numerical simulations of the relevant phenomena are employed to reach these goals and this thesis essentially covers our work towards the first objective, namely a *numerical investigation of the mechanisms that facilitate the oil release from carbonate rocks during waterflooding*. Given the wide scope of this mechanistic remit, we investigate a range of approaches both at the pore level and at the continuum scale. In outline, the work programme in this thesis examines the following areas of investigation:

1. Pore-scale modelling of the fluid velocity distribution within the porous sample using the grid-based finite element (FE) method. This procedure is necessary for the subsequent modelling of the transport of dissolved ions as the velocity with which they are advected is calculated as a result of this step. It also allows us to calculate the sample permeability directly from the pore geometry data.

2. Pore-scale modelling of the inert solute transport based on the finite element – finite volume method. In this step we consider how the solute is propagated within the porous sample subject to convection and diffusion. No chemical interactions are considered at this point. This procedure enables us to directly calculate the dispersivity of a porous sample.
3. Extension of the solute transport to account for the arbitrary chemical reactions within the aqueous phase or between the brine and the mineral phase. This step also describes the way to simulate the phenomenon of surface diffusion along the fluid-solid interfaces within the finite element – finite volume framework.
4. Rule-based method of accounting for the presence of the second immiscibly trapped fluid phase. Provided that we know what chemical conditions trigger the wettability change, this method allows us to use pore-scale modelling to analyse whether these conditions occur, where they occur and how they are influenced by the flow of the aqueous phase.
5. Finally, we analyse the available experimental data on the chemical interaction between the injected fluids and the carbonate rocks. We then build a continuum scale simulation that incorporates various chemical reactions, such as ions adsorption and mineral dissolution and precipitation. We match the output of the continuum scale model with the experimental data to identify what chemical interactions the ions dissolved in seawater are involved in.

The second objective of this work is a subject of extensive research in its own right as there are presently no established procedures to establish the effects of the reactive solute transport on the continuum-scale properties of the two-phase flow. We reserve this topic for the future work, as indicated in Section 5.2.

1.1 WATERFLOODING EFFICIENCY AS A FUNCTION OF BRINE COMPOSITION

In the last 15 years it has been demonstrated that the waterflooding efficiency *in sandstones* is affected by the brine's ionic composition (Yildiz

and Morrow, 1996). Lager et al. (2008) proposed that, in sandstones, oil components are bound to the surface of oil-wet materials, such as clays, by cation bridging (RCOO-M-surface , where M is a multivalent cation). If the salinity of the surrounding water is low enough, the electrical double layer at the clay surface expands and the bound multivalent cations become accessible for the monovalent cations dissolved in the water. The resulting ion exchange releases the organic complexes and changes the surface wettability.

The impact of brine ionic composition on oil recovery *from carbonate rocks* has also been studied recently. The interest in this topic was kindled by an outcome of the waterflooding programme conducted in the Ekofisk oilfield in the North Sea in the beginning of 1980s. The resulting oil displacement by seawater proved to be more effective than expected. This finding was followed by a series of ongoing laboratory studies.

As spontaneous imbibition is a crucial oil-displacing phenomena in fractured reservoirs, the majority of experimental studies so far have concentrated on its sensitivity to the brine composition. It was demonstrated by Standnes and Austad (2000b) that cationic surfactants of the tetra alkyl ammonium type can act as a wettability modifier and initiate the spontaneous imbibition of a brine into an initially oil-wet chalk core. Subsequently it was found by Strand et al. (2003) that the presence of SO_4^{2-} ion in addition to the same type of cationic surfactants further improves the recovery by spontaneous imbibition. It was then shown by Zhang and Austad (2005) that sulphate can change wettability even when no surfactant is present. Further research (Strand et al., 2006; Zhang et al., 2007) revealed that three divalent ions – SO_4^{2-} , Ca^{2+} and Mg^{2+} – impact on the imbibition process, thus making seawater a promising injection fluid for carbonate (or at least chalk) waterflooding. It was reported that for this impact to occur sulphate had to be dissolved in the brine together with at least one of the positively charged ions and that the presence of SO_4^{2-} and Ca^{2+} had an effect at both low (40 °C) and high (> 90 °C) temperatures, while SO_4^{2-} and Mg^{2+} only worked at high temperatures. The amount of recovered oil was observed to increase with increasing concentration of the relevant ions. Fig. 1.1 demonstrates the sensitivity of the oil recovery to the composition of imbibing brines above 70 °C, as reported by Zhang et al. (2007). It can be seen that the addition of Mg^{2+} significantly improves the recovery as long as SO_4^{2-} is also present

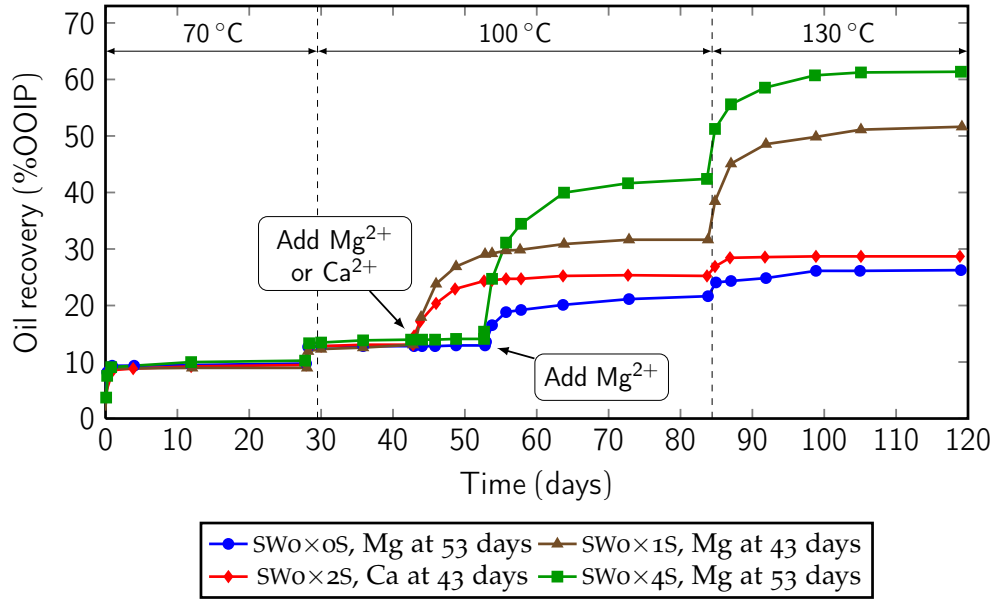


Figure 1.1: Oil recovery during spontaneous imbibition experiments for temperatures above 70 °C reported in (Zhang et al., 2007). Imbibing seawater initially contained no Ca^{2+} and Mg^{2+} ions, which is marked as SWo. Four different concentrations of SO_4^{2-} were used, with n in SWo×nS denoting a multiple of an average seawater concentration of SO_4^{2-} . Calcium or magnesium ions were subsequently added after 43 or 53 days to analyse their influence on oil recovery.

in the brine. It also shows that calcium alone is not enough to trigger the enhanced recovery by the temperature jump above 100 °C.

Probably because sulphate ions were shown to improve the recovery in conjunction with surfactants, it was hypothesized in the above-mentioned studies that these ions act in a similar fashion, i.e. by forming ion-pairs with oil components which are then released from the rock surface, thus locally altering the wettability towards more water-wet conditions. The proposed mechanism posits that the adsorption of SO_4^{2-} onto the chalk surface decreases its initially positive charge, which causes an excess of Ca^{2+} to be attracted to the surface. Ca^{2+} reacts with the negatively charged carboxylic group, $-\text{COO}^-$, and some carboxylic material is removed from the chalk surface. At elevated temperatures Mg^{2+} also becomes active and in the presence of SO_4^{2-} it is proposed to displace calcium-carbonate complexes $[-\text{COOCa}]^+$ from the surface. It is argued that this process does not occur at lower temperatures because under these conditions Mg^{2+} ions are strongly hydrated and are hence unlikely to react. Fig. 1.2 depicts the idealized representation of the wettability alteration mechanisms for both sandstones and carbonates.

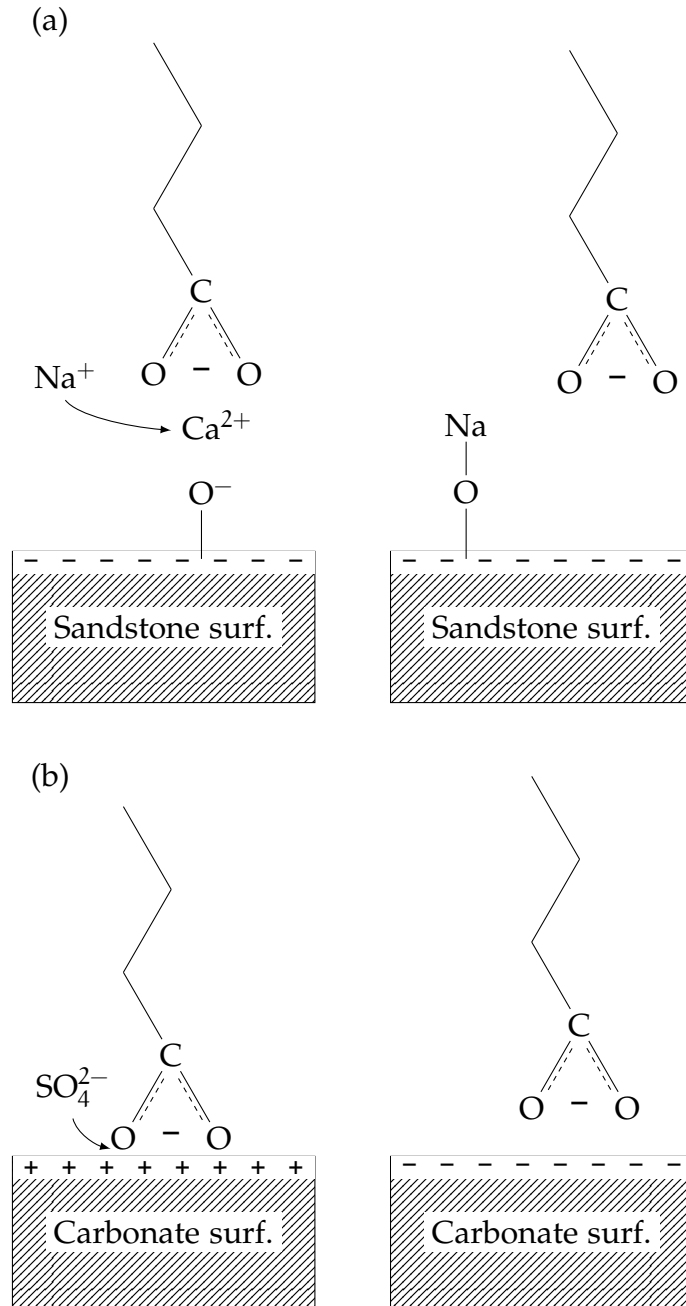


Figure 1.2: Oil recovery mechanisms in (a) sandstones and (b) carbonates proposed in the literature. Lager et al. (2008) proposed that in negatively charged sandstones the wettability changes due to monovalent cations (e.g. Na^+) replacing the divalent cations (e.g. Ca^{2+}), to which the oil components are attached. Strand et al. (2006) suggested that in positively charged carbonates oil components are directly attached to the surface and SO_4^{2-} ions modify the charge leading to local wettability alteration.

An alternative explanation for wettability alteration was proposed by Hiorth et al. (2010a). These workers suggest that, at high temperatures, Ca^{2+} in seawater reacts with SO_4^{2-} and as a result anhydrite is precipitated. Consequently, the aqueous phase loses Ca^{2+} which is then supplied by calcite dissolution. If the rock dissolution takes place at the locations of adsorbed oil, it detaches from the rock surface, hence changing the rock wettability. This mechanism is illustrated in Fig. 1.3. However, this hypothesis does not explain why chalk wettability is altered at lower temperature values (40 °C) at which seawater is not oversaturated with respect to anhydrite. Nevertheless, it was used by Evje and Hiorth (2010) to construct a 1D two-phase model of spontaneous imbibition where the transition between oil-wet and water-wet capillary pressure and relative permeability curves was adjusted with respect to the amount of dissolved calcite:

$$\begin{aligned} H(C) &= [1 + A \cdot \max(C_0 - C, 0)]^{-1}, \\ f(S, C) &= H(C) f^{\text{ww}}(S) + [1 - H(C)] f^{\text{ow}}(S), \end{aligned} \quad (1.1)$$

where

C_0/C (initial) moles of calcite, [mol]

$H(C)$ weighting function

A fitting parameter

$f(S)$ capillary pressure, [Pa], or relative permeability, [–]

In addition, the “ww” and “ow” superscripts denote water-wet and oil-wet conditions respectively. Using this approach, the authors were able to numerically reproduce the observed dependency of the amount of recovered oil on temperature and aqueous concentration of sulphate and magnesium ions. This implies that at least at high temperature chalk dissolution can be one of the factors facilitating oil release during the spontaneous imbibition of seawater.

To finalize the discussion of imbibition experiments, Karoussi and Hamouda (2007) showed that the presence of SO_4^{2-} is not a necessary condition to observe the improved oil recovery and that the recovery strongly depends on the composition of the formation water. However, the samples used in that work were water-wet.

Recently, experimental data on oil recovery during forced brine injection started to appear in the literature. Results presented by Fathi et al.

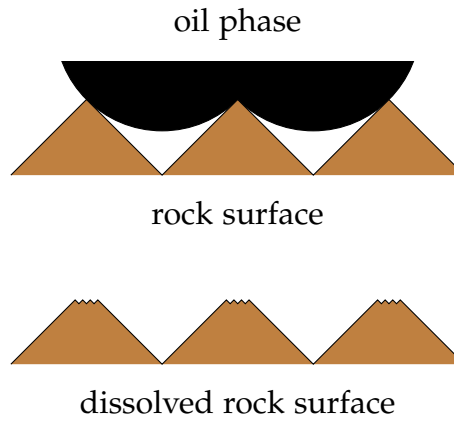


Figure 1.3: Idealized representation of the mechanism of oil recovery due to calcite dissolution. Initially oil is attached to the acute edges of the rock. These regions of high curvature are more likely to dissolve and when this happens the oil is liberated.

(2010) are in line with the data obtained from the spontaneous imbibition experiments – a shift from formation water (which contained no SO_4^{2-}) to seawater as an injected brine significantly improved the recovery factor. Moreover, further injection of diluted seawater resulted in no additional oil production. This finding is in direct contradiction with another publication (Yousef et al., 2010), where a reverse trend was observed – more oil was produced as the injected seawater was progressively diluted, thus reducing the concentration of the relevant divalent ions. These results are presented in Fig. 1.4, see Tables 1.1-1.3 for experimental conditions. Finally, Gupta et al. (2011) performed another set of coreflood experiments, where they concluded that the recovery improvement occurs as a result of the reduction of Ca^{2+} and Mg^{2+} concentrations in the injected brine.

Tables 1.1-1.3 list the main properties and parameters of the discussed experiments except for the recovery factors (RF). In the study by Karoussi and Hamouda (2007) up to 17% of the OOIP was recovered with distilled water, 23% with 0.1 M solution of Na_2SO_4 and 34% with 0.1 M solution of MgCl_2 . These results correspond to 90 °C and distilled water as a connate brine. However, when the same fluid was used both as a connate brine and an imbibing brine, the recovery dropped to 20% for Na_2SO_4 and to 16% for MgCl_2 . In the study by Strand et al. (2006) successively using seawater with zero, average and three times average seawater concentration as imbibing brines resulted in RFs of 8 → 14 → 24. Recovery results reported by Zhang et al. (2007) are presented in Fig. 1.1. In the study by Fathi et al. (2010) successive flooding with formation water (FW), seawater (SW) and three times diluted SW led to RFs of 20 → 42 → 42.

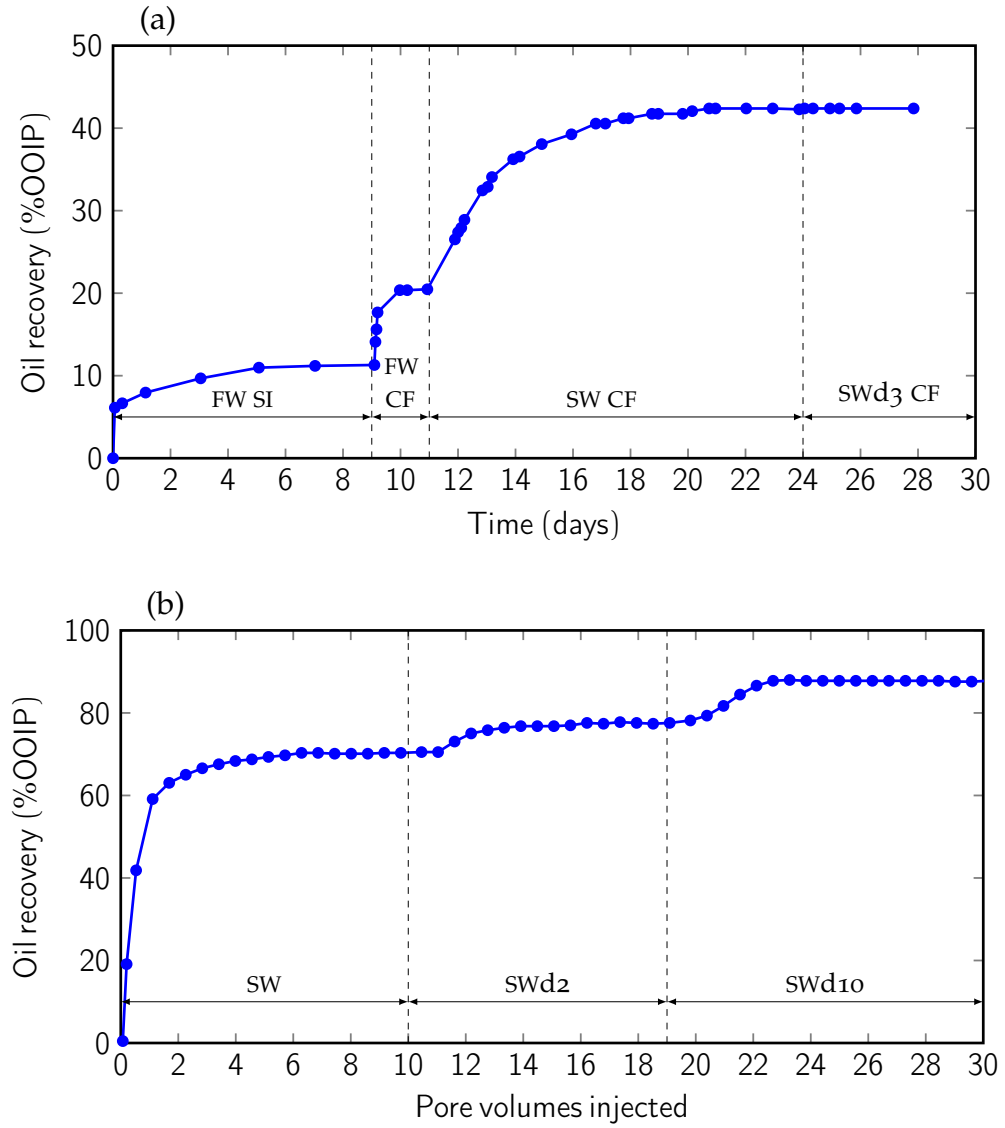


Figure 1.4: Oil recovery during the coreflooding experiments reported by Fathi et al. (2010) (a) and Yousef et al. (2010) (b). SW denotes seawater, while SWdn denotes seawater mixed with distilled water such that the resulting salinity is reduced by a factor of n . SI marks spontaneous imbibition experiments, CF – coreflood experiments. Graph in (a) demonstrates no additional oil recovery when switching the injected brine from SW to SWd₃, while graph in (b) shows the incremental recovery correlated with the seawater dilution.

Table 1.1: Summary of previously reported controlled-salinity experiments. DW denotes distilled water, SW – seawater, AN – acid number, PV – pore volume.

PUBLICATION	Karoussi and Hamouda (2007) ¹	Strand et al. (2006)
Rock type	Stevns Klint chalk	Stevns Klint chalk
ϕ (%) / k (mD)	48-50 / 2-5	48-49 / 2-5
PV (ml)	34	19-32
S_{wr} (%)	30-35	26-28
Injection rate (ml/min)	sp. imbib.	sp. imbib.
Oil AN (mg KOH/g)	n/a	2.1
Injected brines	DW, solutions of $MgCl_2$ and Na_2SO_4	SW with varying SO_4
Temperature (°C)	40 → 70 → 90	110

¹ n-decane was used instead of oil. The contact angle measurements showed that the rocks were water-wet. Hence recovery was observed even with DW as imbibing fluid.

However, in the study by Yousef et al. (2010) successive flooding with FW, SW and SW diluted twice, 10, 20, 20 and 100 times resulted in RFs of 67 → 74 → 83 → 85 → 85 for the first core and 74 → 82 → 93 → 94 → 94 for the second core. Finally, Gupta et al. (2011) reported that a sequence of FW, FW without Ca^{2+} and Mg^{2+} , FW without Ca^{2+} and SW without SO_4^{2-} led to RFs of 58 → 69 → 73 → 75.

An interesting side effect of the same charge-altering mechanism, as discussed by Austad (2008), is the induced anomalously high compaction of chalk rocks, first observed during the production of the already mentioned Ekofisk oilfield in the North Sea. However, it was then experimentally demonstrated by Madland et al. (2011) that the presence of SO_4^{2-} or Ca^{2+} in the injected fluid was not necessary for compaction to occur and that it was correlated with precipitation of magnesium-bearing minerals and the concomitant dissolution of calcite.

To summarize, the exact nature of the seawater-chalk interaction that leads to oil liberation remains unknown. This makes it impossible to accurately design the EOR projects for carbonate reservoirs that involve seawater injection as the result is uncertain. As a first step towards elucidating this mechanism, it is necessary to revisit all available laboratory evidence of seawater-chalk interaction and determine what chemical mechanisms are responsible for the observed experimental behaviour. More specifically, all previous speculations on the seawater-rock interaction were based on series of single-phase coreflood experiments (Madland

Table 1.2: Summary of previously reported controlled-salinity experiments (continued). FW denotes formation water, SW – seawater, AN – acid number, PV – pore volume.

PUBLICATION	Zhang et al. (2007) ²	Fathi et al. (2010) ³
Rock type	Stevns Klint chalk	Stevns Klint chalk
ϕ (%) / k (mD)	47-49 / 2-5	46 / 1-2
PV (ml)	29-30	36
S_{wr} (%)	21-23	8
Injection rate (ml/min)	sp. imbib.	0.025
Oil AN (mg KOH/g)	2.07	1.9
Injected brines	SW with varying SO_4	FW, SW, diluted SW
Temperature (°C)	70 \rightarrow 100 \rightarrow 130	120

² Initially zero Ca^{2+} and Mg^{2+} were present in the brines. Either of those was added during the 100 °C stage and induced additional recovery. Prior to this all brines resulted in the recovery factor of 13% at 100 °C. Results are presented in Fig. 1.1.

³ FW had 2x salinity of SW with high Ca^{2+} (2x the SW level), no SO_4^{2-} , low Mg^{2+} (1/5 of SW level).

et al., 2011; Strand et al., 2006; Zhang et al., 2007), where SO_4^{2-} , Ca^{2+} and Mg^{2+} breakthrough curves were analysed at various temperatures and relative concentrations. This is the data that we will examine in this thesis.

To systematically analyse these curves, we will construct a continuum-scale numerical model of reactive transport in the porous medium that can generate the numerical analogues of the experimental measurements. By controlling what mechanisms, i.e. adsorption or dissolution and precipitation, are included in the simulations, we will be able to determine what mechanisms control the solute concentration levels in the experiments. Prior to this work, few efforts at formalizing the experimental results in a mathematical model were made. A link between calcite dissolution and oil recovery was established by Hiorth et al. (2010a) as an outcome of a 0D chemical box model of seawater at equilibrium with calcite rock. Additionally, this model accounted for the formation of surface complexes on a calcite surface in contact with an aqueous solution. In a study by Evje et al. (2009) a 1D reactive transport model was constructed. It considered dissolution/precipitation processes to be kinetic but discarded the surface complexation and as such did not account for adsorption. Moreover, it was used to model only a single set of coreflood experiments presented by Madland et al. (2011), where a loss of Mg^{2+} and an equal production of Ca^{2+} were observed during the injection of $MgCl_2$ solution into a chalk rock. Authors successfully demonstrated

Table 1.3: Summary of previously reported controlled-salinity experiments (continued). FW denotes formation water, SW – seawater, AN – acid number, PV – pore volume.

PUBLICATION	Yousef et al. (2010) ⁴	Gupta et al. (2011) ⁵
Rock type	Undisclosed carbonate	Middle East limestone
ϕ (%) / k (mD)	25 / 40 and 68	20-25 / 2.7-9.5
PV (ml)	37 and 64	9-14
S_{wr} (%)	10.5 and 14.5	9.5-20
Injection rate (ml/min)	1	0.1
Oil AN (mg KOH/g)	0.25	0.11
Injected brines	FW, progressively diluted SW	FW with varying hardness, SW with varying SO_4
Temperature	100	121

⁴ FW had 4x salinity of SW with high Ca^{2+} (3ox the SW level), negligible SO_4^{2-} , SW level of Mg^{2+} . Two composite cores were used in the experiments.

⁵ FW had 4x salinity of SW with high Ca^{2+} (3ox the SW level), negligible SO_4^{2-} , SW level of Mg^{2+} .

that these observations could be interpreted as a precipitation of $MgCO_3$ accompanied by a simultaneous dissolution of $CaCO_3$.

Wettability alteration is fundamentally a pore-scale phenomena as it affects local capillary rather than viscous forces. To this date, there are very few pore-scale studies that investigate the interplay between reactive transport leading to wettability alteration and the subsequent change in the two-phase fluid flow. In this work we, therefore, construct a novel pore-scale simulator capable of modelling the single-phase reactive transport of the dissolved solutes. We also demonstrate how it can be extended to account for the presence of the second trapped immiscibly fluid phase. In the following section we will give a brief overview of the field of the pore-scale modelling.

1.2 PORE-SCALE MODELLING

The field of pore-scale simulation has grown over the last decade (Meakin and Tartakovsky, 2009) and applications include calculating the spatial distribution of the velocity field (Narsilio et al., 2009), solute transport (Acharya et al., 2007; Bijeljic et al., 2004), mixing and chemical reactions (Li et al., 2006; Tartakovsky and Neuman, 2008; Willingham et al., 2008) and multi-phase flow (Aker et al., 1998; Blunt, 2001; Celia et al., 1995; Knackstedt et al., 2001). Another important application of pore-scale

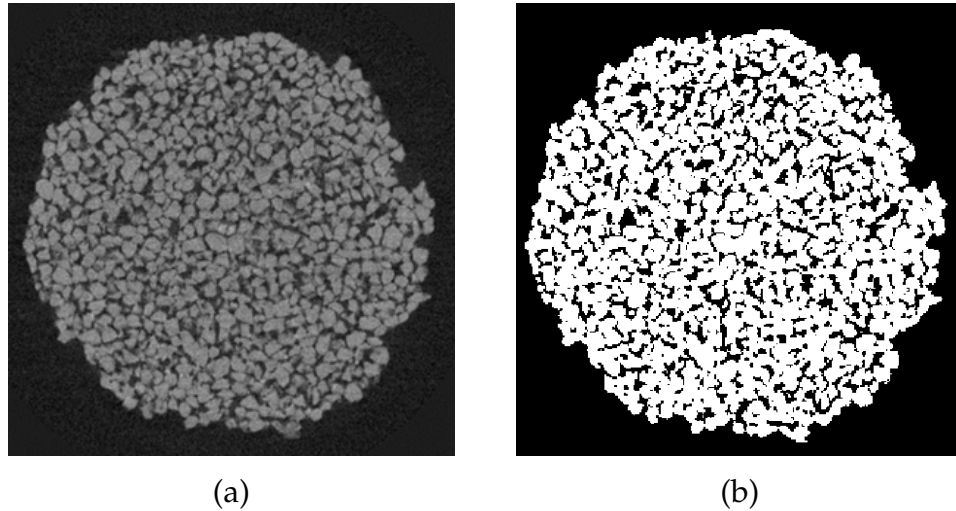


Figure 1.5: A 2D slice from the tomographic image of a sandstone sample (a) and the partitioning of this image into black pores and white grains (b). Images courtesy of Tannaz Pak, University of Edinburgh.

modelling is related to upscaling and averaging in porous media. One example of this is deriving the relations between the underlying microscale variables and their averaged macroscale counterparts, such as the true pressure in the Navier-Stokes equation versus the average pressure in Darcy's law (Nordbotten et al., 2007).

As mentioned earlier, pore-scale models that couple reactive solute transport and multi-phase flow are just beginning to emerge. The need for such models is largely driven by the problem of CO_2 storage in saline aquifers, which is characterized by a strong interplay between the multi-phase flow and chemical processes. However, including all the relevant pore-scale physical processes, such as partial CO_2 dissolution in the aqueous phase which affects density and viscosity ratios between different fluid phases, or the mixing-induced rock dissolution or precipitation, is currently impossible in practice due to both hardware limitations and the lack of algorithms capable of accounting for all the relevant phenomena. Therefore, when it comes to pore-scale modelling, researches mostly concentrate on just one aspect of a problem - either multi-phase flow or single-phase multi-component transport. One example of a coupled model was reported by Hammond and Unsal (2012). The model considered the transport of a single solute, whose adsorption onto the water-oil and water-rock interfaces affected the interfacial tension and the contact angle.

Prediction of the physical properties of the porous media from their microscopic origins involves an accurate characterization of the detailed structure of the pore space. Several approaches exist for obtaining the pore structure. It is possible to measure it directly and non-destructively by the means of (synchrotron) X-ray computed microtomography (Dunsmuir et al., 1991; Spanne et al., 1994). Fig. 1.5 shows an example of a slice through a 3D tomographic image of a sandstone sample of about 5 mm in diameter. In general, these measurements are limited by the resolution of the scanning equipment. Typical resolution of a CT image of a porous sample is several micron and there is a trade-off between the resolution and the overall sample size. Sub-micron resolution can be achieved with alternative techniques, such as scanning electron microscopy (SEM), but the resulting images are two-dimensional. It is possible to reconstruct the 3D pore geometry from the 2D images using statistical methods (Adler et al., 1990; Okabe and Blunt, 2004; Roberts, 1997). These methods consist of measuring the statistical properties, such as porosity, two-point correlation function and multi-point statistics, on the available 2D images of a porous sample. This is followed by a random generation of a 3D model that matches the obtained properties. It was shown that statistically identical porous samples can have different hydrodynamic properties (Øren and Bakke, 2002) mainly due to poor connectivity of the generated media. A more elaborate statistical method, which avoids this deficiency and is based on the Markov Chain Monte Carlo approach, was reported by Wu et al. (2006). Process-based models have been proposed (Øren and Bakke, 2002) as an alternative to the statistical methods. In this technique, rather than generating a sample randomly, it is constructed as a succession of the numerical analogues of the physically justified processes, such as grains sedimentation, compaction and diagenesis. While involving extensive calculations, this method results in the generated media with the pore connectivity that best matches the connectivity of the physical porous samples.

The two most wide-spread types of methods for the numerical simulations of single-phase transport processes at the pore scale are pore-network simulations (Blunt, 2001) and Lagrangian particle-based methods, among which lattice Boltzmann (LB) methods (Chen and Doolen, 1998) are the most popular ones. The use of pore networks to represent multi-phase flow can be dated back to the middle of the previous century. This approach involves additional conversion of the measured pore space

structure into an idealized network of pore bodies interconnected by narrow pore throats of various cross-section shapes. The use of a simplified set of flow equations and the absence of the necessity to explicitly track fluid-fluid interfaces currently renders pore networks technique the only method that can be applied to simulating multi-phase flows in numerical rocks with hundreds of thousands of pores. As such it currently has the best predictive capabilities. Lopez et al. (2010) demonstrate that for rocks with the relatively homogeneous pore geometry pore-network modelling produces reliable results for permeability, relative permeabilities, capillary pressure, initial water and residual oil saturations, Amott-Harvey wettability index. They conducted a comparison between experimental measurements and numerical computations of these parameters for 28 siliciclastic reservoir rocks and showed that for a wide range of porosities (14% to 43%) and permeabilities (5 mD to 20 D) pore-network modelling produces results in agreement with the measurements.

Pore-scale modelling can be used not only to calculate average properties but also to look at the actual pore-scale characteristics of the flow. Ryazanov et al. (2009) implemented a network model that includes a thermodynamically consistent criterion for existence of oil layers in the pore corners, based on the free energy minimization (van Dijke and Sorbie, 2006). This was later used by Sorbie et al. (2011) to investigate the structure of residual oil as a function of sample's wettability. Joekar-Niasar et al. (2010a) used network modelling to investigate the capillary pressure-saturation hysteresis. The authors argue that specific fluid-fluid interfacial area is a major state variable for two-phase flows that is required to explain the typically observed hysteresis.

Pore-network modelling is currently the only tool that can tackle three-phase problems on large domains. Nardi et al. (2009) presented a general network model to simulate three-phase flow that allows for intermediate phase layer to be sandwiched between wetting and non-wetting phases. The existence of these layers is determined based on the geometrical considerations. It shows a fair agreement between experiments and numerical modelling. Al-Dhahli et al. (2011) introduced a novel thermodynamic criterion for formation and collapse of the phase layers (van Dijke and Sorbie, 2003) into a pore network model and implemented a multi-displacement mechanism that makes it possible to model water-alternating-gas (WAG) injection.

Pore networks also offer solutions for modelling flow through the rocks characterized by a much more intricate multi-scale pore structure, such as carbonates with intercrystalline microporosity, intergranular macroporosity, vugs and fractures all contributing to the fluid flow. In such a case the comparison between modelling and laboratory measurements cannot be made unless the effects of multi-scale porosity are incorporated into the model. Wu et al. (2011) showed that a pore-network constructed from a micron-scale CT scan of a carbonate sample underpredicts the sample permeability by an order of magnitude. Incorporating a sub-micron-scale network into the micron-scale network brought the resulting permeability much closer the experimental value. An alternative approach was presented by Bauer et al. (2012), where sub-micron porous regions are incorporated by means of their average porosity and permeability values. This method, however, makes two-phase flow simulations very non-trivial to implement.

Despite the success of pore networks as a modelling tool, it is characterized by a number of limitations. Most network models are restricted to capillary dominated conditions when the influence of viscous forces on fluid distribution is neglected, which prevents them from being used, for instance, to study the effects of discontinuous phase mobilization. To rectify this, dynamic pore network models are being developed. Idowu and Blunt (2010) demonstrated a pore network model that accounts for the time taken to fill network elements and allows swelling of the wetting phase near an advancing water front. It is applied to a domain with 100,000 pores and is shown to reproduce the Buckley-Leverett profile directly from the pore-scale. Another limitation of pore networks is the uncertainty of network shapes in representing the true pore geometry. This is also an ongoing research topic. Joekar-Niasar et al. (2010b) presented a new method for generating the pore throat cross-sections based on recovering the whole range of shape factors present in a porous sample. This allowed them to reproduce not only the experimentally measured capillary pressure curves, but also the measured fluid-fluid interfacial area curves.

Single- and multi-component transport problems can also be tackled by means of pore-network modelling. It has been successfully used to upscale the Brownian motion of an advected inert tracer to quantify the sample's dispersivity (Acharya et al., 2007). Algive et al. (2010) used pore networks to model the pore-scale reactive transport of a CO₂-rich

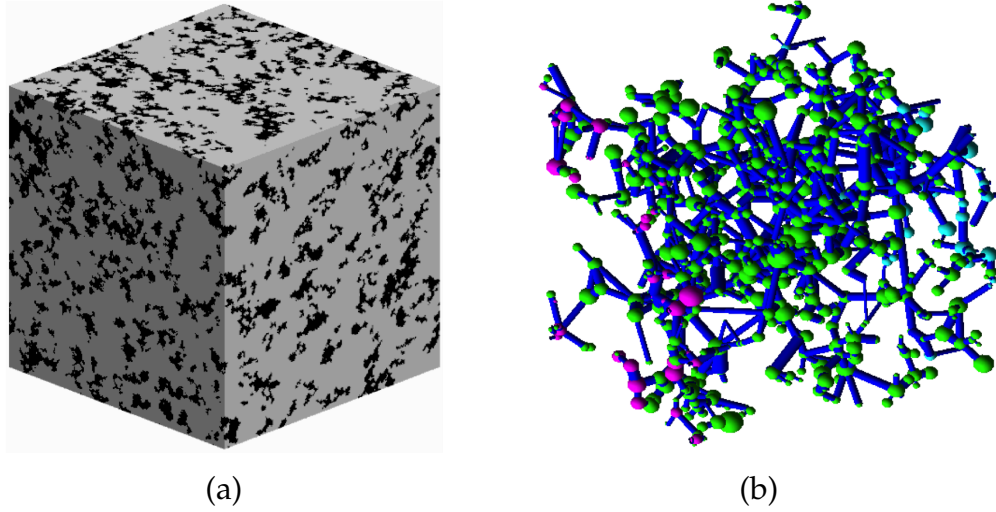


Figure 1.6: A 3D CT image of a porous rock (a) and a corresponding pore network (b). While a pore network representation is enough to recover certain flow properties of the sample (e.g. one- and two-phase permeabilities), it is not sufficient to model the reactive solute transport that involves fluid-rock interaction, which usually depends on the surface roughness.

brine, allowing for pore throats to change their radii based on the amount of dissolution or precipitation and a qualitative agreement of porosity-permeability relation with experimental measurements was obtained. However, because the radius change occurred uniformly along a given throat and because the topology of the network remained the same during the calculation, it remains to be seen how well this approach represents the actual phenomena. An already mentioned study by Hammond and Unsal (2012) used pore-networks to couple the transport of a sorbing wettability altering agent with the two-phase flow. The major obstacle for reactive transport modelling with pore networks is the fact that they do not accurately preserve the original sample geometry, which is important for applications that involve the fluid-rock interactions where a particular goal is to understand how the reacted rock surface evolves over time. This can be seen in Fig. 1.6, where a 3D CT image of a porous rock is followed by a pore network that corresponds to it. The surface of idealized throats in the pore network cannot adequately represent the surface features present in the CT image.

The latter limitations can be surmounted by simulating the fluid dynamics directly on the pore structure images. In this case the LB method is currently the most preferable choice. It is usually applied directly on the voxelized regular grid, but extensions to unstructured meshes are

generally possible (Peng et al., 1998). Lattice Boltzmann method in its simplest single-phase form is very easy to implement and extension to two-phase flows are straightforward as no interface tracking is required. Ramstad et al. (2011) showed the comparison between LB calculations of relative permeabilities and experimental measurements and corroborates that the method has capabilities to predict two-phase flow properties, at least for sandstone geometries. An elaborate single-phase reactive transport LB model that accounts for the pore geometry modifications was developed by Kang et al. (2006). It was used by Kang et al. (2010) to simulate the flow of CO₂-rich brine through a 2D porous sample.

The LB method also allows the construction of models characterized by multi-scale porosity. For example, Kang et al. (2002) showed how the Darcy flow can be recovered with the LB method and how it can be coupled with the Navier-Stokes flow in the rest of the model.

Nevertheless, care should be taken when using LB methods. Narváez et al. (2010) showed that permeability calculations in 3D sandstone samples demonstrate a strong unphysical sensitivity to fluid viscosity through the variation of relaxation time. The sensitivity can be reduced but not eliminated by using a multi-relaxation time (MRT) scheme (d’Humières, 1994). Similar comments can be made about LB multi-phase modelling – the most popular multi-phase Shan-Chen model (Shan and Chen, 1993) is not thermodynamically consistent and the resulting surface tension term in the Shan-Chen model has a different form from the one in the two-phase Navier-Stokes equation. Kuzmin et al. (2008); Kuzmin and Mohamad (2010) showed how Shan-Chen model can be improved using the MRT method. The main shortcoming of the multiphase LB method is its inability to model the problems with high viscosity and/or density contrasts between the two fluids. It also suffers from the spurious currents, i.e. unphysical non-zero velocity values near the fluid interface for the systems at equilibrium. Finally, the multiphase LB method requires to use separate particle populations for different fluids, thus significantly increasing the computational burden of the algorithm. This is in contrast to the grid-based methods where a single set of equations is solved on the domain irrespective of the number of the fluid phases and the phase separation is achieved by means of the interface tracking.

LB methods only discern between the fluid and the solid nodes of a given numerical grid. This presents a drawback of LB approach with respect to two-phase flow modelling as compared to the pore-network

technique. Namely, it becomes practically impossible to include the fluid layers that form in the pore corners, because this would require an unreasonable level of mesh refinement in the regions occupied by these layers. As a result, the fluid connectivity within the pore space is not represented correctly with the LB methods.

Despite being easy to implement in the code, multi-phase LB methods are very computationally demanding. The matter is mitigated by the fact that LB schemes are embarrassingly parallel, but they still require a large number of computational nodes if a calculation is to be conducted on a reasonably large domain. As an example, a mature open-source LB code Palabos was used by Parmigiani et al. (2011) to model two-phase flow coupled with solid melting. Authors indicate that for each simulation they used 2000 processors with run times of up to 60 hours for the samples with $200 \times 200 \times 300$ lattice nodes.

As stated above, the LB method is not the only particle-based approach and other examples include Dissipative Particle Dynamic (DPD) (Hoogerbrugge and Koelman, 1992), Smoothed Particle Hydrodynamic (SPH) (Lucy, 1977) and Moving Particle Semi-implicit (MPS) (Koshizuka et al., 1995). The use of SPH method for simulating two-phase flows and single-phase flows with solute precipitation was demonstrated by Tartakovsky et al. (2007b,a), albeit only for 2D models. Ovaysi and Piri (2011) used MPS to investigate the influence of non-linear inertial term of Navier-Stokes equation on the dispersion. The main advantage of MPS method among other particle methods is its ability to simulate the flow of truly incompressible fluids.

While particle-based methods offer means to recover the solution of the Navier-Stokes equation, it is possible to seek its solution directly, using traditional grid-based approaches, such as finite difference, finite element or finite volume methods. For the single-phase applications this is the preferred approach because of its better numerical efficiency compared to all particle-based methods. Having said this, the main obstacle here is still the amount of computational work, which grows rapidly with the complexity of domain geometry (i.e., number of nodes required to correctly represent the domain boundaries increases) and with the dimensionality of the problem. This is because the inversion of the matrix representing the discretized equations for the geometry of interest is very costly, prohibiting the use of large pore samples or complex geometries. Therefore, this method is usually applied either in 2D (Garmeh et al.,

2009) or in 3D with a simplified domain geometry, such as packs of spheres (Cardenas, 2008, 2009).

Previous work that deals with the Navier-Stokes solution on experimentally measured pore geometries uses relatively small sample sizes (Fourie et al., 2007; Gerbaux et al., 2009; Malinouskaya et al., 2008). However, recently Mostaghimi et al. (2010) used finite difference method to solve Stokes equation on a large sample ($300 \times 300 \times 300$ voxels), followed by a streamline-based algorithm to simulate the solute transport. An interesting approach was demonstrated by Smolarkiewicz and Larrabee Winter (2010), where grain surfaces are introduced not through mesh conformance but with an immersed boundary method. Other methods were suggested that approximate the solution of the Navier-Stokes problem (Akanji and Matthäi, 2010), but their comparison against the exact solution requires further analysis.

Several methods exist that extend the Navier-Stokes equation to the description of the multi-phase fluid flows. These include volume of fluid (Hirt and Nichols, 1981), level-set (Sethian, 1999), and phase-field (Jacqmin, 1999) methods. The volume of fluid method is hard to combine with arbitrarily shaped elements, usually met in the unstructured meshes; it also produces discontinuous interface surfaces. The level-set method does not strictly conserve the fluid mass and does not provide direct means to specify the wetting angle at the fluid-solid interface. The phase field method requires local grid refinement near the fluid interface, which is again non-trivial to implement on unstructured grids. Unstructured meshes also do not provide a clear way of calculating the local interface curvature which is necessary for computing the surface tension forces in all the above-mentioned approaches. To this date very few applications of these methods to the problems of the porous media fluid flows were reported in the literature. Prodanovic and Bryant (2006) used level-set method to simulate quasi-static drainage and imbibition processes, i.e. omitting the solution of the Navier-Stokes equations. Xu et al. (2011) used the volume of fluid method with the Navier-Stokes solution on a small idealized 3D porous domain to model CO_2 injection. At present the potential applications of these methods far exceed the available implementations.

The large body of research that deals with various methods for single- and multi-phase flow modelling at the pore-scale suggests an on-going interest in methods that link 3D images of porous rocks and numerical

modelling of their various transport properties. Despite that, as suggested by Sorbie and Skauge (2011), the pore-scale modelling can never be truly predictive in the sense that the overall number of parameters that characterize the construction of a numerical pore scale model is larger than the number of parameters available from the laboratory data. It is, however, an invaluable tool for explaining the observed experimental measurements as well their extrapolation outside the conditions (i.e. temperatures, solute concentrations, etc.) available in the laboratory.

1.3 STRUCTURE OF THE THESIS

The rest of the thesis is structured as follows. In Chapter 2 we describe the numerical method for simulating the single-phase fluid flow and inert solute transport in porous media. The chapter describes how the experimental computed tomography data is converted into a numerical grid. It is subsequently used to solve the Stokes equations to obtain fluid velocity profile and the advection-diffusion equation to describe the solute transport. In Chapter 3 we extend this method to include the reactive transport of single or multiple components. We also describe a rule-based method based on pore size distribution to obtain the two-phase fluid distribution within the pore space. In Chapter 4 we revisit the available experimental measurements of the chemical interaction between seawater and chalk rocks and determine what chemical effects can explain these measurements. We conclude the chapter with the discussion on what implications these might have on the two-phase flow in chalk. We finish the thesis with recommendations on how this work can be extended in the future. Fig. 1.7 demonstrates the structure diagram of this thesis including the potential avenues for the future work.

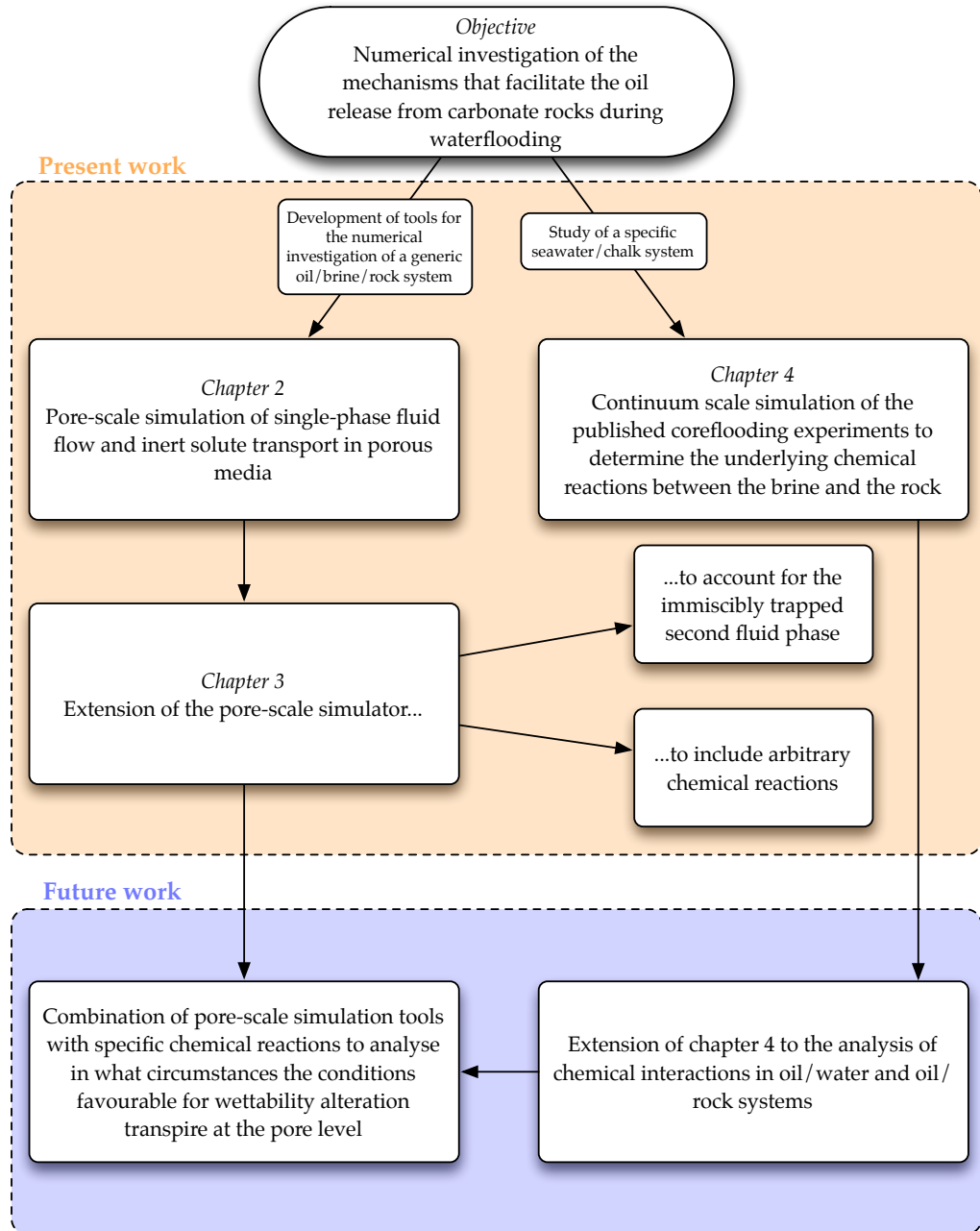


Figure 1.7: Organization of the thesis including the potential directions for the future work.

PORE-SCALE MODELLING OF INERT TRANSPORT

CONTENTS

2.1	Introduction	23
2.2	Numerical methods	25
2.2.1	Continuous formulation of fluid flow equations	25
2.2.2	Weak form of Stokes equation	27
2.2.3	Discrete form of Stokes equations	29
2.2.4	Benchmarking against analytical solution	31
2.2.5	Combined FE-FV method for advection-diffusion equation	33
2.2.6	Algebraic multigrid method	36
2.2.7	Parallel discretization	39
2.2.8	Mesh generation	40
2.3	Method application	43
2.3.1	Reconstructed 3D meshes	43
2.3.2	Pressure and velocity profiles	44
2.3.3	Solute transport	47
2.4	Summary	54

2.1 INTRODUCTION

Understanding the fundamental physics of fluid flow and transport in porous media is a crucial topic for all fields dealing with mass and heat transfer in subsurface systems, such as groundwater reservoirs, saline aquifers targeted for CO₂ storage, oil and gas fields or geothermal fields. Continuum-scale models, which are used to describe flow at the scale of a reservoir, rely on various macroscopic parameters, such as the effective permeability, porosity or dispersivity. However, these macroscopic parameters in turn depend on the underlying microscopic properties of the system. They can be measured either experimentally or in some cases computed by means of numerical modelling of physical phenomena at the pore scale. The advantages of the second approach lie in the fact that, once the numerical algorithm is established, it can complement exper-

imental data by providing additional information and understanding about the phenomena under study. For instance, numerical modelling can show the details of fluid flow within separate pores of a rock sample and give insight into why a macroscopic parameter such as dispersivity or the extent of reacted grain surface area behaves in a certain way. Therefore, it is important to develop pore-scale models that allow us to predict the fluid flow properties directly from the information about the pore space geometry. One impediment to this upscaling process is the complexity of the geometry and topology of the pore system in realistic rocks.

In this work, we present a computationally efficient approach to simulate single-phase fluid flow and solute transport in porous media. It is based on the unstructured FE - finite volume (FV) method that resolves pore space geometry in great detail while solving the fundamental Navier-Stokes and advection-diffusion equations without invoking additional physical assumptions. Our FE-FV realization is made using the Complex System Modelling Platform (CSMP++) (Matthäi et al., 2007), our in-house object-oriented finite element - finite volume based C++ library tailored to simulating a wide range of fluid flow processes in geometrically complex porous media. The computational domain is discretized by an unstructured FE method and contains a complementary FV grid. Unstructured meshes with varying element sizes result in accurate capturing of grain boundary shapes while at the same time avoiding the overrefinement of internal regions of large pores. The meshes are constructed from X-ray computer tomography scans of real 3D porous samples, but could equally well be applied to any pore system model, e.g. from a 3D numerical reconstruction method (Wu et al., 2004, 2006). In order to increase the efficiency of the calculations, we use CSMP++ in conjunction with an algebraic multigrid (AMG) solver (Stüben, 2001). AMG methods have the distinctive advantage that they scale linearly as a function of the number of the unknowns.

We solve the Stokes equation at the pore scale for the full FE grid to obtain the velocity field for single phase flow, from which permeability of the sample can be calculated. With this velocity field we then solve the tracer solute transport equation for a species with molecular diffusion coefficient, D_m , in order to calculate the upscaled dispersion coefficient D . This procedure is repeated at a range of flow velocities to obtain D as a function of flow rate; more precisely we construct two plots: D/Ua vs Peclet number $Pe = Ua/D_m$ and D/D_m vs Pe , where U is an average

flow velocity and a is an average grain size. The first plot highlights the transition between various types of flow regime while the second one allows a quantitative comparison of sample dispersivities with other published results. Both results are compared with the previously reported experimental and numerical findings.

2.2 NUMERICAL METHODS

2.2.1 Continuous formulation of fluid flow equations

The partial differential equations that govern the incompressible Newtonian fluid flow within an arbitrary domain Ω are the Navier-Stokes equations. These equations arise from applying Newton's second law to fluid motion, with the fluid stress being a combination of the shear stress between parallel fluid layers (proportional to the gradient of velocity) and the local pressure gradient

$$\rho \frac{d\mathbf{u}}{dt} = \rho \frac{\partial \mathbf{u}}{\partial t} + \rho(\mathbf{u} \cdot \nabla)\mathbf{u} = \mu \nabla^2 \mathbf{u} - \nabla p. \quad (2.1)$$

There are four unknowns in Eq. 2.1 (vector \mathbf{u} and scalar p) and only three equations. An additional condition necessary to solve the Navier-Stokes equations is the law of mass conservation. For an isothermal incompressible fluid it assumes the form

$$\nabla \cdot \mathbf{u} = 0, \quad (2.2)$$

where the following notation is used

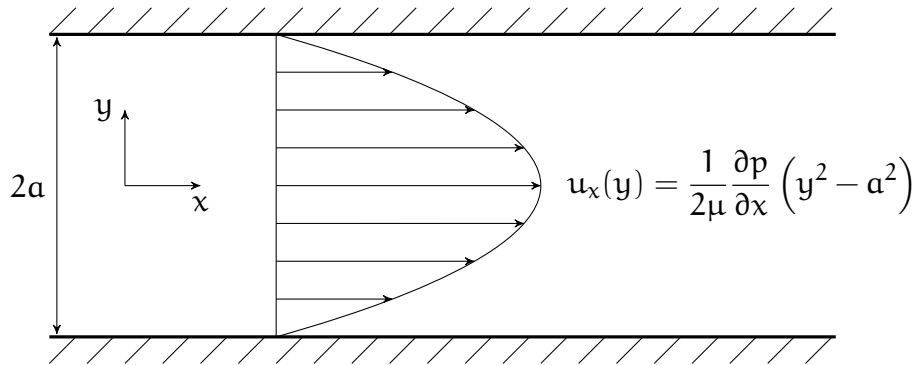


Figure 2.1: Velocity profile for a viscous fluid in a 2D channel with parallel walls subject to a constant pressure gradient, commonly known as the Poiseuille flow.

- p pressure, [Pa]
- ρ density, [kg/m³]
- μ viscosity, [Pa·s]
- \mathbf{u} velocity, [m/s]

Perhaps the most surprising fact regarding the Navier-Stokes equations is that despite the immense importance of their solution to many fields of science and engineering (e.g. weather prediction, aircraft design, flow in blood vessels, labs-on-a-chip design), there is no general proof of its existence and smoothness. At the time of writing of this thesis a prize of \$1,000,000 is offered by Clay Mathematics Institute to the first person to solve this problem.

In what follows, we consider the case of creeping flow, characterized by a very low Reynolds number ($Re \sim 10^{-1}$). This condition occurs in most porous media flow problems and is well studied (Happel and Brenner, 1983). In this case the non-linear term in Eq. (2.1) vanishes. Additionally, in this work we focus on the steady-state flows and, therefore, we solve Eq. (2.1) without considering the time derivative term. Overall, the governing Stokes equations describing laminar steady-state flow of a single fluid phase in a porous medium are

$$\mu \nabla^2 \mathbf{u} = \nabla p. \quad (2.3)$$

The boundary conditions, necessary to close Eqs. (2.2)-(2.3), include the no-slip condition at the rigid boundaries, i.e. $\mathbf{u}|_{\Gamma_{\text{rigid}}} = \mathbf{0}$, as well as the proper conditions at the inflow and outflow boundaries. Instead of assigning the inflow velocity profile, which can be considered as a more traditional type of Dirichlet boundary conditions, we follow the procedure described by Heywood et al. (1996), in order to impose the prescribed pressure drop across the porous sample. Namely, we set that

$$p - \mu \partial_n \mathbf{u}|_{\Gamma_{\text{in/out}}} = P_{\text{in/out}} \quad (2.4)$$

for both the inflow and outflow boundaries $\Gamma_{\text{in/out}}$, where $P_{\text{in/out}}$ are the desired pressure values and ∂_n denotes a spatial derivative in a direction normal to the corresponding boundary. The discrepancy between the intended and realized pressure drop due to the second term of left-hand side of Eq. (2.4) is proportional to $1/r^3$ in the three-dimensional case,

where r is a curvature radius of the boundary surface. Hence, in our case of flat boundaries, this mismatch is cancelled. Therefore, the final system of equations to be solved numerically assumes the following form

$$\left\{ \begin{array}{ll} \mu \nabla^2 \mathbf{u} = \nabla p & \text{in } \Omega, \\ \nabla \cdot \mathbf{u} = 0 & \text{in } \Omega, \\ \mathbf{u} = \mathbf{0} & \text{on } \Gamma_{\text{rigid}}, \\ p - \mu \partial_n \mathbf{u} = P_{\text{in}} & \text{on } \Gamma_{\text{in}}, \\ p - \mu \partial_n \mathbf{u} = P_{\text{out}} & \text{on } \Gamma_{\text{out}}. \end{array} \right. \quad (2.5)$$

In the general case, the solution of Eq. 2.5 cannot be obtained analytically. A well-known textbook example where the analytical solution is known is the Poiseuille flow between two parallel plates in 2D (depicted in Fig. 2.1) or in a cylinder in 3D, where a constant pressure gradient is applied to the fluid parallel to the channel boundaries. In this case the fluid velocity is collinear to the pressure gradient and its magnitude increases quadratically as a function of the distance from the channel walls, reaching its maximum in the centre. However, more complex cases require numerical treatment. Below we describe an algorithm of solving Eq. 2.5 using the FE method.

To finalize the short introduction to the Navier-Stokes equations, we note that volume averaging of Eq. 2.3 can be used to obtain the phenomenologically derived Darcy law

$$\mathbf{q} = -\frac{1}{\mu} \mathbf{k} \cdot \nabla \hat{p}, \quad (2.6)$$

where \mathbf{q} is a volumetric flux vector [m/s], \mathbf{k} is a permeability tensor [m²], which depends on the pore geometry, and \hat{p} denotes average macroscopic pressure. In this case it can be seen that $\mathbf{q} = \langle \varphi \mathbf{u} \rangle$, where $\langle \cdot \rangle$ denotes volume averaging operation and φ is a porosity value, while the link between \hat{p} and microscopic pressure p is still an open question (Nordbotten et al., 2007).

2.2.2 Weak form of Stokes equation

The FE method is based upon discretization of an integral (weak) form of the considered partial differential equation. Hence, as a first step, we

have to formulate the weak form of Eq. 2.3. Here we will briefly outline the necessary steps; further details can be found, for instance, in the book by Donea and Huerta (2003).

The weak form requires the introduction of classes of functions for the velocity field and the pressure field. The space of trial solutions with respect to velocity \mathbf{u} is denoted by \mathcal{S} . It contains the approximating functions for velocity and is characterized as follows:

$$\mathcal{S} := \{\mathbf{u} \in \mathcal{H}^1(\Omega) \mid \mathbf{u} = \mathbf{u}_D \text{ on } \Gamma_D\}. \quad (2.7)$$

This means that space \mathcal{S} consists of vectors, all components of which are square integrable and their first derivatives are also square integrable. Also these vectors have to satisfy the Dirichlet boundary conditions on Γ_D , a part of the boundary $\partial\Omega$ where those conditions are prescribed. In our case $\Gamma_D = \Gamma_{\text{rigid}}$ and $\mathbf{u} = \mathbf{0}$. The weighting functions of velocity, \mathbf{w} , belong to \mathcal{V} , which is almost the same as \mathcal{S} with the exception that the weighting functions are required to vanish on Γ_D :

$$\mathcal{V} := \{\mathbf{w} \in \mathcal{H}^1(\Omega) \mid \mathbf{w} = \mathbf{0} \text{ on } \Gamma_D\}. \quad (2.8)$$

Note that for our problem (2.5) spaces \mathcal{V} and \mathcal{S} essentially coincide, but this is not a general case.

Finally, we introduce a space of functions, denoted \mathcal{Q} , for the pressure. As we shall see, spatial derivatives of pressure do not appear in the weak form of the Stokes problem; thus functions in \mathcal{Q} are simply required to be square integrable

$$\mathcal{Q} := \mathcal{L}_2(\Omega). \quad (2.9)$$

Moreover, since there are no explicit Dirichlet boundary conditions on pressure, the space \mathcal{Q} generally suffices as both the trial space and the weighting function space.

Once all the necessary spaces are established, we can construct the weak form of the system (2.5). For this we multiply the governing equations by the weighting functions (the first equation in Eq. 2.3 is multiplied by $\mathbf{w} \in \mathcal{V}$ and the second by $q \in \mathcal{Q}$) and integrate the result over the

computational domain Ω . Omitting the intermediate calculations, this results in:

$$\begin{cases} \mathbf{a}(\mathbf{w}, \mathbf{u}) + \mathbf{b}(\mathbf{w}, p) = (\mathbf{w}, P_{\text{in}} \mathbf{n}_{\text{in}})_{\Gamma_{\text{in}}} + (\mathbf{w}, P_{\text{out}} \mathbf{n}_{\text{out}})_{\Gamma_{\text{out}}}, \\ \mathbf{b}(\mathbf{u}, q) = 0. \end{cases} \quad (2.10)$$

Here $\mathbf{n}_{\text{in/out}}$ denote normal vectors to corresponding boundaries and the following definitions are utilized:

$$\begin{aligned} \mathbf{a}(\mathbf{w}, \mathbf{u}) &= \int_{\Omega} \nabla \mathbf{w} : \mu \nabla \mathbf{u} \, dV = \int_{\Omega} \sum_i \sum_j \mu \frac{\partial w_i}{\partial x_j} \frac{\partial u_i}{\partial x_j} \, dV, \\ \mathbf{b}(\mathbf{u}, q) &= - \int_{\Omega} q \nabla \cdot \mathbf{u} \, dV, \quad (\mathbf{w}, \mathbf{t})_{\Gamma} = \int_{\Gamma} (\mathbf{w} \cdot \mathbf{t}) \, dS. \end{aligned} \quad (2.11)$$

Therefore, we can see that imposed pressure drop condition manifests itself in two surface integrals in the right-hand side part of the weak form. A solution of the weak formulation is a pair of trial functions $(\mathbf{u}, p) \in \mathcal{S} \times \mathcal{Q}$ that satisfies Eq. 2.10 for $\forall(\mathbf{w}, q) \in \mathcal{V} \times \mathcal{Q}$.

2.2.3 Discrete form of Stokes equations

Finally, we establish the discretization of the weak form, which requires discretization of both trial and weighting functions.

Trial functions for pressure and velocity components are approximated as

$$\mathbf{u}_i^h(\mathbf{x}) = \sum_{\text{nodes}} N_A(\mathbf{x}) u_{iA}, \quad p^h(\mathbf{x}) = \sum_{\text{nodes}} N_A(\mathbf{x}) p_A, \quad (2.12)$$

where N_A is a shape function associated with global node number A , and u_{iA} and p_A are the values of $u_i^h(\mathbf{x})$ and $p^h(\mathbf{x})$ at a node number A . In general case velocity and pressure nodes, as well as the shape functions, can be different. With respect to Stokes equation, the choice of shape functions has to satisfy the so-called Ladyzhenskaya-Babuška-Brezzi (LBB) compatibility condition (Babuška, 1971; Brezzi, 1974; Ladyzhenskaya, 1969). This condition is not satisfied if the shape functions are chosen to be linear for both velocity and pressure; a quadratic function for velocity has to be used instead. In order to reduce the amount of computational work and use the same first order of approximation for both $u_i^h(\mathbf{x})$ and $p^h(\mathbf{x})$, we implement the Galerkin/least-squares (GLS) method (Hughes and Franca, 1987), which makes it possible to circumvent the LBB condition.

This method exhibits stable and convergent approximation for any choice of the discrete velocity and pressure interpolations. Existence, uniqueness and error behavior of the resulting FE solution has been demonstrated by Zhou and Feng (1993).

Weighting functions in the standard FE method are limited to a set of all nodal shape functions N_A . Therefore, substituting Eq. (2.12) into Eq. (2.10) together with the weighting functions N_A yields the following system of linear equations

$$\begin{bmatrix} \mathbf{K}_\mu & \mathbf{0} & \mathbf{0} & -\mathbf{G}_x \\ \mathbf{0} & \mathbf{K}_\mu & \mathbf{0} & -\mathbf{G}_y \\ \mathbf{0} & \mathbf{0} & \mathbf{K}_\mu & -\mathbf{G}_z \\ \mathbf{G}_x^T & \mathbf{G}_y^T & \mathbf{G}_z^T & \mathbf{K}_{st} \end{bmatrix} \cdot \begin{bmatrix} \widehat{\mathbf{u}}_x \\ \widehat{\mathbf{u}}_y \\ \widehat{\mathbf{u}}_z \\ \widehat{\mathbf{p}} \end{bmatrix} = \begin{bmatrix} \widehat{\mathbf{f}}_x \\ \widehat{\mathbf{f}}_y \\ \widehat{\mathbf{f}}_z \\ \widehat{\mathbf{0}} \end{bmatrix}. \quad (2.13)$$

The hat sign indicates a vector of nodal values, for example

$$\widehat{\mathbf{u}}_x = [u_{x_1} u_{x_2} \dots u_{x_n}]^T. \quad (2.14)$$

Every entry on the left-hand side matrix of Eq. (2.13) is a submatrix of the size of $n \times n$, where n is the number of mesh points. Each element's contribution to these submatrices is calculated as follows

$$\mathbf{K}_\mu^e = \mu \int_{\Omega^e} \left(\sum_i \frac{\partial \widehat{\mathbf{N}}^T}{\partial x_i} \frac{\partial \widehat{\mathbf{N}}}{\partial x_i} \right) dV, \quad (2.15)$$

$$\mathbf{K}_{st}^e = \int_{\Omega^e} \tau_e \left(\sum_i \frac{\partial \widehat{\mathbf{N}}^T}{\partial x_i} \frac{\partial \widehat{\mathbf{N}}}{\partial x_i} \right) dV, \quad (2.16)$$

$$\mathbf{G}_{x_i}^e = \int_{\Omega^e} \frac{\partial \widehat{\mathbf{N}}^T}{\partial x_i} \widehat{\mathbf{N}} dV. \quad (2.17)$$

Here Ω^e is an element volume, $\widehat{\mathbf{N}}$ is a vector containing nodal shape functions, $\widehat{\mathbf{N}} = [N_1 \ N_2 \ N_3 \ \dots \ N_n]$. Symbols $\widehat{\mathbf{u}}_{x_i}$ and $\widehat{\mathbf{p}}$ denote nodal unknowns of velocity components and pressure and $\widehat{\mathbf{f}}_{x_i}$ are right-hand side vectors containing the corresponding boundary conditions. Finally, submatrix \mathbf{K}_{st} comes from the GLS stabilization technique where τ_e is an element-wise stabilization parameter, which is best chosen as $\tau_e = \alpha h_e^2 / 4\mu$ (Codina, 2000). In this definition h_e is a measure of element size

and α is a constant of the order of unity. The choice $\alpha = 2/3$ appears to be optimal for linear elements.

It is also worth mentioning that arranging the system Eq. (2.13) unknown-wise, i.e. seeking a solution vector in the form

$$[u_{x_1} \dots u_{x_n} \quad u_{y_1} \dots u_{y_n} \quad u_{z_1} \dots u_{z_n} \quad p_1 \dots p_n]^T, \quad (2.18)$$

results in the sparse matrix that has an excessively large bandwidth. Therefore, we rearrange the vector point-wise, such that the solution vector has the form

$$[u_{x_1} \ u_{y_1} \ u_{z_1} \ p_1 \quad \dots \quad u_{x_n} \ u_{y_n} \ u_{z_n} \ p_n]^T. \quad (2.19)$$

When viewed in the light of pore-scale modelling of the fluid flow, the benefits of the Stokes FE discretization scheme that we employ are many. First, stabilized FE formulation allows us to use the first order of approximation for both velocity and pressure fields. This becomes very important when the fluid flow is to be calculated on the domains with millions of elements, as it enables us to significantly reduce the size of a linear system to be solved. Moreover, when combined with the domain parallelization, our discretization scheme results in less inter-processor communication as compared to the mixed element formulations. Finally, the choice of FE over finite difference (FD) or FV methods allows us to obtain a solution of the steady-state incompressible Stokes problem in a single computational step rather than resorting to iterative schemes that involve intermediate pressure and velocity correction stages or the artificial compressibility methods with marching in pseudo-time. Therefore, we believe that our implementation of the numerical solution of the Stokes equation is best suited for the purpose of pore-scale modelling.

2.2.4 Benchmarking against analytical solution

In order to verify the convergence of our FE scheme, we benchmarked it against an analytical solution for the stationary incompressible Stokes flow taken from the book by Donea and Huerta (2003). The problem consists of determining the velocity field $\mathbf{u} = (u_x, u_y)$ and the pressure p in a 2D square domain $\Omega = [0, 1] \times [0, 1]$ with a prescribed body force \mathbf{b} within Ω and a no-slip boundary condition on $\partial\Omega$

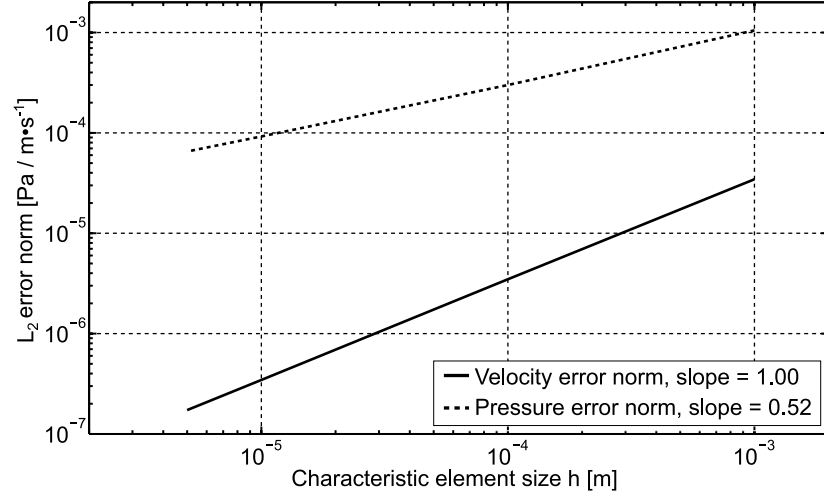


Figure 2.2: Velocity and pressure error in L_2 -norm versus characteristic element size h . Velocity field demonstrates the linear convergence while pressure converges sub-linearly due to the implemented GLS stabilization technique.

$$\begin{cases} -\mu \nabla^2 \mathbf{u} + \nabla p = \mathbf{b} & \text{in } \Omega, \\ \nabla \cdot \mathbf{u} = 0 & \text{in } \Omega, \\ \mathbf{u} = 0 & \text{on } \partial\Omega. \end{cases} \quad (2.20)$$

Fluid viscosity is taken as unity and the components of the body force \mathbf{b} are prescribed as

$$\begin{aligned} b_x &= (12 - 24y)x^4 + (-24 + 48y)x^3 + (-48y + 72y^2 - 48y^3 + 12)x^2 \\ &\quad + (-2 + 24y - 72y^2 + 48y^3)x + 1 - 4y + 12y^2 - 8y^3, \\ b_y &= (8 - 48y + 48y^2)x^3 + (-24 + 72y - 72y^2)x^2 \\ &\quad + (4 - 24y + 48y^2 - 48y^3 + 24y^4)x - 12y^2 + 24y^3 - 12y^4. \end{aligned} \quad (2.21)$$

The exact analytical solution for this problem is

$$\begin{aligned} u_x(x, y) &= x^2(1-x)^2(2y-6y^2+4y^3), \\ u_y(x, y) &= -y^2(1-y)^2(2x-6x^2+4x^3), \\ p(x, y) &= x(1-x). \end{aligned} \quad (2.22)$$

A presence of the body force leads to a slight modification of a right-hand side vector as compared to (2.13), but otherwise the linear system to be solved has the same structure. Fig. 2.2 shows that the numerical error, measured in the L_2 norm, decreases as the mesh is refined. As

mentioned before, we use linear elements for both velocity and pressure and therefore expect that the error decreases as $\mathcal{O}(h)$. Numerical results show that the error for the velocity field decreases at this rate while the pressure converges at half the rate. This is due to the pressure diffusion introduced in the stabilization term. The same difference in convergence rates for velocity and pressure would hold for a more conventional mixed FE method.

2.2.5 Combined FE-FV method for advection-diffusion equation

Transport of an inert solute, denoted as $C(\mathbf{x}, t)$ and with the units of [mol/l], within a fluid with an absence of volumetric sources and sinks is described by the general advection-diffusion equation (ADE)

$$\frac{\partial C(\mathbf{x}, t)}{\partial t} = \nabla \cdot (D_m \nabla C) - \nabla \cdot (\mathbf{u}C), \quad (2.23)$$

where \mathbf{x} is a coordinate vector and D_m is a molecular diffusivity [m^2/s]. The velocity \mathbf{u} in each pore is directly given by the solution of the Stokes equation as described above. As a boundary condition, we keep C value as a constant at the inflow boundary and allow it to undergo pure advection at the outflow boundary,

$$C(\mathbf{x}, t)|_{\Gamma_{\text{in}}} = C_0, \quad \nabla C(\mathbf{x}, t) \cdot \mathbf{n}|_{\Gamma_{\text{out}}} = 0. \quad (2.24)$$

Equation (2.23) is solved by Godunov operator splitting (Godunov, 1959), which assumes that the total time derivative can be calculated as a summation of the diffusion step and advection step. Applying the operator splitting technique has the advantage that we can use two different numerical methods to solve the diffusion and advection components, respectively. The diffusion derivative, with the assumption of constant diffusivity and absence of volumetric sinks and sources, is given by

$$\left(\frac{\partial C}{\partial t} \right)_{\text{diff}} = D_m \nabla^2 C, \quad (2.25)$$

which we solve using the FE method. The FE procedures necessary for solving the diffusion equation are well established (Istok, 1989) and similar to those described in Section 2.2.2, albeit involving only a single set of unknowns. Hence no special techniques are required to implement the

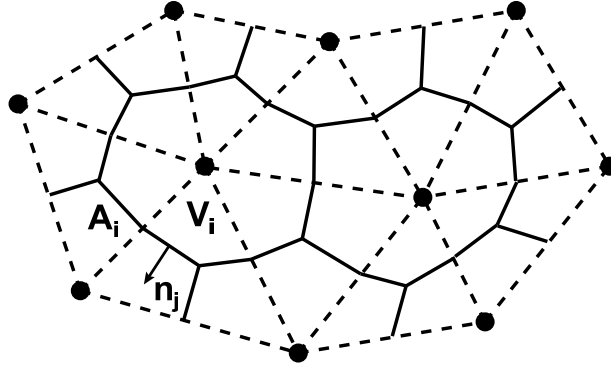


Figure 2.3: A simple 2D finite element mesh (dashed) with the corresponding and virtual node-centred finite volume mesh (solid). Mesh nodes are marked as filled black circles.

first order of approximation for the solute concentration. Discretization of the relevant weak form results in the following linear system (implicit backward Euler scheme is used for time discretization)

$$\left(\frac{\mathbf{M}}{\Delta t} - \mathbf{K}_D \right) \hat{\mathbf{C}}^{t+\Delta t} = \frac{\mathbf{M}}{\Delta t} \hat{\mathbf{C}}^t. \quad (2.26)$$

The element contribution matrices are given by

$$\mathbf{K}_D^e = D_m \int_{\Omega^e} \left(\sum_i \frac{\partial \hat{\mathbf{N}}^T}{\partial x_i} \frac{\partial \hat{\mathbf{N}}}{\partial x_i} \right) dV, \quad (2.27)$$

$$\mathbf{M}^e = \int_{\Omega^e} \hat{\mathbf{N}}^T \hat{\mathbf{N}} dV. \quad (2.28)$$

The advection derivative is given by

$$\left(\frac{\partial C}{\partial t} \right)_{\text{adv}} = -\nabla \cdot (\mathbf{u}C), \quad (2.29)$$

which we solve using the mass and shock preserving FV method.

A FV mesh is generated as a complement to a FE mesh around the corner nodes of each finite element (Geiger et al., 2004; Paluszny et al., 2007). Faces of each finite volume are constructed by connecting the finite element barycentres with the barycentres of its faces and edges, thus forming a cell around each node. A corresponding 2D FE-FV mesh representation is shown on Fig. 2.3.

We integrate Eq. (2.29) over a finite volume V_i , corresponding to a node i , and apply the Gauss-Ostrogradsky theorem

$$\int_{V_i} \frac{\partial C(t)}{\partial t} dV = - \oint_{A_i} \mathbf{n} \cdot \mathbf{u} C(t) dA. \quad (2.30)$$

Here A_i is the boundary area of the finite volume V_i and \mathbf{n} is the outward pointing normal vector of a FV boundary. The area integral on the right-hand side of Eq. (2.30) can be represented as a sum over all FV faces, marked with index j (see Fig. 2.3). By discretizing the time-derivative on the left-hand side of Eq. (2.30) using a backward Euler scheme, we obtain the following formulation

$$C_i^{t+\Delta t} = C_i^t - \frac{\Delta t}{V_i} \sum_j (\mathbf{n}_j \cdot \mathbf{u}_j) C_j^{t+\Delta t} A_j. \quad (2.31)$$

A value of solute concentration at a j^{th} face is taken to be equal to a value at an upstream node, i.e. a node for which $(\mathbf{n}_j \cdot \mathbf{u}_j) > 0$. The value of velocity \mathbf{u}_j is calculated by interpolation of the nodal values onto the barycentre of an element which the face j belongs to. We use the implicit formulation because the presence of very small elements in the meshes that represent porous samples leads to an excessively restricting Courant-Friedrichs-Lewy (CFL) criterion. For meshes used in this work, it would require about 10^5 time steps in order to fully saturate them with an inert solute. With the implicit method it was possible to reduce the amount of time steps 100 times without sacrificing numerical accuracy. For all cases when the ADE was solved in this work, a maximum acceptable time step was empirically calculated such that the evolution of the concentration profile remained the same within a desired tolerance when the time step was halved. Fig. 2.4 demonstrates the application of this criterion: for every time step we calculate the average effluent concentration of a solute as a function of the simulation time (see Section 2.3.3) and reduce the step until the resulting curve does not change.

The use of FE-FV formulation ensures that we keep the number of degrees of freedom low. Combined with the implicit time stepping scheme it allows us to solve the ADE directly on the very large computational domains in a reasonable amount of wall-clock time. This makes our approach an ideal choice for modelling solute transport at the pore scale among the variety of available candidates.

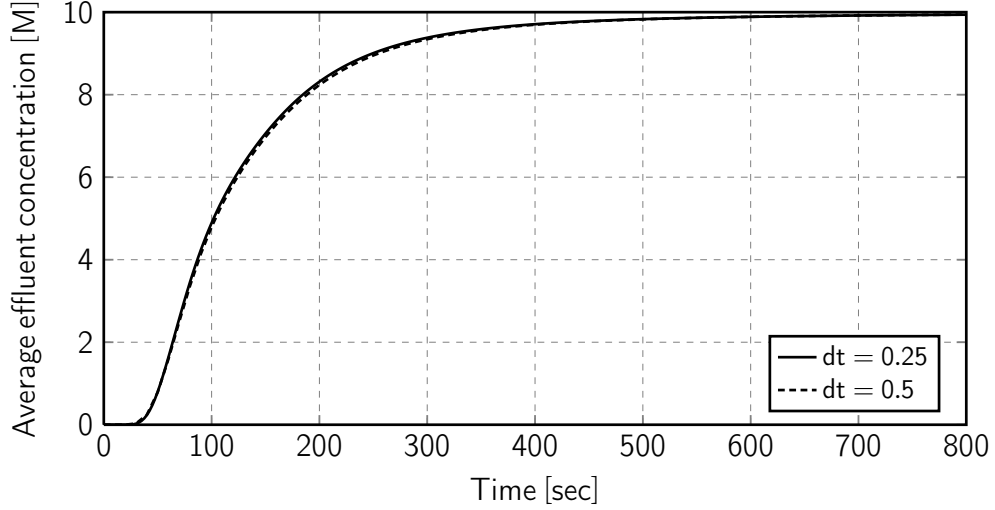


Figure 2.4: Criterion for choosing the time step for the transport calculations. For every time step we calculate the average effluent concentration of a solute as a function of the simulation time (see Section 2.3.3) and reduce the step until the resulting curve does not change.

2.2.6 Algebraic multigrid method

The 3D volumetric meshes, reconstructed from the porous sample computed tomography (CT) measurements, are characterized by a large number of nodes (of the order of millions). As can be seen from the structure of Eq. (2.13) it contains four times as many unknowns as the number of FE nodes. Therefore, highly efficient solvers are required to find an approximate solution for a linear system of this size. In our approach we use the algebraic multigrid library SAMG (Stüben and Clees, 2005), developed at the Fraunhofer Institute for Algorithms and Scientific Computing.

The two main principles of multigrid approach – error smoothing and coarse grid correction – are demonstrated on Fig. 2.5. Let us consider a linear problem $\mathbf{Ax} = \mathbf{b}$. On every grid Ω_h , starting with the finest level, an error smoothing operation (S_h) is applied first, where error $\mathbf{e} = \mathbf{x} - \tilde{\mathbf{x}}$ is a difference between exact (\mathbf{x}) and current ($\tilde{\mathbf{x}}$) solutions. This operation is intended to rapidly reduce the high-frequency component of \mathbf{e} . This is followed by projection (also called restriction, R_h^{2h}) of the solution to the next coarse level, where low-frequency error components of the previous fine level turn into high frequency errors again. Another smoothing step reduces \mathbf{e} further and another restriction takes place. The procedure is carried forward until the coarse level is small enough for the

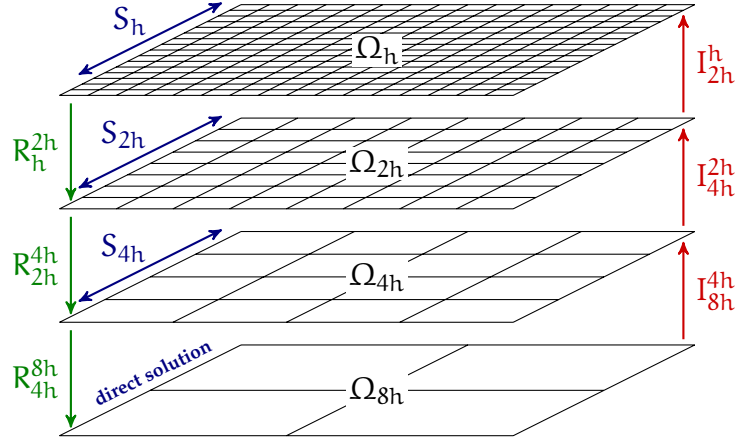


Figure 2.5: Schematic representation of a single multigrid cycle. Ω denotes multiple levels, S represents a smoothing step, R – restriction step, I – interpolation step. Direct solution is calculated at the coarsest level.

solution on it to be calculated exactly. It is then interpolated (I_{2h}^h) back to fine levels. The idea of AMG is to perform these operations directly on certain classes of sparse matrix equations. Therefore, in AMG method no geometric information needs to be available for the construction of the multilevel hierarchy. Coarse levels (Ω_{2h}), inter-grid transfer (R_h^{2h} , I_{2h}^h) and coarse level operators (S_{2h}) are built automatically, based purely on algebraic information explicitly or implicitly contained in the underlying matrix (such as size and/or sign of the matrix entries). This makes AMG especially suited for applications on unstructured grids where the implementation of geometric multilevel approaches is too complicated if possible at all.

SAMG approximates the problem $\mathbf{Ax} = \mathbf{b}$ iteratively using two-part process. The first part is the setup phase which recursively carries out four steps. First, the matrix connectivity is analysed. Second, based on this analysis a subset of unknowns is constructed to represent the next coarser level. Third, restriction and interpolation operators are established, which transfer information between different levels. Finally, the coarse-level matrix problems are assembled. The second part is a solution phase which uses the resulting components of the setup phase to carry out the iterative multigrid cycle, usually termed the V-cycle. One V-cycle employs stepping from the finest level to the coarsest one and back. On each level smoothing is performed so that coarser level can effectively contribute to improving finer level quantities. Cycling is carried out repeatedly until the trial solution $\tilde{\mathbf{x}}$ approximates the problem $\mathbf{Ax} = \mathbf{b}$ within numerical precision such that $\tilde{\mathbf{x}} \approx \mathbf{x}$.

This cycling on multiple grids has the advantage that the CPU time and memory requirements of algebraic multigrid solvers scale as $\mathcal{O}(n)$, where n is the number of unknowns, i.e. the size of \mathbf{x} . This is a significant improvement over direct, ILU or conjugate gradient solvers for which the amount of numerical operations increases as $\mathcal{O}(n^\alpha)$ where $\alpha > 1$.

The SAMG package is not just an AMG implementation for one particular problem type but rather a complete multilevel framework. Several setup strategies are available that cover various types of coupled systems of partial differential equations (PDEs). We found that in our particular case the solver works best if we use ILU factorization with no fill-in (ILU(o)) as a smoother in combination with a point-based coarsening approach and fluid pressure as a primary unknown. The former means that the matrix has to be reordered in a way described at the end of Section 2.2.3. The latter means that the construction of coarser levels of FE linear system from Stokes equation is performed based on the connectivity structure of the fluid pressure diagonal matrix blocks. Transfer operators are constructed for each unknown separately, following the standard AMG procedure for single-unknown problems (Brandt et al., 1982; Stüben, 1999). Finally, SAMG is not used as a stand-alone solver. Each V-cycle rather serves as a preconditioner for GMRES(20) (GMRES restarted in every 20 steps) iterative solver.

It is clear that the problem of direct 3D pore-scale modelling of fluid flow and transport is characterized by a large number of degrees of freedom and that this number quickly increases with the growth of the domain size. More formally, if we assume that Q represents a number of voxels per one dimension, then the total amount of degrees of freedom will scale as $n = \mathcal{O}(Q^3)$. The computational work scales, as described above, as $\mathcal{O}(n^\alpha)$, where α depends on the employed linear solver. As a result, the required computing time scales as $T = \mathcal{O}(Q^{3\alpha})$. Clearly, it is essential to use efficient solvers with the optimum scaling ($\alpha = 1$) if one wishes to work with the domains of a representative size. We, therefore, consider the algebraic multigrid solver a crux of our approach, that lets us bring the problem, that was until recently considered tractable only using large computer clusters, to the domain of problems manageable with desktop computers.

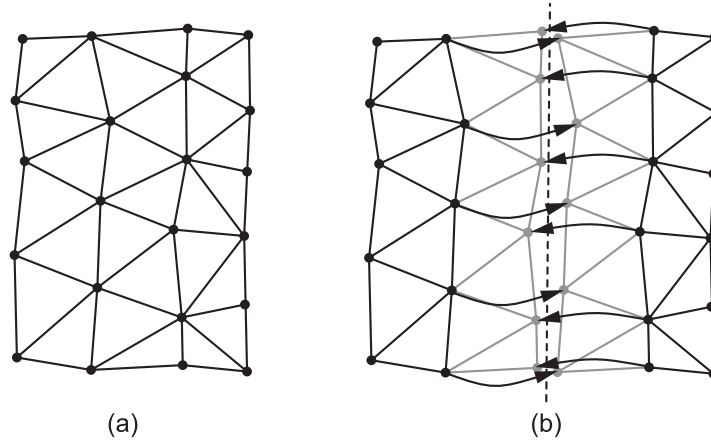


Figure 2.6: Partitioning of a FE mesh in 2D. Original mesh (a) is split into two sub-meshes (b). They overlap by a single layer of elements shown in grey colour. Arrows represent the inter-processor communication that involves sending and receiving values between the corresponding nodes of two partitions.

2.2.7 Parallel discretization

Despite the high efficiency of the AMG method, models that involve realistic 3D pore geometries can require an unpractical amount of memory and, to a lesser extent, computing time. Apart from algorithmic and hardware improvements, an effective mean of gaining a significant speedup is task parallelization (Coumou et al., 2008). In our code we employ the domain decomposition procedure to run 3D models on multiple processors. We use node-level graph partitioner METIS (Karypis and Kumar, 1998) to automatically decompose a domain into a number of adjacent subdomains. Each of them is then treated on a separate processor. The resulting partitions overlap by exactly one layer of elements (usually called *halo* elements) that represent the communication volume between processors (see Fig. 2.6). Since each processor includes halo elements in the evaluation of the local FE matrices, restricting the overlap to a single layer ensures that the memory overhead of domain decomposition is kept to a minimum. Therefore the overall memory requirements per computational node are reduced by a factor almost linearly proportional to a number of partitions. The information between individual CPUs is exchanged using the MPI protocol (Gropp et al., 1996). Fig. 2.7 demonstrates the result of partitioning of a complex 3D tetrahedral mesh in 16 subdomains. Each subdomain contains approximately the same number of elements so as to balance the computational load between individual CPUs.

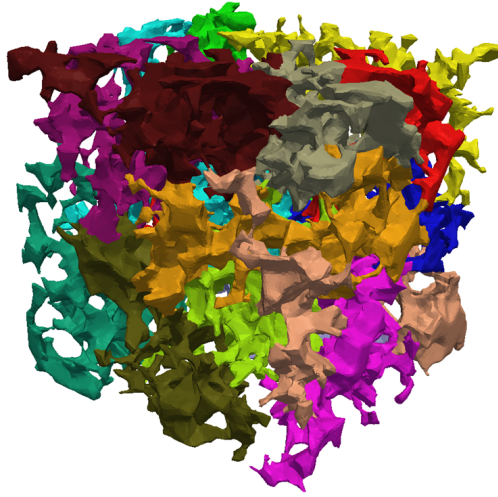


Figure 2.7: Partitioning of a 3D tetrahedral mesh representing the pore space of a sandstone sample in 16 subdomains of approximately equal size.

The SAMG solver has a parallelized counterpart – SAMGp (Krechel and Stüben, 2001). It is designed to take advantage of the matrices produced by domain decomposition, providing similar numerical behaviour and convergence properties as the sequential version. It has been observed that SAMGp scales almost as $\mathcal{O}(n/n_p)$, where n is again the number of unknowns and n_p is the number of processors, as long as this ratio is not less than 50k. When less than 50k degrees of freedom fall on each processor then, as the coarse levels are being generated, they become too small to be efficiently spread between all participating CPUs. Instead, coarse levels are joined together and treated on only a portion of all available processors, hence resulting in the load imbalance. In such a case, increasing the number of processors does not result in an increase of computational efficiency.

2.2.8 Mesh generation

In order to investigate the flow through a realistic pore geometry, one has to transform it into a proper finite element mesh. The first stage of this process is performing an X-ray computed tomography scanning of an actual porous sample. This experiment results in a spatial X-ray absorption profile of the sample. Based on the absorption contrast between a fluid and a solid one can infer the location of pores and grains with an error depending on the scanner resolution and create a 3D binary image of the sample (see Fig. 2.8a) (Dunsmuir et al., 1991). The next step

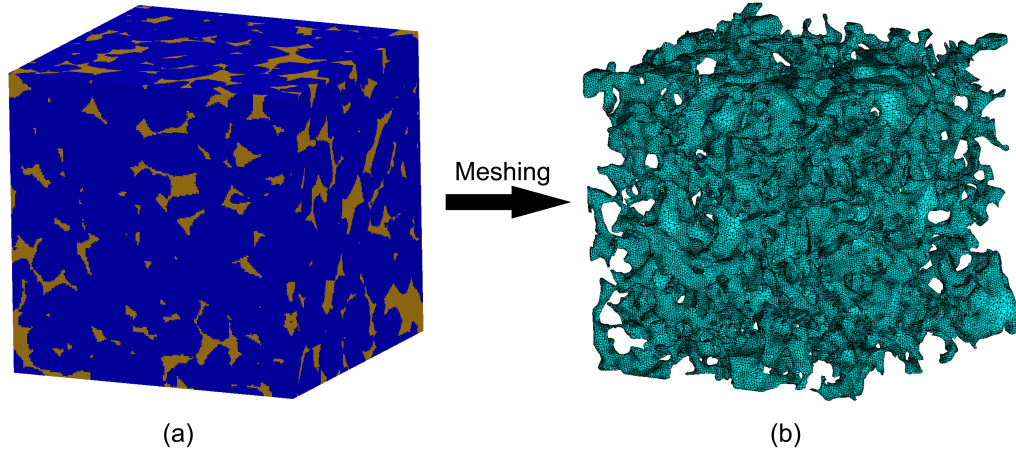


Figure 2.8: (a) Voxelized representation of a Fontainebleau sandstone sample obtained by thresholding the corresponding X-Ray CT data. Blue voxels denote solid space, brown ones denote pore space. Each voxel is a cube with the edges of $7.5 \mu\text{m}$. The overall size of the sample is 1.5 mm in each direction. (b) FE-2 mesh reconstructed from the voxelized data. The outer surface contains 763 thousand of triangles. The surface interior is filled with 3.3 million of tetrahedral elements (not shown).

is construction of a watertight isosurface (see Fig. 2.8b), which isolates the region of interest, i.e. pores from grains. Finally, the interior of the isosurface is filled with volumetric elements and this provides the FE mesh.

There are numerous algorithms for isosurface extraction, with the standard approach being the so-called marching cubes algorithm (Lorensen and Cline, 1987). However, this method is of limited applicability for our particular problem. First, it produces topologically inconsistent non-manifold surfaces. A two-manifold surface has a property that a small enough sphere around any point belonging to it will be divided into two parts that lie on the opposite sides of the surface. Non-manifold surfaces do not share this property, which in our case means that their volumetric interior is not continuous everywhere. Fig. 2.9 demonstrates the difference between a two-manifold and a non-manifold surface in 2D. A surface in Fig. 2.9b contains one node where the non-manifoldness occurs – a sphere of any radius centred at this node will be divided in more than two parts.

Another limitation of the marching cubes algorithm is that it produces surfaces with an excessively large amount of triangles, which can pose an obstacle for subsequent data processing by a volumetric mesher. In this work we use two different software packages to study the implications of a mesh construction step. The first one is the proprietary Mimics[®] soft-

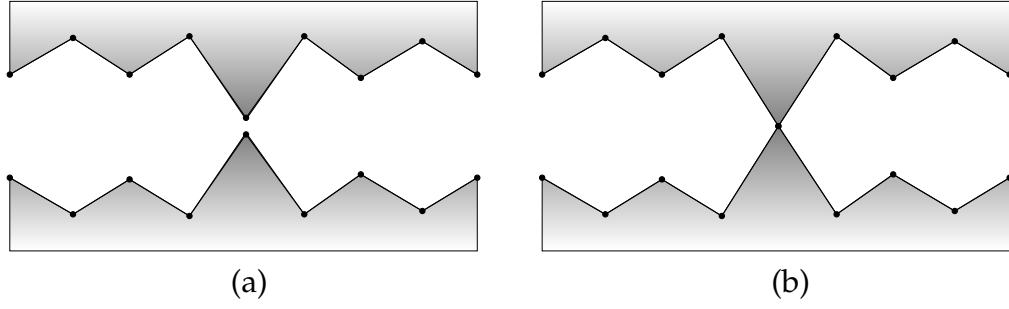


Figure 2.9: 2D representation of (a) two-manifold and (b) non-manifold surfaces. Surface meshes correspond to an idealized pore channel, the colour gradient marks solid boundaries.

ware by Materialise, which is a complete package with various algorithms to translate raw data from X-ray CT scans into a format suitable for finite element meshing. Mimics[®] provides its own implementation of a modified marching cubes algorithm, which is guaranteed to produce manifold meshes with a smaller degree of fragmentation. It also has a mesh optimization functionality to improve the isosurface quality in terms of the aspect ratio of its triangles. The second is a 3D mesh generation module from the open source CGAL library (Rineau et al., 2010). It avoids the isosurface stage and constructs the tetrahedral elements complex directly from the voxelized data, allowing for almost entirely automated mesh generation. The CGAL mesh generator constructs a 3D triangulation according to the restricted Delaunay triangulation paradigm. It offers a control over the quality of the tetrahedral elements in the generated meshes through the upper bound of the elements' linear size and over the geometrical conformity of the mesh boundary to the part of the CT data identified as pore space.

The efficiency and low memory requirements of CGAL complement our general approach of using the best available methods for the pore-scale modelling of fluid flow and solute transport. Its ability to directly mesh the CT images is invaluable for our purpose. Moreover, being an open-source C++ library, it can, in principle, be incorporated into our CSMP++ codebase and enable us to implement the adaptive grid refinement based on *a posteriori* error estimation as well as local domain remeshing when the boundary motion are accounted for.

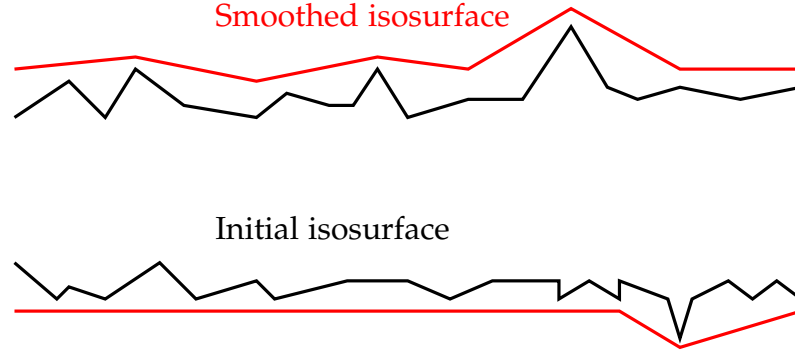


Figure 2.10: A simplified 2D representation of an initial rough isosurface (black) of a pore and an isosurface after smoothing (red). The amount of detail in a smoothed isosurface is significantly reduced but the resulting pore diameter is wider leading to an overestimation of the average permeability.

2.3 METHOD APPLICATION

We will now demonstrate the application of our numerical procedure to investigate the flow properties and emerging transport characteristics in a 3D Fontainebleau sample. Fontainebleau sandstones are characterized by a very narrow distribution of grain sizes with an average grain having a diameter of 250 microns. Their homogeneity makes these sandstones particularly suited for measuring the pore space geometry using X-ray computed tomography.

2.3.1 Reconstructed 3D meshes

Fig. 2.8 demonstrates the application of a mesh generation workflow to a Fontainebleau sandstone sample. The sample has the dimensions of $1.5 \times 1.5 \times 1.5 \text{ mm}^3$, a permeability of $1.19 \times 10^{-12} \text{ m}^2$ and a porosity of 13.5% (Jiang, 2008). The CT scanner resolution is $7.5 \text{ }\mu\text{m}$, therefore the resulting 3D image of the sample has the size of 200 voxels in all 3 directions.

The mesh generated with CGAL library contains 3.1 million tetrahedra and 932 thousand nodes. The calculated porosity of this FE mesh is 13.2%, which is slightly lower because CGAL mesher discards the regions of isolated pore space. We will refer to this mesh as FE-1. For this work the upper boundary for the tetrahedra size was set to 1.5 voxels and the spatial deviation between the mesh boundary and the CT data boundary was limited by 0.2 voxels.

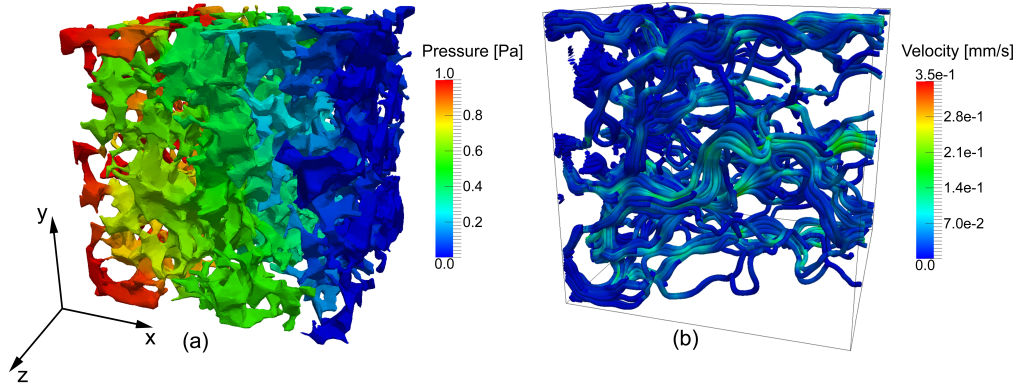


Figure 2.11: (a) Fluid pressure and (b) velocity distributions along the porous sample, obtained from the solution of the Stokes equations. Velocity is represented as streamlines.

The isosurface from Mimics[®] contains 474k triangles and 236k vertices. The surface was consequently processed using the ANSYS ICEM CFD[®] software to generate the volumetric mesh, representing the pores, with 3.3 million tetrahedra and 763k nodes. This mesh will be referred to as FE-2. The calculated porosity of the FE-2 is 17%. This discrepancy can be explained by the isosurface extraction process which used an option that reduces experimental noise but at the same time increases the diameter of the pores slightly (see Fig. 2.10). However, due to limited access to the Mimics[®] software, we were not able to modify the mesh once this difference has been found. Moreover, we use this mismatch as an instructive example of the sensitivity of pore-scale fluid flow predictions to the tiny changes of pore geometry.

2.3.2 Pressure and velocity profiles

For calculating the velocity distribution, a pressure gradient of 1 Pa was applied across the sample in the x direction. The fluid had a uniform viscosity of 10^{-3} Pa·s. No-slip conditions were assigned to the grain boundaries, as well as the the domain boundaries parallel to the x axis. The mesh was partitioned into 16 subdomains. The computing facility, used to run the calculation, was the Heriot-Watt University Cluster, which consists of 40 AMD Opteron 875 nodes, each supplied with 4 GB of RAM. Every computing node can run up to 4 jobs simultaneously. The peak memory requirement for our simulation was 6.5 GB. Hence we had to run the simulations in parallel, although they could be performed on a 64-bit desktop PC with 8 GB RAM equally well. Since the Heriot-Watt Cluster

only allows for non-dedicated simulations, i.e. it is not possible to reserve entire CPU nodes and their RAM for a simulation, we used 16 processors to ensure that we always have sufficient memory available. The required CPU time was 2 minutes to solve the linear problem (2.13) with 3 million degrees of freedom. The scaling behaviour of SAMGp (Coumou et al., 2008; Krechel and Stüben, 2001) suggests that the CPU time will increase linearly with the decrease in processors, i.e. approximately 4 minutes will be needed to solve the linear problem with 8 processors etc. This is still significantly faster compared to the LB method because we do not need to solve a transient problem.

The results for pressure and velocity distribution within the pore space are shown on Fig. 2.11. Velocity is represented along the streamlines emerging from the inlet boundary. Streamlines effectively represent the preferential flow paths of an imaginary tracer, transported by the fluid. They can be subsequently used as an alternative method of the solute transport simulation (Mostaghimi et al., 2010). These paths do not cover the whole pore space, as the intricacy of pore geometry inevitably leads to some pores being stagnant, i.e. no flow occurs in them. Another consequence of the pore space structure is that the flow with the maximum velocity magnitude takes place not inside the narrowest throats, which is the case, for instance, in a steady flow through a single tube of variable radius. Instead the fluid favors wider and less resistant throats. In order to demonstrate these effects more clearly, Fig. 2.12 presents a complementary 2D velocity distribution, which corresponds to a photomicrograph of a grainstone sample with the dimensions of $10 \times 6 \text{ mm}^2$.

Based on velocity distribution, one can estimate the resulting permeability of the sample by integrating the velocity vector over the outflow boundary Γ_{out}

$$k = \frac{\mu L \int \mathbf{u} \cdot \mathbf{n} d\Gamma_{\text{out}}}{A(p_{\text{out}} - p_{\text{in}})}, \quad (2.32)$$

where

- A area of the sample cross-section normal to the flow, $[\text{m}^2]$
- L sample length, $[\text{m}]$
- $p_{\text{in/out}}$ pressure values at the inflow/outflow boundaries, $[\text{Pa}]$

These calculations yield a permeability value of $0.71 \times 10^{-12} \text{ m}^2$ for FE-1 mesh and $3 \times 10^{-12} \text{ m}^2$ for FE-2 mesh. Since these values differ by a factor of 4, we also ran a LB simulation on the voxelized representation

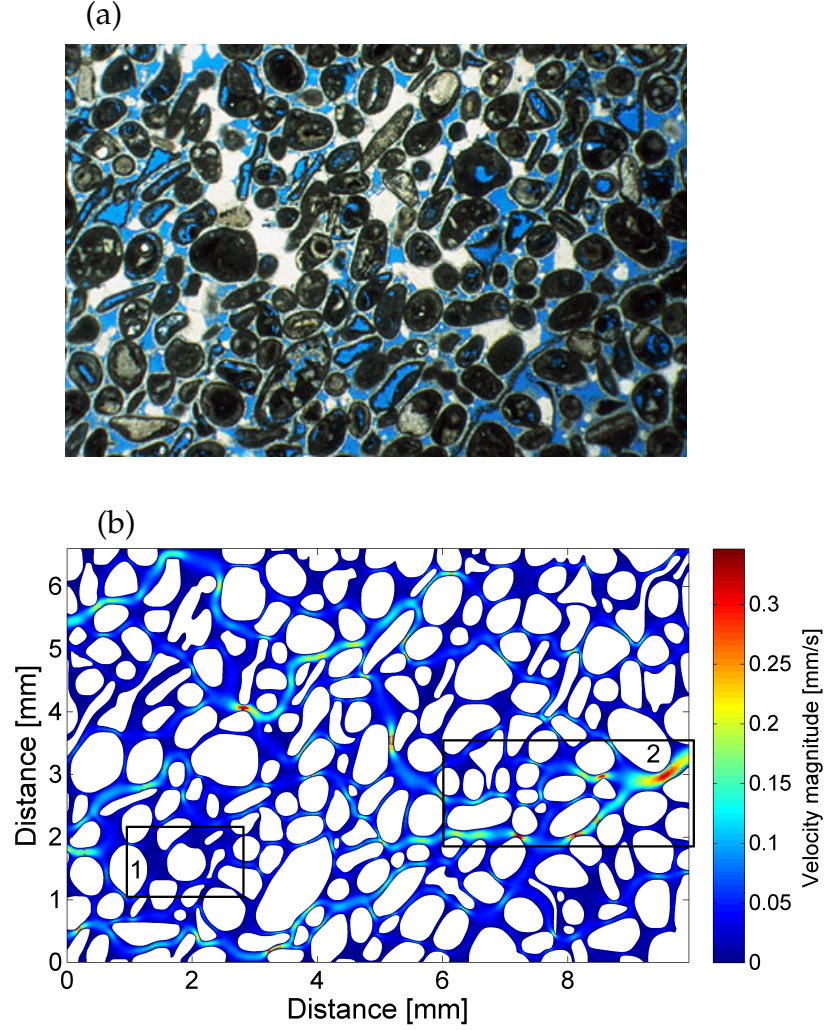


Figure 2.12: (a) Grainstone photomicrograph and (b) a fluid velocity distribution across a corresponding 2D mesh. Region 1 represents a stagnant area where velocity is low. Region 2 demonstrates the development of a preferential flow path.

of the same sample using the SHIFT scheme (Ma et al., 2010) and the same lateral boundary conditions. A relaxation time was taken equal to unity, which makes the permeability to be least affected by viscosity (Pan et al., 2006). The resulting LB permeability is $0.66 \times 10^{-12} \text{ m}^2$, which is very close to a result obtained with the FE-1 mesh. Permeability values are summarized in Table 2.1. For the sake of time comparison, LB calculation of permeability took about an hour to converge. This result allows us to make two conclusions.

First, the discrepancy between numerical values and an experimental permeability of $1.19 \times 10^{-12} \text{ m}^2$ is not inherent to the FE modelling approach, but is rather a consequence of a limited sample size. Indeed, as demonstrated by Jiang (2008), the representative elementary volume (REV)

size for this particular sample is $V_{\text{REV}} = 6.8 \text{ mm}^3$, while we had access to a portion of data with a volume of $V_{\text{REV}} = 3.38 \text{ mm}^3$. Since the sample is smaller than the REV scale, a no-slip boundary condition on the lateral sides of the domain that introduces an additional drag may further reduce the permeability value, as demonstrated by Gerbaux et al. (2009). Finally, as shown by Jiang (2008), who studies the same sandstone sample, when a domain exceeding the REV size is taken, the LB method yields a permeability of $1.28 \times 10^{-12} \text{ m}^2$, a result much closer to an experimental value.

Second, the permeability mismatch demonstrates that isosurface reconstruction step has to be treated with care. Though an isosurface generation can be seen as an attempt to restore the geometry information from the jagged voxelized CT data, it is a post-processing procedure and can introduce geometrical errors. In our case the noise reduction procedure of Mimics[®] effectively reduced the CT resolution while CGAL isosurface was a by-product of the 3D mesh generation and as such was conformal to the CT data with a minimal degree of smoothing. It should be noted that the voxelized X-ray CT data is already an approximate representation of the original pore geometry and the accuracy of the computed permeability will not only depend on the accuracy of the numerical method but also on the quality of the CT data, the segmentation and smoothing algorithms and other factors.

2.3.3 Solute transport

The modeled single-phase velocity distribution can be used to calculate the hydrodynamic dispersivity of the porous sample, which describes the effective parameter to model solute transport of the macro, i.e. continuum,

SOURCE	PERMEABILITY VALUE (m^2)
Experimental	1.19×10^{-12}
FE-1 model	0.71×10^{-12}
FE-2 model	3.0×10^{-12}
LB model	0.66×10^{-12}

Table 2.1: Permeability values obtained experimentally and from different numerical models.

scale. Dispersivity in porous media results from the interplay of Brownian motion of the solute molecules, i.e. molecular diffusion, and the velocity differences among different streamlines, i.e. mechanical dispersion. In this section we will demonstrate how our model can capture the effects of this interplay consistently with the experimental findings (Fried and Combarnous, 1971).

In order to estimate the sample dispersivity, we first solve the ADE, using the procedure outlined in section Section 2.2.5. From this we obtain a spatial distribution of a solute concentration $C(\mathbf{x}, t)$ at each time step. We can therefore calculate the average breakthrough concentration $\bar{C}(t)$ by integrating $C(\mathbf{x}, t)$ across the outflow boundary Γ_{out} , weighted with a local flux value

$$\bar{C}(t) = \frac{\int C(\mathbf{x}, t) \mathbf{u}(\mathbf{x}) d\Gamma_{\text{out}}}{\int \mathbf{u}(\mathbf{x}) d\Gamma_{\text{out}}}. \quad (2.33)$$

We then find the least-squares fit of the Ogata-Banks analytical solution of a 1D advection-diffusion equation (Ogata and Banks, 1962) to the resulting breakthrough curve

$$C_{\text{OB}}(t) = \frac{C_o}{2} \left[\text{erfc} \left(\frac{L - Ut}{\sqrt{4Dt}} \right) + \exp \left(\frac{LU}{D} \right) \text{erfc} \left(\frac{L + Ut}{\sqrt{4Dt}} \right) \right], \quad (2.34)$$

where

- C_o fixed inflow concentration, [mol/l]
- U mean flow velocity, [m/s]
- D (longitudinal) hydrodynamic dispersivity, [m²/s]

The above-mentioned interplay between convection and molecular diffusion is expressed in terms of a throat Peclet number $Pe = Ua/D_m$, where a is a characteristic length of the sample. In this particular case we took a equivalent to a mean Fontainebleau sandstone grain size of 250 microns. Low Peclet numbers correspond to the diffusion-dominated flow regime, while high ones are characteristic of convection-dominated regime. Experimental studies (Fried and Combarnous, 1971) suggest that in the first regime dispersivity decreases with velocity, if all other parameters are equal. In the latter regime it increases slowly with velocity. By changing the imposed pressure gradient and the molecular diffusivity we can verify this dependency between the Peclet number and an upscaled sample dispersivity.

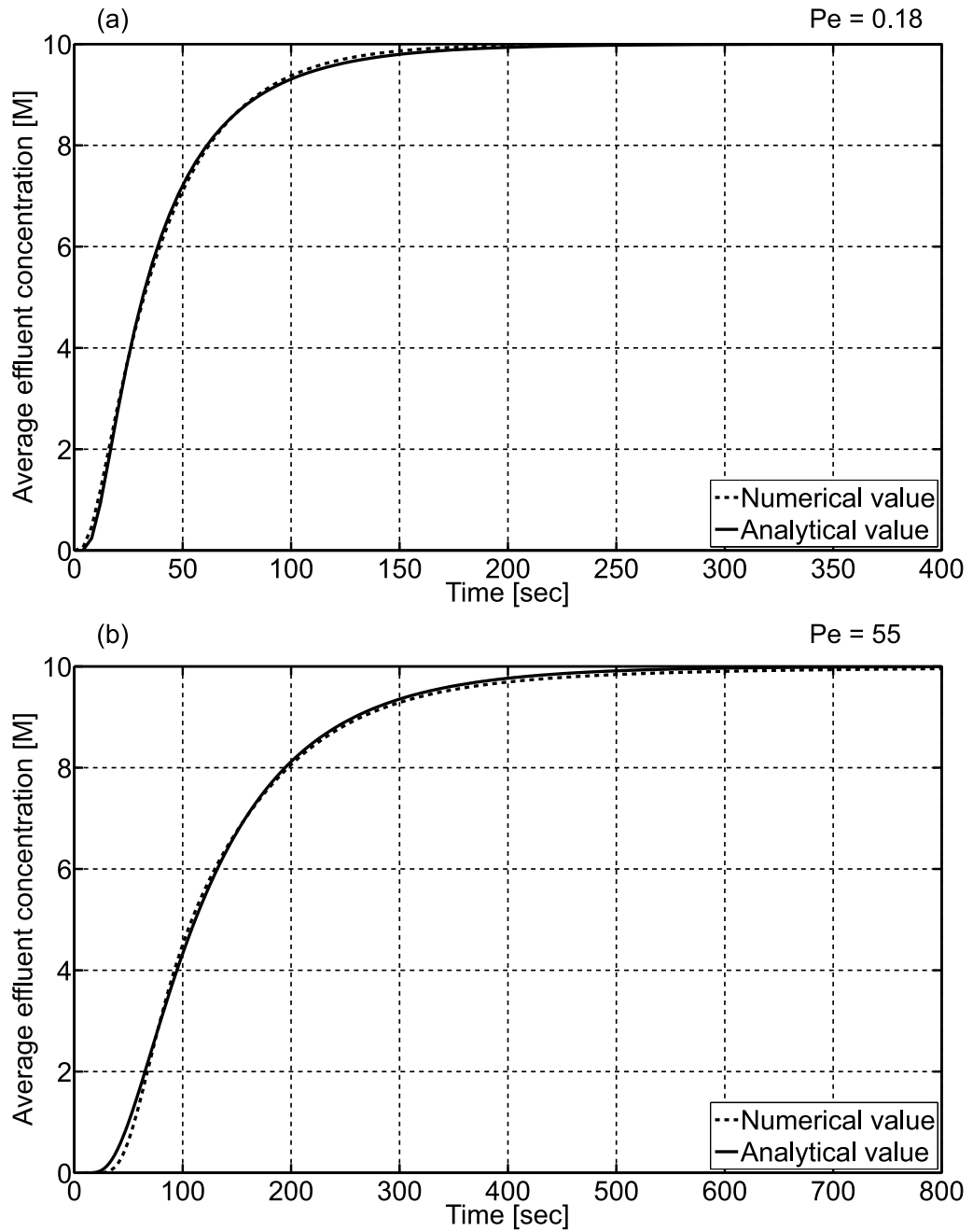


Figure 2.13: Flux-weighted breakthrough curves, corresponding to Peclet numbers $Pe = 0.18$ (a) and $Pe = 55$ (b). High Peclet numbers characterize a convection-dominated regime in which case long tailing occurs. That is, the concentration takes a longer time to reach the maximum value than predicted by the analytical solution.

Fig. 2.13 demonstrates two breakthrough curves that correspond to the diffusive ($Pe = 0.18$) and convective ($Pe = 55$) flow regimes, respectively. Though both curves are well approximated by an analytical solution (2.34), a close inspection of the second ($Pe = 55$) curve reveals that the concentration does not reach its maximum inflow level within the time span of the modelling. As indicated by Salles et al. (1993), the size necessary for a breakthrough curve to have no tailing, is linearly proportional to the Peclet number. When the solute diffuses away from the major flow paths it becomes trapped or delayed within stagnant zones (Haggerty and Gorelick, 1995). If the solute diffusivity is low (i.e. Peclet number is high), it takes a significant amount of time for the solute to diffuse back to high-velocity streamlines and hence causes the tailing effect. In case of higher (molecular) diffusivity, e.g. thermal diffusion, this heterogeneity effect becomes less dominant and the tailing is reduced. This essentially determines the REV size of a sample for the transport modelling. Salles et al. (1993) suggests that no tailing will occur when the sample's linear size L is larger than

$$L > 10 Pe \cdot a. \quad (2.35)$$

Therefore, the sample whose size is sufficient for determining the permeability value may be too small for the solute transport calculations.

Fig. 2.14a shows the calculated FE-1 and FE-2 samples' dispersivities for a wide range of throat Peclet numbers. It should be noted that in both cases we used the same average grain size value a for calculating the Peclet number which is justified by the fact that the relative difference of this parameter between FE-1 and FE-2 is close to one. The results are plotted in a dimensionless fashion as $\log_{10}(D/Ua)$ versus $\log_{10}(Pe)$ (Acharya et al., 2007; Bijeljic et al., 2004; Fried and Combarnous, 1971; Sorbie and Clifford, 1991). This way points corresponding to different values of molecular diffusivity collapse onto a single curve. The overall form of this curve for the FE-2 mesh compares very well with the experimental results (Fried and Combarnous, 1971), which demonstrates that our code captures this well-known emergent behavior. At values of $Pe < 1$, the curve has a negative slope because dispersion is almost constant in the diffusion-dominated regime. A minimum in the value of D/Ua is predicted in the range $1 < Pe < 10$ which is also found experimentally (Fried and Combarnous, 1971). For $Pe > 10$ the slope turns

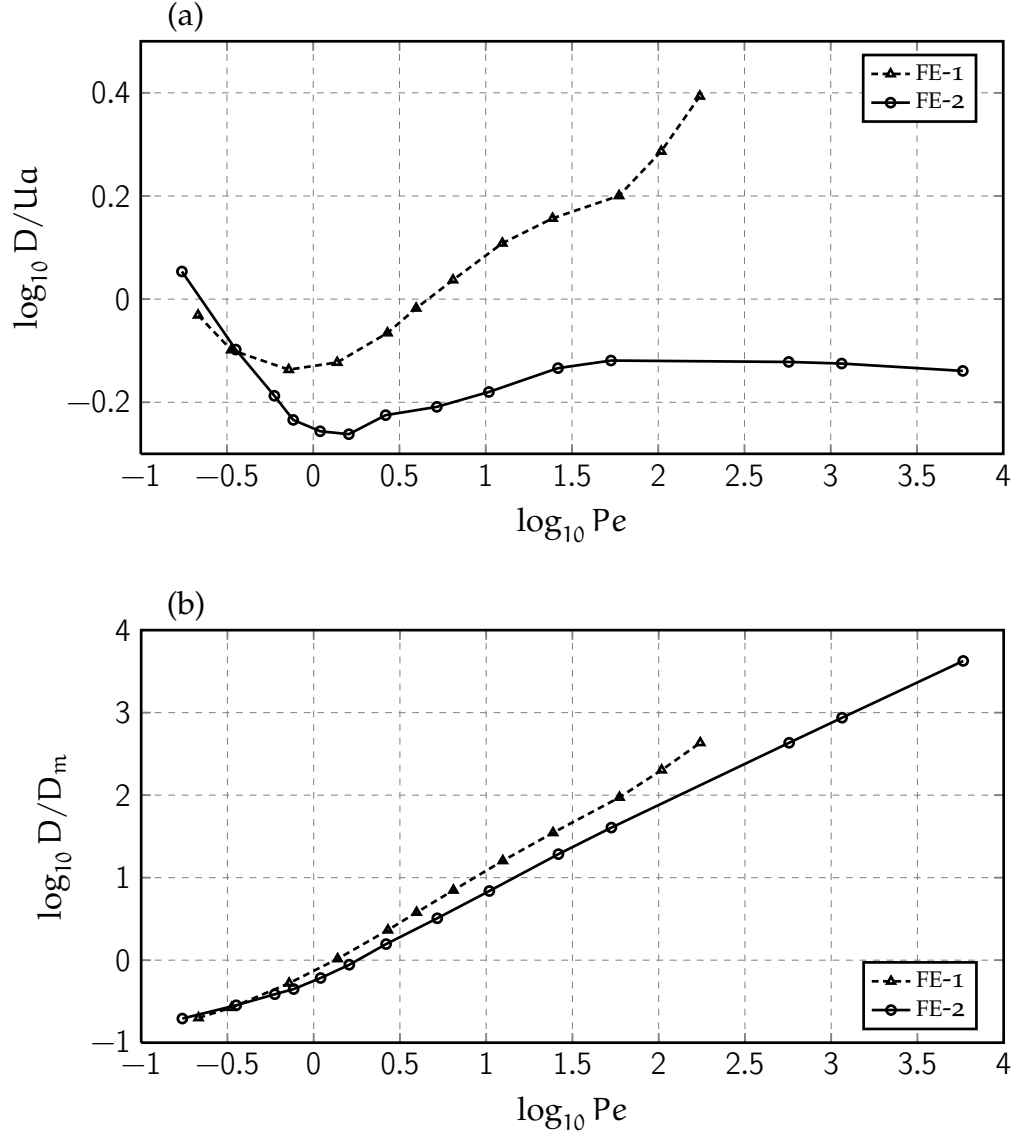


Figure 2.14: (a) Dispersivity versus throat Peclet number $Pe = Ua/D_m$ plotted in a dimensionless fashion as D/Ua . The shape of the curve reflects the transition from the diffusion- to convection-dominated regime of the fluid flow. (b) Dispersivity versus throat Peclet number $Pe = Ua/D_m$ plotted as D/D_m . Two curves correspond to conformant (FE-1) and slightly inflated (FE-2) meshes.

positive corresponding to the regime where mechanical dispersion is prevalent but where molecular diffusion cannot be ignored. At Pe values greater than ~ 1000 the slope approaches zero. This is where dispersion is purely mechanical and D is, theoretically, linear to U (Brenner, 1980). The observed decline at $Pe > 10^3$ occurs because the tailing of breakthrough curves leads to a poorer fit of numerical calculations against Eq. (2.34) and hence a deviation of D/Ua from the expected behavior. It should also be noted, that points on Fig. 2.14 were calculated by varying both velocity and molecular diffusivity to verify the consistency of the dimensionless plot, i.e. that the cases corresponding to different diffusivities but same Peclet number result in the same value of D/Ua . The results for the FE-1 sample demonstrate the correct behaviour in the low and intermediate Pe ranges, albeit with the higher levels of dispersivity at the same values of Pe as compared to the FE-2 mesh. However, for high Peclet numbers the behaviour of dispersivity is drastically different from that for the FE-2 sample. This is discussed below.

The curve in Fig. 2.14a emphasizes the transition between three different flow regimes. Another way to plot the transport modelling results is in the $\log_{10}(D/D_m)$ versus $\log_{10}(Pe)$ scale, which allows easier quantitative comparison with other works dealing with the porous media dispersion. This plot is presented in Fig. 2.14b for both FE-1 and FE-2 meshes. Fig. 2.14b agrees well in terms of dispersivity magnitude with the results on longitudinal dispersion compiled by Bijeljic et al. (2004). At low Peclet numbers diffusion drives the solute propagation and therefore the effective dispersivity is lower than molecular diffusivity ($\log_{10}(D/D_m)$ is negative) as the pore space restricts the solute movement. The slope of the curve in this region gradually approaches zero as the very low Pe dispersivity depends only on formation resistivity factor and porosity (Sahimi and Islam, 1995). Again, at the mixed-flow regime convection-diffusion interplay is the most pronounced and hence the curve has a slope higher than unity.

Both figures demonstrate a difference in the transport properties between the two meshes. For the FE-1 sample we observed that at around $Pe > 200$ the breakthrough curves shows a strong non-Gaussian behavior with long tailing and that they can no longer be approximated with the Ogata-Banks solution. This is in agreement with the above-mentioned discussion on non-Gaussian dispersion behavior by Salles et al. (1993) and shows that the sample size is far below the transport REV scale at

$Pe > 200$. We believe that the drastic difference in the dispersivity behaviour originates due the fact that the FE-1 sample has narrower pore throats than the FE-2 sample, and hence contains more streamlines that do not reach the outflow boundary. In the case of small diffusivity (i.e. high Pe) when a solute particle starts moving along a dead-end streamline there is a low probability of it reaching the other side of a sample and therefore outflow concentration rises very gradually. Another possible source of such a discrepancy is the fact that the FE-1 is characterized by a rougher grain surface (see Fig. 2.10) with a very low fluid velocity inside the surface kinks. If a solute particle is brought into these low-velocity regions, it again has low probability of returning back to the flow. All in all, this is an open question that requires further research but it is outside the scope of the present work.

As a result of this, the behaviour of the dispersivity D in Fig. 2.14a does not reflect the experimental findings and is not linearly proportional to the mean velocity U . In Fig. 2.14b the difference between FE-1 and FE-2 again manifests itself in the dispersivity magnitudes and also the power law coefficient δ between D/D_m and Pe (a slope in the logarithmic scale). The results are $\delta = 1.23$ for FE-1 and $\delta = 1.1$ for FE-2 for the $10 < Pe < 200$ region. This further illustrates the sensitivity of pore-scale modelling results to the proper construction of the numerical domain. The power law coefficient describes the influence of diffusion from the low-velocity boundary layers on the overall sample dispersivity. The widening of pore channels in FE-2 mesh reduced the rate of this diffusion and thus resulted in a lower value of δ . Other studies on numerically reconstructed Fontainebleau sandstones report the power law coefficient of $\delta = 1.34 - 1.56$ (Salles et al., 1993). However, a subsequent work by Yao et al. (1997) demonstrated that the numerical approach employed for estimating the sample dispersivities in (Salles et al., 1993) and Yao et al. (1997) yielded a consistently higher power law coefficient as compared to the experimental measurements. For the sake of comparison, published experimental results on power law coefficient in Berea sandstones range from $\delta = 1.13$ (Gist et al., 1990) to $\delta = 1.33$ (Kinzel and Hill, 1989), which suggests that both values computed in this work are physically quite reasonable. Finally, it is worth indicating that in most publications on the dispersivity simulations the results are published in the $\log_{10}(D/D_m)$ versus $\log_{10}(Pe)$ scale. Our results demonstrate that even when the results look reasonable in this scale, care should be taken as they can still be

unphysical in the sense that the transition between various flow regimes is not captured properly due to the sample size limitations.

One important application of the procedure described here is an analysis of the relation between the molecular diffusivity of a solute in bulk water D_m and the diffusivity of the same solute in saturated porous media D_{pm} in the absence of advection. This relation is crucial in the performance assessment of underground disposal systems for the radioactive waste. The average macroscopic diffusion coefficient is defined as (Skagius and Neretnieks, 1986)

$$D_{pm} = \phi\delta/\tau^2 \times D_m, \quad (2.36)$$

where

- ϕ diffusion-accessible porosity, [–]
- δ constrictivity, [–]
- τ tortuosity, [–]

Porosity and constrictivity can be determined from the geometrical structure of the porous sample, while tortuosity can be obtained by calculating the stationary velocity profile and the corresponding streamlines (Matyka et al., 2008). The average diffusion coefficient can be computed by tracking the spatial evolution of the solute concentration within the sample when no advection occurs. Hence the validity and the range of applicability of the aforementioned relation can be studied.

2.4 SUMMARY

In this chapter we presented a direct pore-scale procedure for modelling the single-phase fluid flow and transport in reconstructed 3D porous medium. The key elements of this procedure are:

1. a FE solution of the stationary Stokes equation on unstructured meshes for an accurate representation of domain geometry;
2. an algebraic multigrid method for solving the resulting FE linear problem, which offers a linear number-of-operations scalability with respect to mesh refinement and hence significantly mitigates the computer resources limitation factor;
3. an optional domain decomposition for problem parallelization;

4. a combined FE-FV technique for solving the transient inert transport problem.

The main novelty of our approach to modelling the pore-scale physics is the implementation of numerical methods that are best suited for our purpose. By utilizing an unstructured mesher that works directly on the CT data, stable first-order discretization schemes for the governing PDEs and a state-of-the-art algebraic multigrid solver, we for the first time bring the problem of direct pore-scale fluid flow and solute transport within the reach of research groups that do not have access to computer clusters with hundreds of computing nodes. By applying this procedure to a reconstructed Fontainebleau sandstone sample we were able to demonstrate that the FE solution yields the same permeability value as the LB method while requiring a fraction of time necessary for the LB solution to converge. We also highlighted the detrimental effect of reducing the amount of geometrical data by means of excessive domain boundary smoothing. This implies that given an accurate mesh of a domain it is much more preferable to use the FE-based method of calculating the resulting permeability than the currently more wide-spread LB approach.

Transport modelling demonstrated the correct transition between various flow regimes from diffusion- to convection-dominated and gave quantitatively similar results when upscaled sample dispersivity was compared to other published results. It also showed a slight decrease in the sample dispersivity as well as in the relative contribution of diffusion in the mixed flow regime in the case of a mesh with inflated pore throats. Finally, we observed that a mesh reconstruction procedure determines the onset of the breakthrough curves tailing with respect to the Peclet number.

In the next chapter we will discuss how our pore-scale model can be extended to include the effects of chemical reactions such as mixing and interaction between the solute and the rock.

Results of this chapter were presented in the following peer-reviewed publication:

- Y. Zaretskiy, S. Geiger, K. S. Sorbie, and M. Förster. Efficient flow and transport simulations in reconstructed 3D pore geometries. *Advances in Water Resources*, 33(12):1508-1516, 2010

PORE-SCALE MODELLING OF REACTIVE TRANSPORT

CONTENTS

3.1	Introduction	56
3.2	Numerical method	59
3.2.1	Chemical reactions	60
3.2.2	Distance field calculation	62
3.3	Example application	73
3.4	Summary	79

3.1 INTRODUCTION

In Chapter 2 we considered the transport of an inert solute, where the local solute concentration can change either due to fluid advection or as a result of molecular diffusion. However, many real-life transport phenomena also involve the chemical interaction between different species dissolved in the fluid or between the fluid and the rock. In what follows we will discuss how these effects can be incorporated in a numerical simulation.

The dynamics of chemical reactions in porous media is pertinent to a wide range of reservoir engineering problems including CO₂ sequestration (Durucan and Shi, 2009), contaminant transport (Chern and Chien, 2003), chemically enhanced oil recovery (Strand et al., 2006), or mineral scale formation during oil production (Sorbie, 2010). The associated spatial and temporal evolution of reactive species within the porous rocks is often difficult to measure across the relevant scales and hence it is important to develop the appropriate numerical models that allow us to quantify and upscale these phenomena. Numerical models can, for instance, facilitate the design of an enhanced oil recovery procedure and predict the future behavior of the system such as the distribution of species within a porous medium.

In modelling reactive transport, the porous medium itself can be described with an explicit geometry, as a set of grains and voids, or it can be treated as a continuum, characterized by average properties. The latter approach is more efficient in terms of computational efforts and usually implies that the evolution of chemical species is governed by the advection-dispersion-reaction equation

$$\phi(\mathbf{x}, t) \frac{\partial C_i}{\partial t} + \nabla \cdot (\mathbf{u}(\mathbf{x}, t) C_i) - \nabla \cdot (\mathcal{D}(\mathbf{x}, t) \nabla C_i) = R(C_1, \dots, C_n, \mathbf{x}, t), \quad (3.1)$$

where

C_i	concentration of the species i , [mol/l]
$\phi(\mathbf{x}, t)$	porosity (scalar) field, [–]
$\mathbf{u}(\mathbf{x}, t)$	velocity (vector) field, [m/s]
$\mathcal{D}(\mathbf{x}, t)$	dispersivity (tensor) field, [m ² /s]
$R(C_1, \dots, C_n, \mathbf{x}, t)$	generic reaction term, [mol/(l·s)]

Akin to the case of inert solutes in Chapter 2, this kind of transport description requires knowledge of the relevant effective properties of the medium, such as porosity, permeability, dispersivity, reactive surface area, etc. As a result, such an approach cannot be used to describe the solute flow *a priori*. Instead, empirical relations between parameters are used, such as Kozeny-Carman relation (Carman, 1937, 1956; Kozeny, 1927), which describes the evolution of permeability as a function of porosity. In addition, this description assumes that the reactants are well-mixed and does not resolve any local distribution and flow focusing effects due to the porous medium's microstructure. As an alternative, models with an explicit pore geometry description do not rely on averaged macroscopic parameters and can model the temporal and spatial localizations of reactions at the pore scale, which can then be used to derive appropriate effective parameters on the continuum scale.

Since it has been established experimentally that the change of brine composition can trigger the enhanced oil recovery during waterflooding of chalk rocks, this process clearly involves certain chemical interactions between the brine and the porous rock. Therefore, one cannot simulate this process without treating the transported solutes as reactive. Moreover, the process involves two fluid phases and as such an influence of the brine composition on the oil-water interface properties cannot be ex-

cluded either. Consequently, a complete numerical model of this problem should couple two-phase flow and reactive solute transport components. As indicated in the introduction of this thesis, currently no method is available that can adequately simulate both phenomena. Furthermore, there is no clear physical understanding of the nature of the link between the brine composition and the two-phase flow. Therefore, in this chapter we follow both avenues in terms of how they can be modelled within the FE-FV framework, but, as will be seen in the next chapter, we will mainly concentrate on simulating the single-phase chemical interaction between the brine and the rock. The problem of existing second fluid phase is presented only as a proof of concept and the approach to this problem is simplified – we only show how we can account for its presence in the form of immiscibly trapped oil blobs rather than simulating the complete transient two-phase transport. More specifically, in this chapter

1. We present a computationally efficient approach to simulate single-phase fluid flow and reactive solute transport at the pore scale in porous media. We extend the inert transport model from Chapter 2 and introduce the fluid-solid interaction in the form of a non-linear adsorption. The reaction step is decoupled from the rest of the calculations and hence alternative chemical reactions can be modeled in a similar fashion, either coded manually or by linking an external chemical software package (see, for instance, PHREEQC (Charlton and Parkhurst, 2011), GEM-Selector (Kulik et al., 2003)) with the flow solver. We do not include any chemical reactions in our simulations that are specific to waterflooding of chalk rocks as we devote the next chapter to identifying exactly what these reactions are.
2. In addition to the generic description of reactive transport modelling, we describe a method of determining the pore size distribution within an unstructured numerical domain, based on calculating a distance map of a domain. The presented technique in itself is a first reported extension of the method of maximal inscribed spheres proposed by Silin and Patzek (2006) to the unstructured FE meshes. As such it can, in principle, be used to simulate the capillary pressure curves directly from the CT data. In the context of two-phase pore-scale reactive transport modelling, it does not offer a way to model the *dynamics* of the oil phase, but it offers means to account

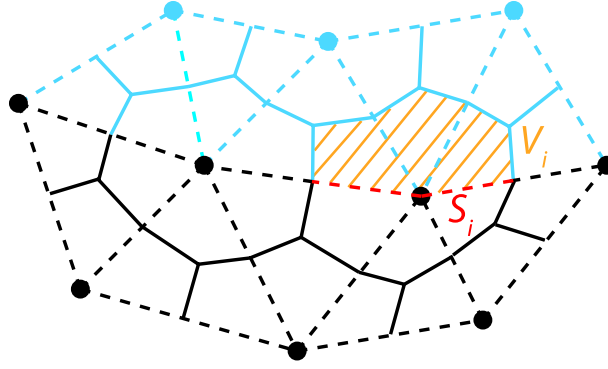


Figure 3.1: Relation between a 2D finite element mesh (dashed), a node-centred finite volume mesh (solid), nodal surface (red line), and nodal volume (orange area). Black and blue colors are used to distinguish between the fluid and grain parts of the domain (see also Fig. 2.3).

for its *presence*. Therefore, provided that we know what chemical conditions trigger the wettability change, it allows us to use pore-scale modelling to analyse whether these conditions occur, where they occur and how they are influenced by the flow of the aqueous phase.

3. Finally, we briefly demonstrate how our distance-based method can be used to place the oil blobs in the pores based on the rock wettability and to subsequently model the reactive solute transport within the aqueous phase, including the micron-scale water films that may surround the oil blobs. The model is rather simple as it accounts for a single solute that can adsorb onto the water-rock surface. Oil-water and oil-rock interactions are not considered. Even with an simple model we highlight an issue that the high affinity of a solute towards the rock surface may limit the solute's propagation towards the oil/water/rock contact lines and reduce the effectiveness of a potential EOR technique. However, more elaborate analysis requires the exact knowledge of the chemical effects that determine the oil/water/rock interaction.

3.2 NUMERICAL METHOD

The main difference between modelling inert (see Chapter 2) and reactive transport phenomena, as far as meshing is concerned, is that in the latter case we store additional information about the grains boundaries in the form of a triangulated surface aligned along the grains (red region in

Fig. 3.1). This surface mesh allows for easier calculation of the surface area associated with every boundary node and, more importantly, it provides means for modelling additional surface effects, namely diffusion along the surface films formed by the wetting fluid. This is accomplished by assigning a nominal thickness to the triangular elements and including them in the diffusion step of the transport calculation (see Eq. 2.25). This capability is important in modelling the scenario in which the pore is occupied by a non-wetting fluid, but the grains are coated with the wetting fluid surface films at the micron scale. Fig. 3.1 demonstrates the relation between various mesh components.

3.2.1 Chemical reactions

As mentioned earlier, we model the interaction between the fluid and the solid grains by introducing the non-linear adsorption of the solute. The adsorption is incorporated by Godunov operator splitting method as an equilibrating stage that follows every transport time step, which is a direct extension of how the inert transport calculations are implemented. Namely, we start with the advection-diffusion-reaction equation (we omit the optional dependency (\mathbf{x}, t) of various parameters on the spatial and temporal coordinates for the sake of brevity)

$$\frac{\partial C}{\partial t} = \nabla \cdot (D_m \nabla C) - \nabla \cdot (\mathbf{u}C) + \left(\frac{\partial C}{\partial t} \right)_{\text{reaction}}, \quad (3.2)$$

subject to the boundary conditions (2.24). The effect of the first two terms on the right-hand side of Eq. 3.2 is calculated with exactly the same procedure as described in Section 2.2.5. The third term denotes a generic reaction term whose exact form depends on the reactions considered in the model. For the non-linear adsorption, it assumes the form

$$\left(\frac{\partial C}{\partial t} \right)_{\text{reaction}} = k_1 \Gamma - k_2 C \cdot (\Gamma_{\text{max}} - \Gamma). \quad (3.3)$$

Here $\Gamma_{\text{max}}/\Gamma$ is a (maximum) surface concentration [moles/m²], and $k_{1,2}$ are the desorption/adsorption rates, with the units of [m²/(l·s)] and [m²/(mol·s)]. Since Eq. 3.3 contains no gradients, it only needs to be integrated in time. Moreover, if the equilibrium assumption is considered, then we only need to obtain the steady-state solution of Eq. 3.3 by equating its left-hand side to zero. In addition to this, we have

to enforce the mass conservation law between the volumetric and the surface concentrations of the solute. Hence we arrive at the following system of equations that has to be solved at every node located on the grain surface

$$\begin{cases} \Gamma = \Gamma_{\max} \frac{\beta C}{1 + \beta C}, \\ C_0 V_i + \Gamma_0 S_i = C V_i + \Gamma S_i. \end{cases} \quad (3.4)$$

Here the first equation is a Langmuir adsorption isotherm and the second one is a mass conservation law, where the “0” subscript denotes initial concentration levels. Langmuir isotherm is derived under assumption that the adsorption sites do not influence each other and as such it does not account for the overall charge of the adsorbing surface. This system is solved after every transport time step because it disturbs the fluid-solid equilibrium. The following notations are used

$\beta = k_2/k_1$ equilibrium constant for adsorption, [l/mol]

S_i area of an i^{th} boundary node, [m²]

V_i volume of an i^{th} boundary node, [m³]

An algorithm for calculating the nodal volume and surface values is demonstrated in Fig. 3.1: it consists of summing up the volumetric contributions of the adjacent FV segments, marked with index k , of the highest (3D or 2D) and the second highest (2D or 1D) dimensions of a given model,

$$V_i = \sum_k V_k, \quad S_i = \sum_k S_k. \quad (3.5)$$

As noted before, more complex chemical reactions, such as mixing of multiple species within the fluid or mineral precipitation, can be modeled using the same approach by replacing the solution of Eq. (3.4) with a specific chemical solver. A particular example of such a solver is PHREEQC (Charlton and Parkhurst, 2011). It is a geochemical software capable of simulating a wide range of equilibrium reactions between water and minerals, ion exchangers, surface complexes, solid solutions, and gases. It contains an internal scripting language, which allows for a general formulation of kinetic reactions such as nonequilibrium mineral dissolution and precipitation. PHREEQC’s functionality as a chemical solver will be covered in more detail in the next chapter. For this section it is important to note that PHREEQC can be run not only as a stand-alone software but also as a C++ class (called IPhreeqc) from any in-house

fluid flow and transport code. An input method of IPhreeqc expects local concentrations, a time step (for kinetic reactions), a nodal area (for surface reactions) and a mass of water (linearly proportional to a nodal volume) as its arguments. An output method can return new concentrations values thus concluding the calculations for a single time step.

3.2.2 *Distance field calculation*

The described reactive transport model can be used to address questions associated with the chemically enhanced oil recovery in porous media, for instance low-salinity water flooding (Lager et al., 2008). To do this, we have to introduce the concept of a second immiscible phase. Since our 3D meshes consist of millions of elements, methods that are usually used to extend the Navier-Stokes equation to the case of multiple phases (level-set, volume-of-fluid, phase field methods, see, for instance, Unverdi and Tryggvason (1992)) would require a prohibitive amount of computations. To avoid them, we propose the use of a simple quasi-static rule-based approach.

We assume that for a non-wetting fluid (e.g. water in an oil-wet rock) to invade any given pore, i.e. a drainage process, it has to overcome the capillary pressure exerted on a spherical bubble inscribed inside that pore. In other words, we approximate an interface between two fluid phases as having a spherical shape. The capillary pressure is related to the curvature radii R_1 and R_2 of an interface through the Young-Laplace equation (Collins and Cooke, 1959)

$$P_c = \sigma(1/R_1 + 1/R_2). \quad (3.6)$$

In case of a spherical interface two radii are equal ($R_1 = R_2 = R$) and the capillary pressure is inversely proportional to the sphere radius R . The effect of a non-zero wetting angle θ_w can in principle be included with a $\cos \theta_w$ term, resulting in a local capillary pressure of $P_c = 2\sigma \cos \theta_w / R$.

It should also be noted that, since we are working with the irregular pore geometries with no distinct pore entities (as opposed to, for instance, pore networks), we define radii for every point of a pore domain. A point radius is a radius of a sphere of a maximum size that is inscribed in the pore space and covers that particular point. This remark on the maximum

size of a sphere is important because a point can be covered by more than one inscribed sphere.

Assuming for the moment the radius of every point is known, the procedure for modelling the invasion process is the following. First, a radius value for every point belonging to the sample inlet (which currently is an oil-water interface) is analysed. Starting from zero, an entry pressure is increased in small increments until it exceeds the $P_c = 2\sigma/R_{\max}$, where R_{\max} is a maximum radius among all the inlet points. Then all the points with the radius $R > R_{\max}$ that are connected to the initial entry point with $R = R_{\max}$ become invaded. The condition $R > R_{\max}$ can hold because it is checked for all points that are connected through the defending wetting fluid to the entry point, while the R_{\max} value was determined only among the points that belong to the inlet surface. Moreover, the points can become invaded only if they are additionally connected to the outlet through the wetting phase, i.e. there is a path for the defending fluid to escape the pore sample. Once all locations for invasion are identified, the procedure is repeated again but this time it starts not only with the (non-invaded) points that belong to the inlet but also with the points that belong to the newly formed oil-water interface.

Therefore, the full invasion-percolation scenario is simulated during this procedure. This procedure can also be applied to an imbibition process, e.g. water flooding of a water-wet system initially filled with oil, by considering increasing radii of spheres of the defending non-wetting fluid. However, this approach, as implemented in this thesis, only accounts for the bulk fluid connectivity and not for the connectivity through the surface films, i.e. no film flow is assumed. Also, only piston-like fluid displacement is simulated and snap-off effects are not considered. The described algorithm is similar to the one presented by Silin and Patzek (2006) but it is extended to work on unstructured meshes.

This procedure is of an approximate character for several reasons. First, the interface between two fluids does not necessarily assume a spherical shape. Second, the quasi-static approach is only valid when capillary forces dominate viscous forces, i.e. only for slow flow rates that are usually characterized by capillary numbers $N_{Ca} = \frac{\mu v}{\sigma}$ (Lake, 1989) of less than 10^{-4} (μ is viscosity of the wetting fluid, v is characteristic velocity, σ is interfacial tension). The approach is strictly valid only for the strongly wetting case, for example the fully oil-wet system. Finally, as indicated above, certain physical effects intrinsic to fluid displacement are

not accounted for. Nevertheless, this approach should properly predict the order in which pores are invaded and also demonstrate the change in residual oil in case interfacial tension is locally reduced.

The pore radii for an irregular pore geometry are calculated by first computing the pore space distance field, i.e. the distance to the nearest boundary for every node in the mesh. There are different ways of calculating the distance field, but most of them are geometrical algorithms that can only be applied to regular finite difference meshes (Sethian, 1999). In order to find the distance field of an arbitrary unstructured mesh, such as the one shown on Fig. 2.8, one has to solve a PDE to which the distance field would be a solution. There are two potential candidates for this task. One is the Poisson equation which gives an approximate result but presents no complications for finding its numerical solution (Fares and Schröder, 2002). An alternative is called the Eikonal equation which defines the exact distance field but is strongly non-linear and requires special numerical treatment (Tucker et al., 2005). Here we will consider both solutions.

The first approach is based on the following assumption. If a particle is placed at an inner node of the computational domain and allowed to perform a random walk until it hits the domain boundary then the average time it takes for this particle to reach the boundary should be proportional to the distance from the particle's initial position to this boundary. Mathematically, this average time \mathcal{T} can be computed by solving the following Poisson equation

$$\begin{cases} \nabla^2 \mathcal{T} = -1, & \mathbf{x} \in \Omega; \\ \mathcal{T} = 0, & \mathbf{x} \in \partial\Omega_{\text{Dir}}; \\ \frac{\partial \mathcal{T}}{\partial \mathbf{n}} = 0, & \mathbf{x} \in \partial\Omega_{\text{Neu}}. \end{cases} \quad (3.7)$$

where Ω denotes the computational domain. The Dirichlet conditions (Dir) are prescribed on the walls where the distance is calculated from, Neumann conditions (Neu) are assigned otherwise. The random walk model is expressed in this equation as a diffusion process with the unit diffusivity constant. Once the equation is solved the distance field $d(\mathbf{x})$ (with the units if [m]) is computed as

$$d(\mathbf{x}) = \sqrt{\nabla \mathcal{T}(\mathbf{x}) \cdot \nabla \mathcal{T}(\mathbf{x}) + 2\mathcal{T}(\mathbf{x})} - |\nabla \mathcal{T}(\mathbf{x})|. \quad (3.8)$$

This relation is exact only when the boundary is flat and forms no angular features. Otherwise some deviations will occur. Fig. 3.2 demonstrates an application of this procedure in 2D. The domain used is a 6×6 square, hence the maximum distance value is reached at its centre and equals 3. The Poisson equation is obtained with a first-order FE method on a triangular mesh, similar to how the diffusion equation was solved in Eq. 2.26. Nodal gradients of ϕ are estimated by first calculating the piecewise constant element gradients and then extrapolating those values, weighed by the element area, back onto the nodes. For a triangular FE grid the weighting factor is $1/3$. In the first numerical case, Dirichlet conditions are imposed on the upper and lower boundaries, with Neumann conditions on the left and right sides, i.e. the angle between different portions of the Dirichlet boundary is still zero. In the second case distance field from all 4 sides of the square is calculated, forming four right angles in a Dirichlet boundary. Fig. 3.3 shows the distance field values plotted along the vertical axis of symmetry of the square. As expected, as long as the Dirichlet conditions are prescribed on flat boundaries, the Poisson equation yields the correct answer (Fig. 3.3a). When the boundary includes angular features (Fig. 3.3b) this approach is valid only in its vicinity. The reason for this is that the $d(\mathbf{x})$ value becomes influenced by more than one linear segment of the domain boundary, which is a consequence of the ellipticity of the Poisson equation. Depending on the application in mind, this might be sufficient. However, we require the distance field to be true everywhere.

A straightforward remedy for such a problem would be to replace the diffusion process with the wave propagation. Indeed, if one sends a spherical wave from a given point and calculates the time it takes for it to reach the boundary, the result would be determined solely by the closest distance to the boundary, no matter what spatial configuration that boundary assumes. As in the previous case, the point-wise wave propagation time can be determined by solving a certain PDE called the Eikonal equation. The Eikonal solution is an exact domain distance field $d(\mathbf{x})$, and the equation is written as

$$\begin{cases} |\nabla d(\mathbf{x})| = 1, & \mathbf{x} \in \Omega; \\ d = 0, & \mathbf{x} \in \partial\Omega_{\text{Dir}}; \\ \frac{\partial d}{\partial \mathbf{n}} = 0, & \mathbf{x} \in \partial\Omega_{\text{Neu}}. \end{cases} \quad (3.9)$$

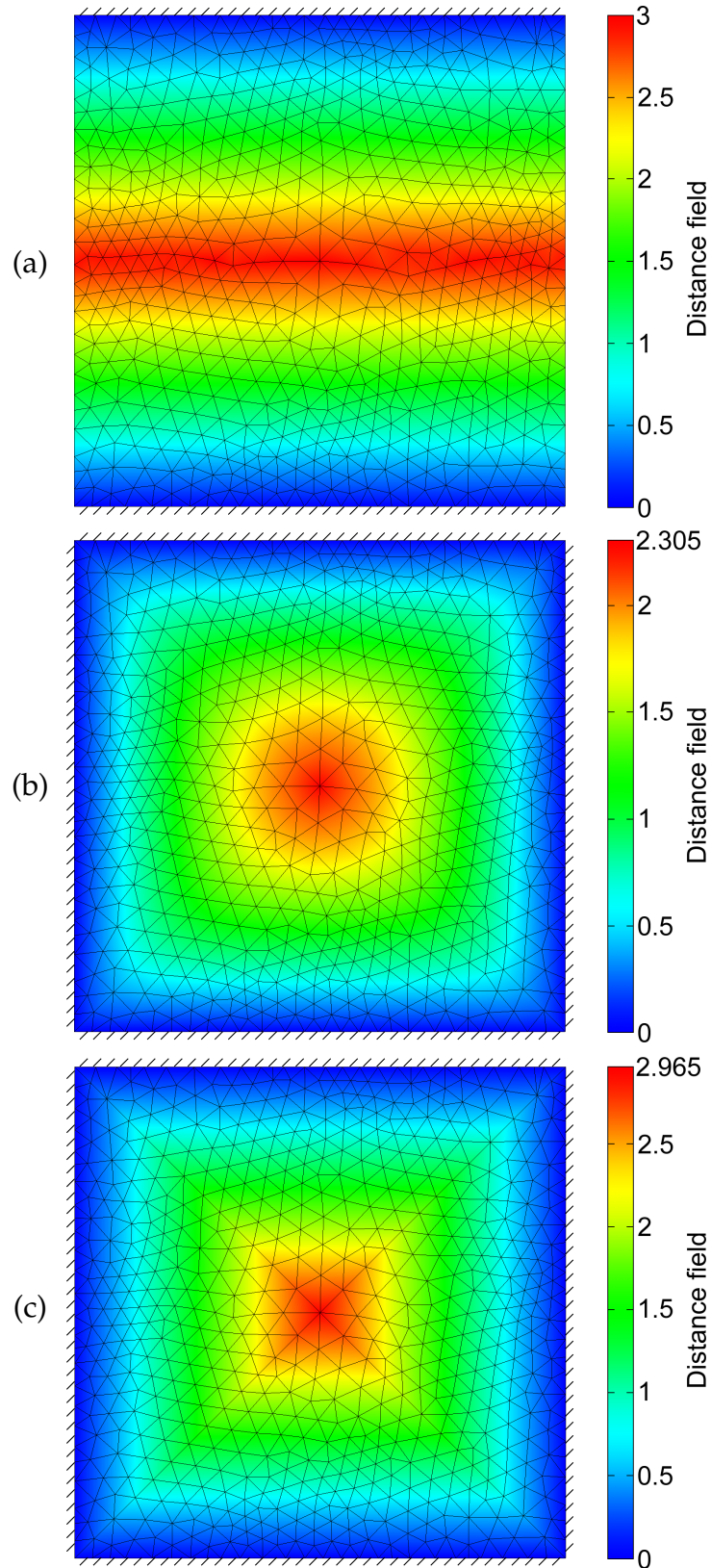


Figure 3.2: Distance field computed as a solution of various numerical cases: (a) Poisson equation with Dirichlet boundary conditions prescribed on the top and bottom sides of the domain. (b) Poisson equation with Dirichlet conditions prescribed on all four sides. (c) Eikonal equation with Dirichlet conditions prescribed on all four sides. Diagonal strokes mark Dirichlet boundaries.

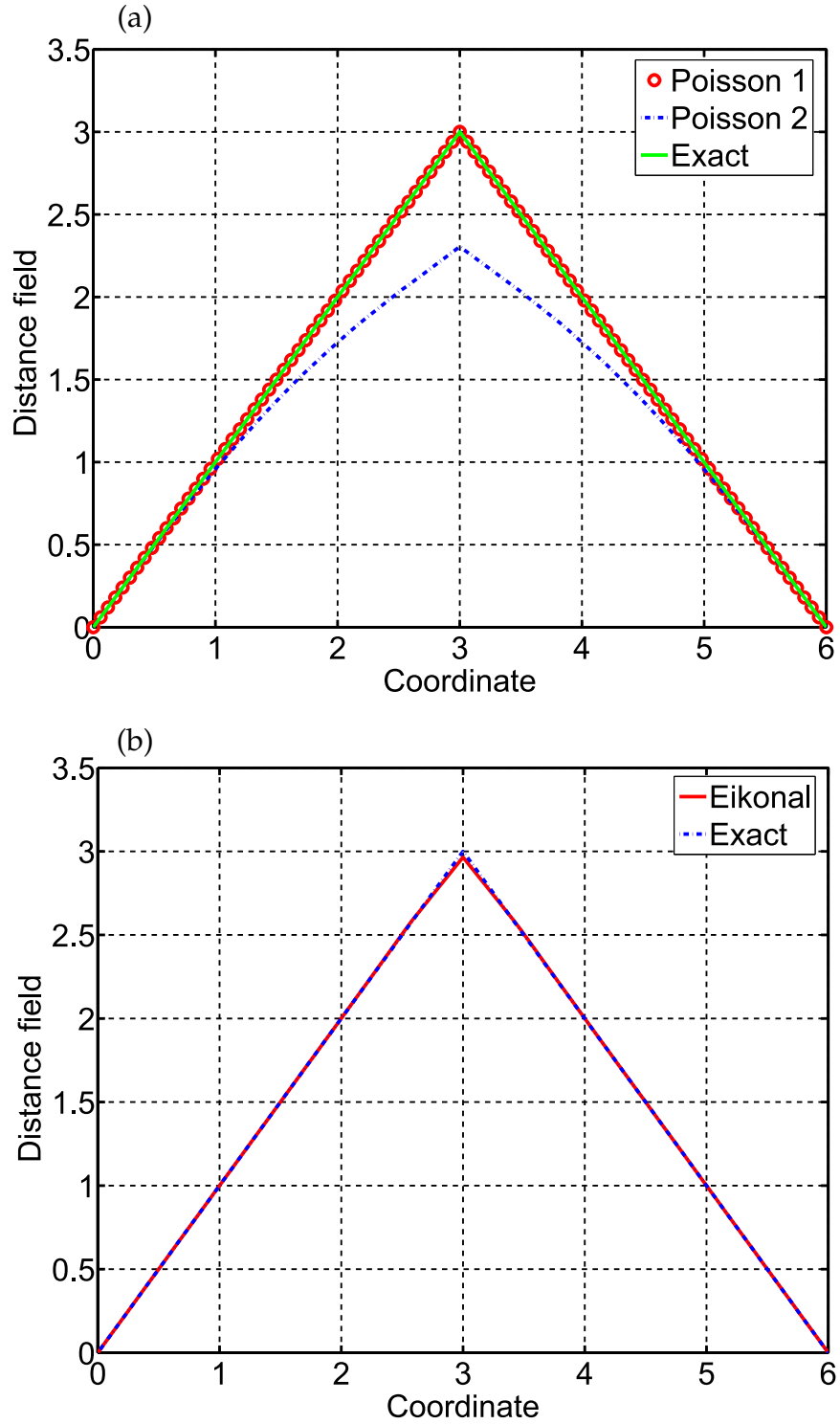


Figure 3.3: Distance field plotted along the vertical axis of symmetry of the domain from Fig. 3.2. The Poisson equation yields correct distance field as long as Dirichlet boundary has no angular features. Otherwise the numerical solution deviates from the analytical one away from the boundary, as the distance field becomes affected by more than one Dirichlet segment. Eikonal solution is exact everywhere except for a slight deviation at the domain centre where a shock-like feature is formed.

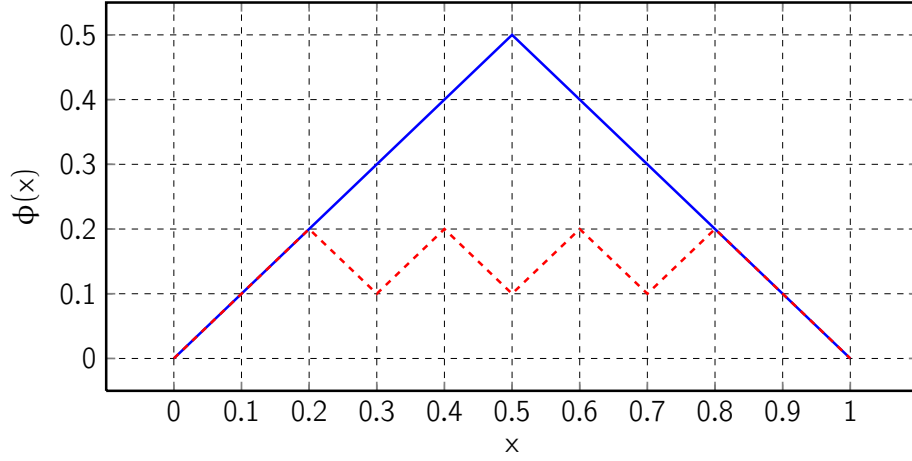


Figure 3.4: Solutions of Eikonal equation on a 1D domain $\Omega = [0; 1]$. The solid line corresponds to the true distance field, while the dashed line describes the sawtooth-like shape of any alternative solution of Eq. 3.9.

The boundary conditions for this equation are the same as in the previous case. It can be easily seen that the solution of this equation is not unique, due to an absolute value operator. As an illustration of this, Fig. 3.4 demonstrates two different solutions of the Eikonal equation on a 1D domain $\Omega = [0; 1]$. It is important to follow a procedure that will allow us to obtain the true distance field solution. A fundamental requirement that the sought-for solution has to satisfy is that its derivative can change sign only at the inner regions that send waves touching two or more boundary points at the same time. Otherwise this solution should linearly increase from boundaries towards the domain central points. One can think of it as a transient process where solution is propagated from the boundaries towards the inner parts of the domain. This deduction will serve as a basis of a mathematical procedure that we employ for solving the Eikonal equation. It is similar to the one described by Xia and Tucker (2010). As a first step, we define the following pseudo-velocity vector

$$\mathbf{U} = \min_{\|\cdot\|} \left\{ \nabla d, \frac{\nabla d}{\|\nabla d\|} \right\}. \quad (3.10)$$

We then multiply the first equation from (3.9) by itself and add a pseudo-time τ derivative on its left-hand side. Combining both steps, we arrive at the following system of partial differential equations

$$\begin{cases} \mathbf{U} = \min_{\|\cdot\|} \left\{ \nabla d, \frac{\nabla d}{\|\nabla d\|} \right\}, \\ \frac{\partial d}{\partial \tau} + \mathbf{U} \cdot \nabla d = 1 \iff \frac{\partial d}{\partial \tau} + \nabla(\mathbf{U}d) = 1 + d\nabla\mathbf{U}. \end{cases} \quad (3.11)$$

The second part here is akin to an advection-diffusion equation, for which we have to calculate its steady state solution. The reason for choosing the pseudo-velocity as defined in (3.10) is to not let the information about the distance propagate faster than in the steady-state case. If one starts from fixed zero values at the boundary and zero initial values inside the domain, then, due to the source term in (3.11), the solution inside will gradually increase until it converges to a correct steady-state value. However, unlike Eq. (2.23), in this case numerical experiments show that we cannot decouple “advection” and “diffusion” parts and the whole system has to be solved using the FV method. The corresponding discrete FV formulation of this system with explicit time discretization is

$$\begin{cases} \mathbf{U}^\tau = \nabla d_e^\tau, \\ d_i^{\tau+\Delta\tau} = d_i^\tau - \Delta\tau \left(\frac{1}{V_i} \sum_j (\mathbf{n}_j \cdot \mathbf{U}_j^\tau) (d_j^\tau - d_i^\tau) A_j - 1 \right). \end{cases} \quad (3.12)$$

Here the gradient of the distance field is re-calculated every time step in an element-wise constant fashion using the gradients of the finite-element basis functions, thus updating the pseudo-velocity field. When inserted into the second equation of (3.12), velocity values are clipped to a length of less or equal than unity to improve the method’s stability. Additionally, a simple first order upwinding scheme is not sufficient to calculate the distance values at the finite-volume segments. Instead, time marching of Eqs. (3.12) in τ was found to converge when the following scheme was used

$$d_j^\tau = d_{\text{upw}}^\tau + \nabla d_{\text{upw}}^\tau \cdot (\mathbf{x}_j - \mathbf{x}_{\text{upw}}), \quad (3.13)$$

Algorithm 3.1: Conversion of distance field into inscribed radii field

```

DATA: Distance field  $d(\mathbf{x})$  – nodal variable
RESULT: Radii field  $R(\mathbf{x})$  – elementwise constant variable

FOREACH node  $i$  DO
     $\Omega \leftarrow \emptyset$  // empty list of elements
     $\mathbf{x}_i \leftarrow$  coordinate of  $i$ 
     $D_{\text{val}} \leftarrow d_i(\mathbf{x})$ 
    FOREACH parent element  $j$  of  $i$  DO
         $\mathbf{x}_j \leftarrow$  barycentre of  $j$ 
        IF  $\|\mathbf{x}_i - \mathbf{x}_j\| \leq D_{\text{val}}$  THEN
            append  $j$  to  $\Omega$ 
        END
    END
    FOREACH element  $p \in \Omega$  DO
        FOREACH neighbour  $q$  of  $p$  DO
             $\mathbf{x}_q \leftarrow$  barycentre of  $q$ 
            IF  $\|\mathbf{x}_i - \mathbf{x}_q\| \leq D_{\text{val}}$  AND  $q \notin \Omega$  THEN
                append  $q$  to  $\Omega$ 
            END
        END
    END
    FOREACH element  $p \in \Omega$  DO
         $R_p(\mathbf{x}) \leftarrow D_{\text{val}}$ 
    END
END
  
```

with the nodal gradients extrapolated from the surrounding element gradients using a distance to an element's barycentre as a weight

$$\nabla d_i = \frac{\sum_e \nabla d_e / |\mathbf{x}_i - \mathbf{x}_e|}{\sum_e 1 / |\mathbf{x}_i - \mathbf{x}_e|}. \quad (3.14)$$

Here the subscript upw denotes an upwind node and \mathbf{x} is used to refer to a radius vector. A radius vector of a FV segment is taken equal to a radius vector of its barycentre.

Fig. 3.2c demonstrates the improvement of a solution obtained by Eikonal equation compared to the one obtained by the Poisson equation. The resulting distance field is almost exact. Fig. 3.3 reveals that the only slight deviation (1.1%) occurs at the domain centre which is the only point influenced by all four boundary segments. A shock-like feature occurs here and it can be correctly resolved by either locally refining the mesh

or using higher-order numerical schemes. Incidentally, this shock-like feature is a part of the medial axis of our square domain. A medial axis of a domain is a closure of a set of centres of all spheres (or circles in 2D) that touch the domain boundary at not less than two points. Fig. 3.3 indicates that the medial axis is characterized by a negative jump of the first derivative of $d(\mathbf{x})$, which in turn means that its second derivative, or more precisely its Laplacian, equals minus infinity, $\nabla^2 d(\mathbf{x}) = -\infty$. This offers an alternative way of determining the medial axis position as compared to purely geometrical methods.

Once the time marching has converged to a steady state, the resulting distance field can be easily converted into the radii field. The radius for a given point is taken to be the maximum distance value among all the points located within the distance value of a current point. Within the finite element framework, this procedure can be described with the pseudocode in Algorithm 3.1.

As mentioned above, the separate treatment of the grain boundaries in our numerical approach allows us to simulate the solute transport along the surface films that coat the grains. Physically these films are formed due to the roughness of the grain surfaces that is not captured by the resolution level at which the porous geometry has been digitized. On the other hand, for the acute geometry features that are larger than the sample resolution (i.e. the voxel size) the formation of the wetting fluid films is an emergent property because the acute features are characterized by small radii values and hence the high capillary pressure level is required to remove the wetting fluid from them. We call these regions of the immobile wetting fluid the “bulk layers” to distinguish them from the sub-resolution surface films.

Finally, Fig. 3.5 demonstrates the distance field and the corresponding radii field for a triangular 2D mesh obtained from a grainstone microphotograph (see Fig. 2.12). Fig. 3.6 shows a corresponding snapshot of a phase distribution at a particular level of the entry pressure during an invasion-percolation scenario, where a non-wetting fluid enters the domain at the left side. It also shows the above-mentioned bulk wetting layers in the concave features of the grains.

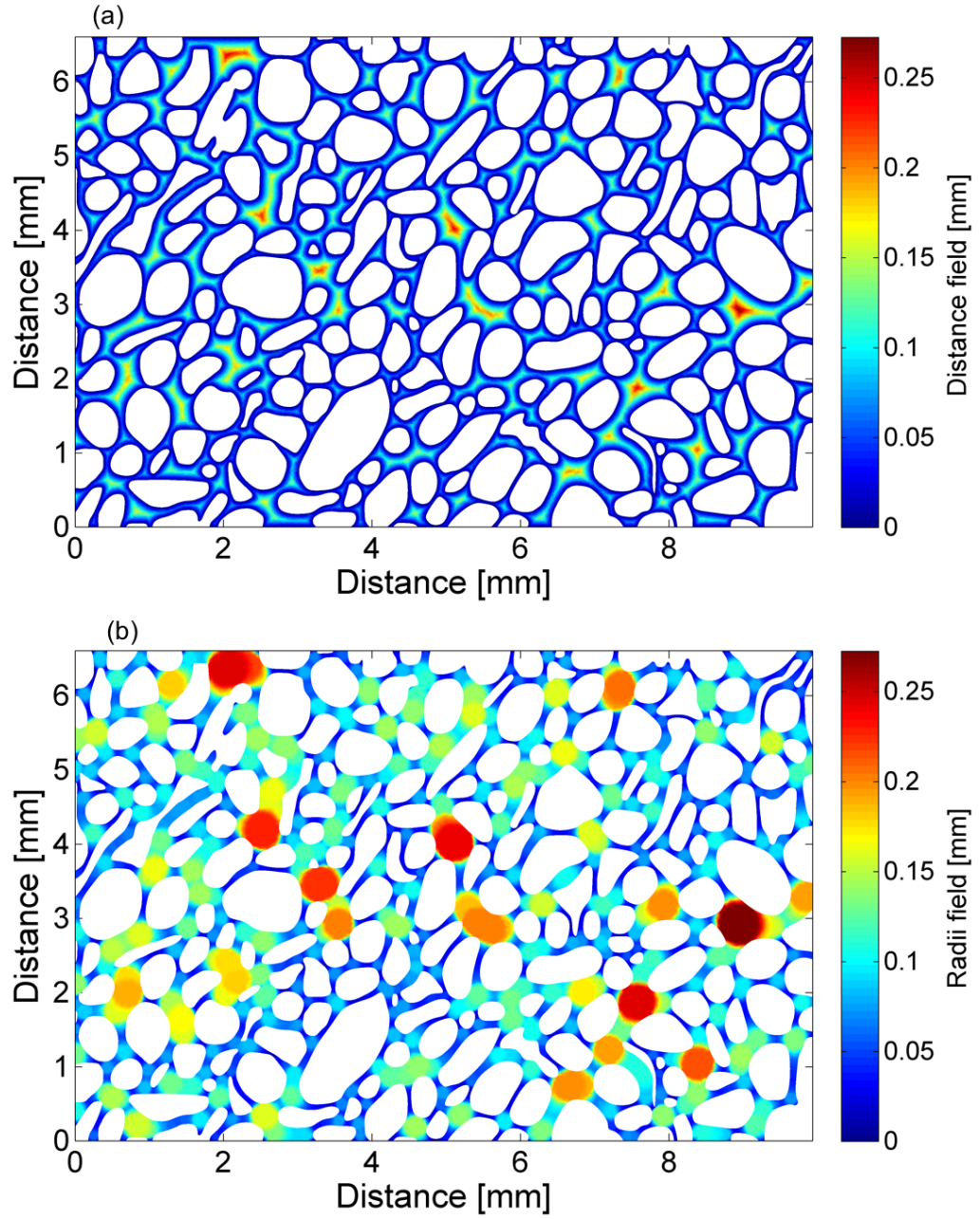


Figure 3.5: (a) Distance field to the nearest pore wall for a 2D grainstone thin section (see also Fig. 2.12). (b) The corresponding radii field.

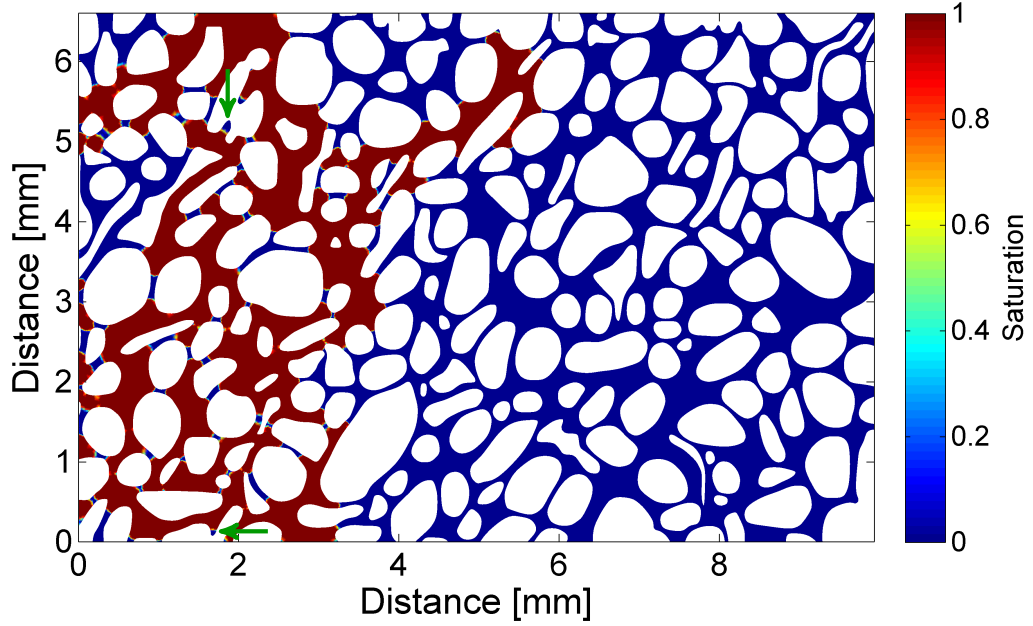


Figure 3.6: Snapshot of a 2D phase distribution at a particular level of the entry pressure during an invasion-percolation scenario. Dark red colour represents the invading non-wetting fluid and blue colour marks the initial wetting fluid. Green arrows show examples of the bulk wetting layers that cannot be removed because they lost connectivity to the outlet.

3.3 EXAMPLE APPLICATION

The ultimate application that we have in mind for our pore-scale model is simulating the reactions that govern wettability change in carbonate rocks. As described in Chapter 1, it is thought that the wettability alteration reactions involve solute adsorption onto the rock surface adjacent to oil, as well as possible change in pore geometry due to dissolution. Therefore, in this chapter we present a model of the transport of a generic solute with affinity towards the rock surface in a pore space partially occupied by oil. Specific chemical reactions will be considered in the next chapter.

To demonstrate the application of our numerical methods we used the Fontainebleau sandstone sample presented in the previous chapter, converted into a finite element tetrahedral mesh. Initial modelling steps are the same as in the inert transport case described in the previous chapter: calculating FE Stokes solution using domain decomposition and AMG method for an ensuing linear system. The computed velocity profile was supplied to an advection-diffusion equation and the evolution of the solute concentration was calculated. Fig. 3.7a depicts an example of the spatial distribution of a solute within the porous sample at a certain

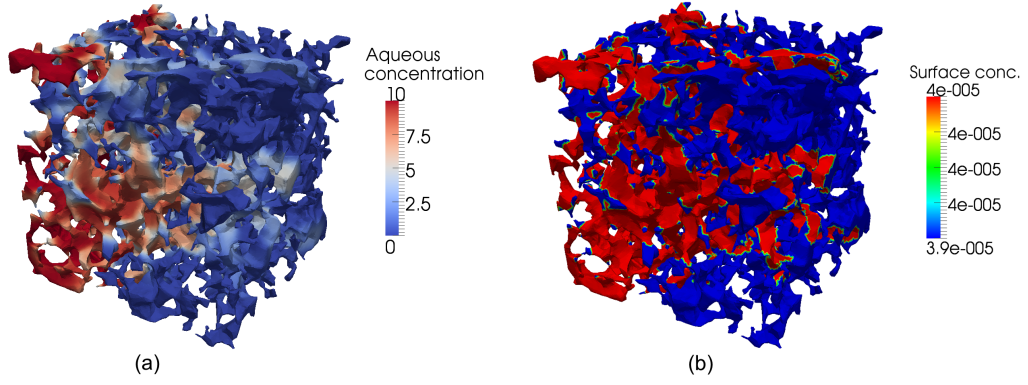


Figure 3.7: (a) Snapshot of the spatial distribution of the solute concentration within the pore space. The prescribed concentration at the inlet is chosen as 10 for convenience and does not represent a physical volumetric concentration level. (b) The corresponding surface concentration when adsorption is present. The red color denotes levels exceeding half of the maximum allowed surface concentration. A narrow range of the colorbar is chosen to clearly distinguish between the values above and below this threshold (of $4 \cdot 10^{-5}$).

moment in time. The case of inert solute transport was then compared to a situation when adsorption was present. Fig. 3.7b shows the spatial distribution of the adsorbed solute within the 3D sample. The surface is marked with a different color when the concentration level exceeds half of the maximum allowed surface concentration; this makes it easier to estimate the extent of the affected surface. One can see that the solute is preferably adsorbed along the major flow pathways, dominated by advection (closer to the outlet), and then propagates towards the more stagnant pores due to diffusion (closer to the inlet).

It is well-known that adsorption mechanism results in the breakthrough curves being retarded as compared to the transport of an inert solute (Pope, 1978). Fig. 3.8a shows the comparison between these two cases and it can be seen that same concentration levels appear later when adsorption is present. Since we associate an areal value with every boundary node of our finite element mesh, we can accurately measure the evolution of the surface affected by our chemical agent. For instance, if we assume that local wettability changes occur after a certain surface concentration threshold has been reached, we can measure the percentage of surface where these changes have developed. Fig. 3.8b shows such a plot with five different threshold values α that are represented as a portion of the maximum surface concentration Γ_{\max} . The first four curves correspond to regions of the Langmuir isotherm where the slope is steep and therefore a solute is more readily transferred from the fluid to the rock surface.

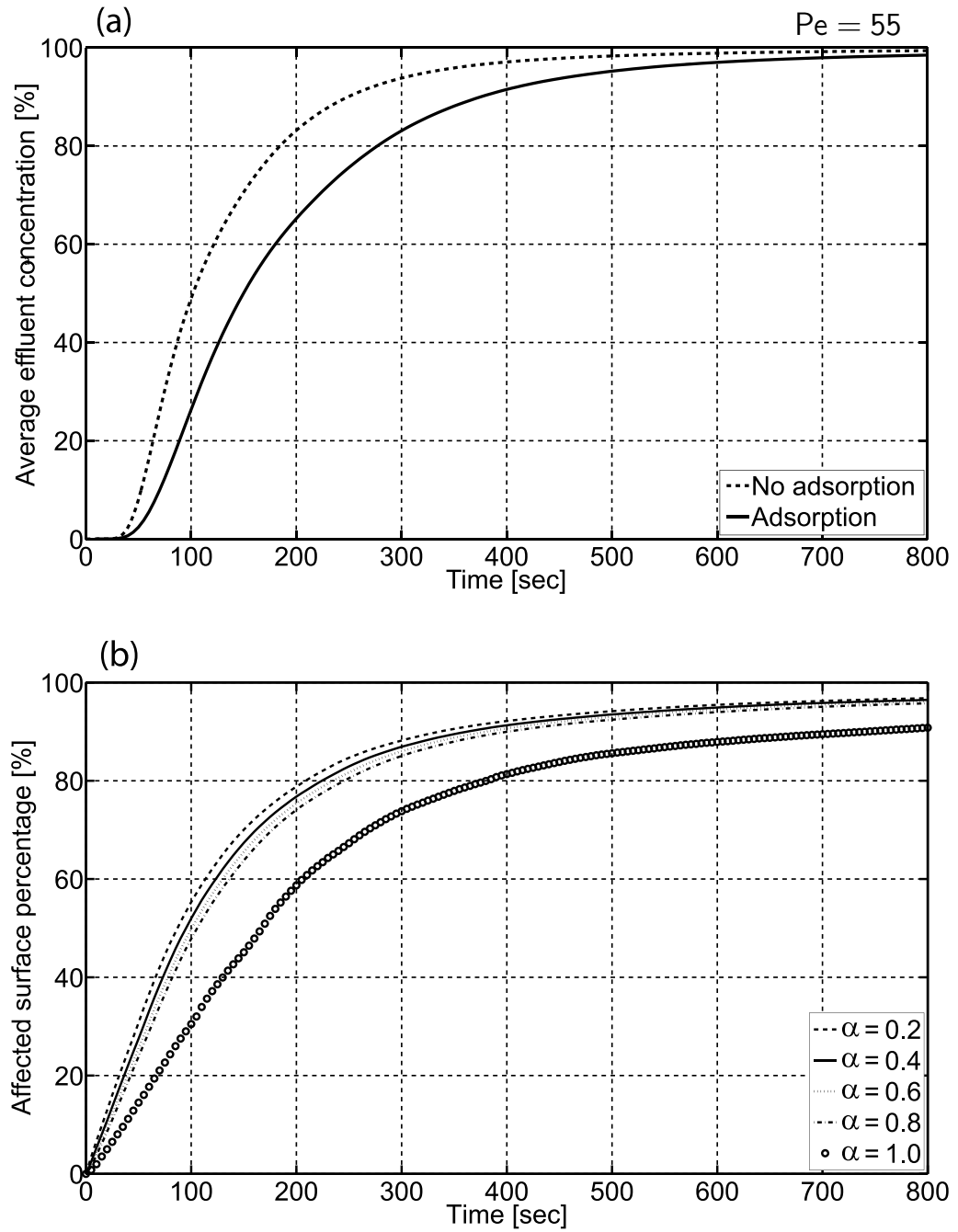


Figure 3.8: (a) Flux-weighted breakthrough curves for cases with and without adsorption. Presence of adsorption introduces the retardation of an outflow solute concentration. (b) Evolution of surface covered with concentration values exceeding certain percentage α of the maximum allowed value Γ_{max} and plotted as a percentage of the overall grain surface.

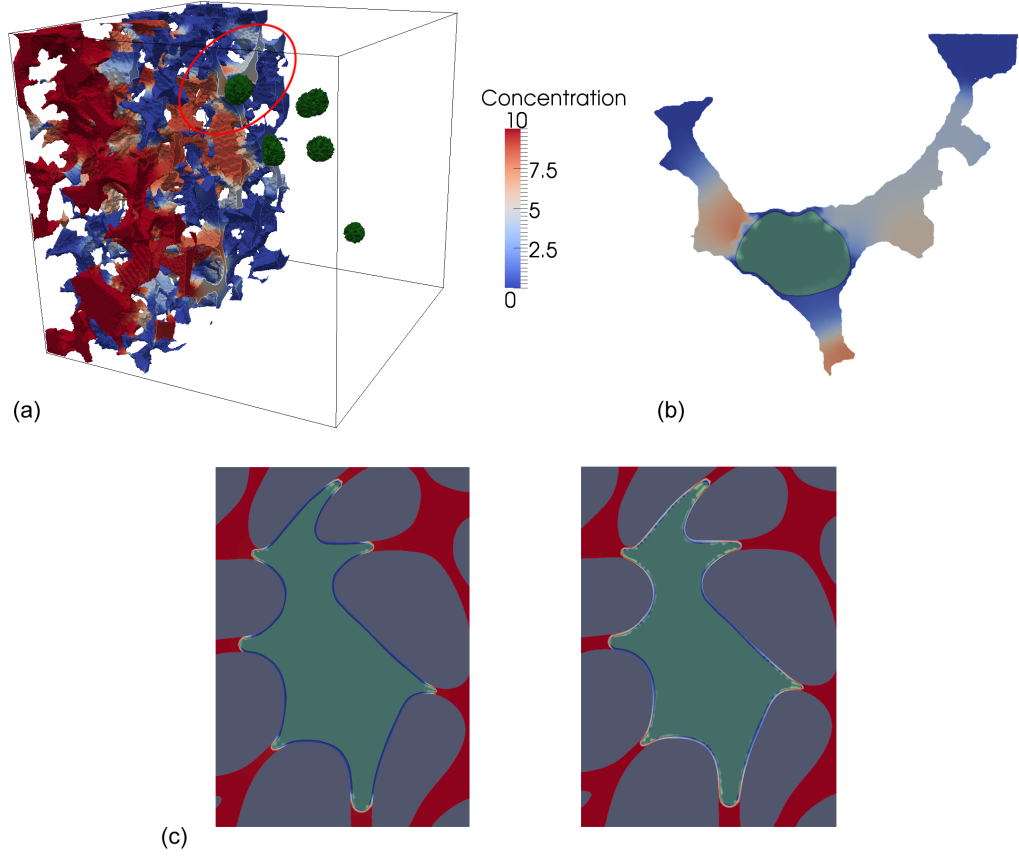


Figure 3.9: (a) A distribution of the solute concentration together with the oil blobs (shown in dark green). The domain is clipped in a way to show an area surrounding one of the blobs. (b) Close-up of a region denoted by red circle on fig. 3.9a. The green zone represents the oil blob cross section. Note that despite the presence of the sub-resolution surface films, the grain surface area surrounding the blob has negligible concentration levels. (c) Auxiliary 2D images of a solute distribution near a pore occupied by oil, also depicted in green. On the left image the solute adsorption is high and the solute cannot propagate towards the centre of the pore. On the right picture the adsorption is low and hence the solute can diffuse along the grain surface.

Since the slope of the adsorption isotherm is almost constant for these four curves, the gap between them is small and does not increase with α . As Γ approaches the maximum value, a surface becomes saturated with a solute and more time is required to further increase the surface concentration (the slope of the adsorption isotherm approaches zero). Hence the curve corresponding to $\alpha = 1$ assumes a slightly distant position.

Finally, we show how our reactive transport model can be used to estimate the potential of the enhanced oil recovery procedures. To do so, we first calculate the capillary pressure distribution based on the distance map. Here we consider the scenario in which the water-wet rock has already been flooded with water and retains the residual oil in the form

of the trapped blobs, i.e. no invasion-percolation scenario is simulated. We assume that these blobs would occupy the medium to large pores since they are characterized by the lowest capillary pressure values. We can determine the location of the largest pores by calculating the distance field of the 3D pore space. In our particular case, the largest pores have a linear size of 80 μm and we placed the trapped oil inside the pores larger than 50 μm . However, it is known that in reality the configuration of the oil blobs is a non-trivial function of the wettability and saturation history (Landry et al., 2011) and can span several pores. Nevertheless, our simplified approach can, to a first approximation, measure the effect that the presence of oil blobs has on the breakthrough curves and adsorption. We restricted our velocity and transport calculation to the remaining pore space, including the surface elements surrounding the oil, to which a thickness of 0.1 μm has been assigned. If the solute concentration level at the grain surface adjacent to the trapped oil reaches a certain level, this could result in a local wettability change and the release of that oil droplet.

Similar approach can be applied to the oil-wet scenario. In this case the oil blobs will occupy smaller pores. As described by Hammond and Unsal (2009), in order for a surface-active agent to access the rock surface of an oil-wet rock, it has to diffuse towards the rock surface, adsorb near the water-oil-rock contact and diffuse along the surface behind the oil meniscus. These processes can be readily simulated using our pore-scale model.

Fig. 3.9a shows a clipped distribution of the solute concentration, which surrounds an oil blob, while Fig. 3.9b shows a close-up of a pore occupied by the trapped oil. Due to the diffusion process, the solute can propagate towards the centre of the blob along surface films. The extent of this propagation is determined by the grain surface reactivity, expressed by Γ_{max} parameter of the adsorption isotherm, and by the thickness of surface films. In this example the solute propagation stopped at the oil boundary because the Γ_{max} is too high for the solute to move any further. this effect is further elucidated in Fig. 3.9c, that shows two auxiliary 2D images of a solute distribution near a pore occupied by oil. On the left image the solute adsorption is high and the solute cannot propagate towards the centre of the pore. On the right picture the adsorption is low and hence the solute can diffuse along the surface films. This implies that if the chemical species is too easily adsorbed to the rock surface

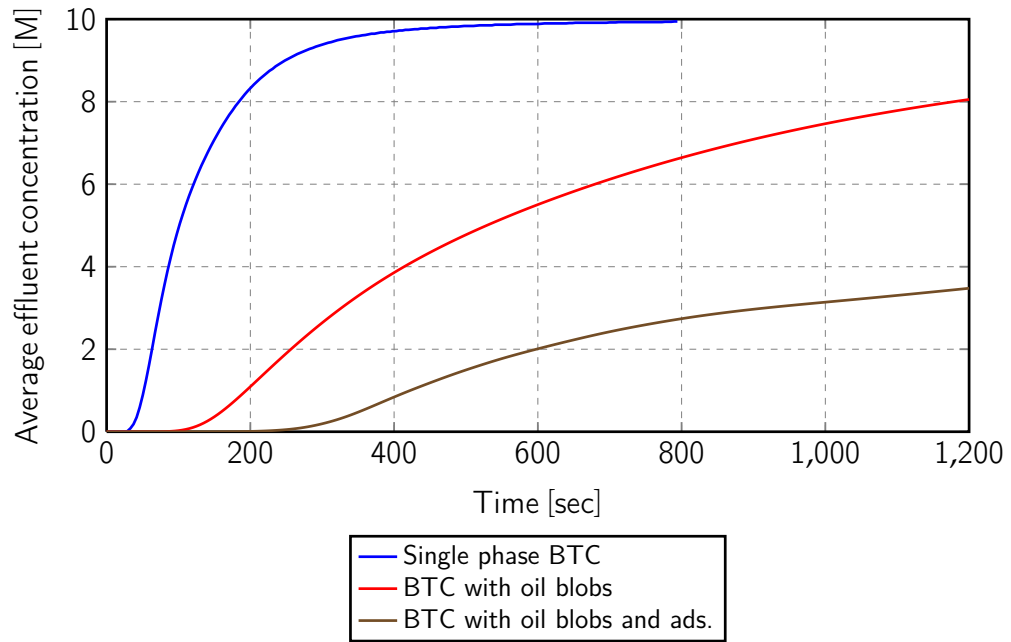


Figure 3.10: Flux-weighted breakthrough curves for the transport cases with (red) and without (blue) the presence of oil, and with both oil blobs and sorbing grain surfaces (brown). Oil residing in the largest pores leads to a very long tailing of the effluent solute concentration. Comparing this figure with Fig. 3.8a reveals that the presence of oil blobs results in a stronger solute retardation due to adsorption.

during the EOR procedure, it will not be able to facilitate the release of trapped oil. It is therefore important to consider the time scales associated with different chemical reactions as well as advection and diffusion. This importance will be further emphasized in the next chapter of the thesis.

Fig. 3.10 presents a comparison between three breakthrough curves – that of an inert solute, of an inert solute when the oil is present and of an adsorbing solute when the oil is present. It can be clearly seen that the effective dispersivity of the sample is significantly increased when the largest pores are inaccessible for the solute and therefore it is transported along the otherwise less preferable flow pathways. This results in a pronounced tailing of the breakthrough curve, or in other words the flow Peclet number is significantly increased. It is also interesting to compare Fig. 3.10 and Fig. 3.8a. It can be seen that the presence of oil in the largest pores results in a stronger solute retardation due to adsorption as compared to the case with unoccluded pores.

3.4 SUMMARY

In this chapter we presented a computational method for the direct pore-scale simulation of the reactive solute transport. The method uses the FE technique to calculate the fluid velocity field and the combined FE-FV method to compute the solute concentration profile. Using the grid-based methods allows us to preserve the accurate information of the pore space structure, which can be crucial for modelling the fluid-rock chemical interactions. Chemical reactions are decoupled from the transport calculations which allows us to link any stand-alone chemical solver to our simulator.

We applied the procedure to a reconstructed Fontainebleau sandstone sample and showed the retardation behavior of the averaged breakthrough curves in the presence of the solute adsorption on the grain walls. We then showed how calculating the distance map of the pore space can be combined together with the solute transport computation to model the possible mechanism for the enhanced model recovery when part of the pore space is occupied by a second immiscibly trapped fluid phase. We showed that even in such a simple model the interaction between the transport and the chemical reactions is non-trivial, i.e. the competition between diffusion and adsorption can prevent the solute from being dispatched to the oil/water/rock contact line. In reality the affinity of an ion towards the surface is influenced among other things by the surface charge (the effect which is not captured by the Langmuir adsorption isotherm employed in this Chapter) which in turn depends on the ionic composition of the brine. This may be one of the reasons for the sensitivity of the oil recovery to the ionic composition of the brine.

Finally, the major advantage of using the FE-FV method for the fluid flow simulations is its capability to simulate the transport phenomena along the 2D surfaces within a 3D domain. Due to this capability it is possible to formally include the sub-resolution surface films at the rock surface without modifying the mesh itself, as well as to model the solute diffusion along the oil-water or oil-rock interfaces, which are suggested to be the crucial mechanisms for dispatching the wettability altering agents to the oil-rock interface (Hammond and Unsal, 2009). We see this as a compelling reason to choose the FE-FV method over other alternatives to simulate the pore-scale reactive transport phenomena relevant to wettability alteration. To the best of our knowledge, no study

has been published to this date that deals with the pore-scale numerical investigation of how the chemical agents are actually dispatched to the oil-wet surfaces.

While the presented numerical methods are adequate for simulating the scenarios where the oil phase is immobile and the samples are completely oil-wet, their extension to the altering wettability effects and the transient motion of both fluid phases is non-trivial. Two possible avenues can be pursued to this effect. First, one can utilize the available two-phase extensions of the Navier-Stokes equation, such as the phase field or level-set methods, to solve the fully transient flow equations with the arbitrary wettability conditions. For instance, the level-set based approach reported by Prodanovic and Bryant (2006) is somewhat similar to what was described in this Chapter, but the use of the level-set method produces the correctly shaped non-spherical interfaces; also it does not solve the Navier-Stokes equations, i.e. the fluids are still assumed to be quasi-static. To this date, no research has been published on the application of the fully transient two-phase Navier-Stokes extensions to the problems of the pore-scale flows in realistic 3D geometries. A second way forward is to use the above described methods to condition the pore-network models, where the governing equations are simplified and the transient motion of fluid interfaces is avoided. This approach to simulating the reactive two-phase flow problems is an extension of the work presented by Hammond and Unsal (2012), where a simple analytical solution for a single pore throat was used to condition the pore network model, to the cases where no analytical solutions are available.

It should also be noted that in this work the 3D simulations were conducted on the mesh that corresponds to a fairly regular sandstone sample. The pore geometry of a carbonate rock is inherently much more complex due to the existence of multi-scale porosity types. Although our meshing procedure should apply equally well to a voxelized image of a carbonate rock, it is the omission of (sub-resolution) geometrical details during the production of this voxelized image that can present additional complexities. As indicated in the Introduction, the pore-scale coupling of flow effects at different scales of porosity in carbonates is a topic of the ongoing research.

To summarize, the tools that we presented in Chapters 2 and 3 laid the groundwork for the simulation of the pore-scale propagation of the reactive solutes and their chemical interaction with both the oil phase and

the rock. Hence, it is first necessary to identify what chemical interactions do occur in reality by analyzing the experimental data.

To this end, in the next chapter we will examine the experimental evidence of the chemical interaction between seawater and chalk as it is considered relevant to enhanced oil recovery in this type of rocks. We will then construct a numerical model that incorporates different chemical mechanisms in an attempt to elucidate which of these mechanisms can explain the experimental measurements.

Results of this chapter were presented in the following peer-reviewed publication:

- Y. Zaretskiy, S. Geiger, and K. S. Sorbie. Direct numerical simulation of pore-scale reactive transport: applications to wettability alteration during two-phase flow. *International Journal of Oil, Gas and Coal Technology*, in press.

CONTINUUM-SCALE MODELLING OF REACTIVE TRANSPORT

CONTENTS

4.1	Introduction	82
4.2	Review of published experimental data	83
4.2.1	Remarks on the published data	91
4.3	Numerical model	92
4.3.1	Aqueous chemistry	92
4.3.2	Surface adsorption	94
4.3.3	Mineral dissolution and precipitation	96
4.4	Modelling results	97
4.4.1	Fixed parameters	98
4.4.2	Fitting parameters and numerical breakthrough curves	99
4.4.3	Outlook for two-phase flow problems	111
4.5	Summary	112

4.1 INTRODUCTION

In the previous chapters we described the construction of a pore-scale simulator for both inert and reactive solute transport. In order to apply it to an actual problem of interest, i.e. wettability alteration in carbonate rocks, we should first determine what chemical reactions govern the fluid-rock interactions. As discussed in Chapter 1, there is some unambiguity in this question. One way to elucidate it is to use the numerical modelling as an explanation tool for the pertinent experimental measurements. To this end, we will review the previously published laboratory data on certain single-phase coreflooding experiments in carbonate rocks with seawater-like brines and construct a numerical model where we have a choice of what chemical effects to incorporate. Currently proposed governing effects include divalent ions adsorption and the mineral phases dissolution and precipitation. Therefore, we use the modelling approach

to determine whether the inclusion of either or both of these effects is necessary to reproduce the experimentally observed evolution of the effluent composition of the injected brines. In contrast to the previous chapters, here we employ a continuum-scale reactive transport modelling approach. This is because the data that we analyse, i.e. effluent breakthrough curves, is available at the continuum-scale and hence for the purpose of matching it the use of average porous medium representation is sufficient. Also, since we do not account for any heterogeneities within the porous samples we describe the solute transport as a 1D process.

We begin by presenting the published experimental data on seawater-chalk chemical interaction. We then describe how the 1D reactive transport problem is solved using the PHREEQC software. We describe various chemical effects that are included in our numerical model and what equations describe these effects. We then use the model to successfully simulate the described laboratory measurements. We finish with the discussion of what implications our results have for similar chemical effects two-phase flows.

4.2 REVIEW OF PUBLISHED EXPERIMENTAL DATA

The first set of relevant coreflood experiments for our purposes was summarized by Strand et al. (2006). Outcrop chalk from Stevns Klint, Denmark, was used as a core material. It is characterized by low permeability of 2–5 mD, high porosity of 45–50% and a specific surface area of 2 m²/g (Hiemenz and Rajagopalan, 1997). The core length was approximately 7 cm and the pore volume was about 44 ml.

Strand et al. (2006) looked at how SO_4^{2-} and Ca^{2+} influenced each others' interaction with the rock. For a given temperature a core sample was first flooded with three pore volumes of seawater with no sulphate, denoted SW_{ss} (sans sulphate) in Table 4.1. After that the injected fluid was changed to seawater with sulphate and an inert tracer (SW_{tr}) or to seawater with sulphate and an adjusted level of dissolved calcium ($\text{SW}_{1/2\text{ca}}$, SW_{ca} , $\text{SW}_{2\text{ca}}$, where a number in the subscripts denotes a $\text{Ca}^{2+}/\text{SO}_4^{2-}$ ratio). Experiments were conducted at five different temperature levels (in °C): 23, 40, 70, 100 and 130. All fluids were injected at a constant flow rate of 0.2 ml/min. Compositions of the brines from Strand et al. (2006) that are used in the subsequent modelling are listed in Table 4.1. Note that,

compared to data reported by Strand et al. (2006), the inert tracer in Table 4.1 was replaced by an additional amount of Cl^- to simplify the input for the numerical model. Some brines are excluded from the table as their corresponding breakthrough curves illustrate the same trends as the ones from Table 4.1 and hence these brines will not be included in the simulation. Key experimental results of Strand et al. (2006) are presented in Figures 4.1-4.2.

The main observations from there results are:

1. Fig. 4.1a: the level of sulphate rises above zero after just more than 1 PV of brine is injected. This implies that the flow of SO_4^{2-} ions is retarded within the rock and the retardation effect increases with temperature.
2. Fig. 4.1b: when SO_4^{2-} ions are present in the brine, a loss of Ca^{2+} occurs. Also, there is an indication of calcium production in the beginning of the flood as the relative calcium concentration starts above one.
3. Fig. 4.2: sulphate retardation increases with temperature and ratio of $\text{Ca}^{2+}/\text{SO}_4^{2-}$.

The second set of experiments we will consider was reported by Zhang et al. (2007). In this work Stevns Klint chalk was again used as a core material, characterized by the same length of 7 cm and a slightly smaller pore volume of about 29 ml.

Emphasis of the work of Zhang et al. (2007) was on comparing the interactions of Ca^{2+} and Mg^{2+} with the rock at different temperatures.

IONS [mol/l]	SW_{ss}	SW_{tr}	$\text{SW}_{1/2\text{ca}}$	SW_{ca}	$\text{SW}_{2\text{ca}}$
C(4)	0.002	0.002	0.002	0.002	0.002
Cl^-	0.623	0.549	0.524	0.525	0.526
SO_4^{2-}	—	0.024	0.024	0.024	0.024
Mg^{2+}	0.0445	0.0445	0.0445	0.0445	0.0445
Ca^{2+}	0.013	0.013	0.0065	0.013	0.026
Na^+	0.5	0.45	0.462	0.45	0.425
K^+	0.01	0.034	0.01	0.01	0.01

Table 4.1: Ionic compositions of brines used for coreflood experiments by Strand et al. (2006).

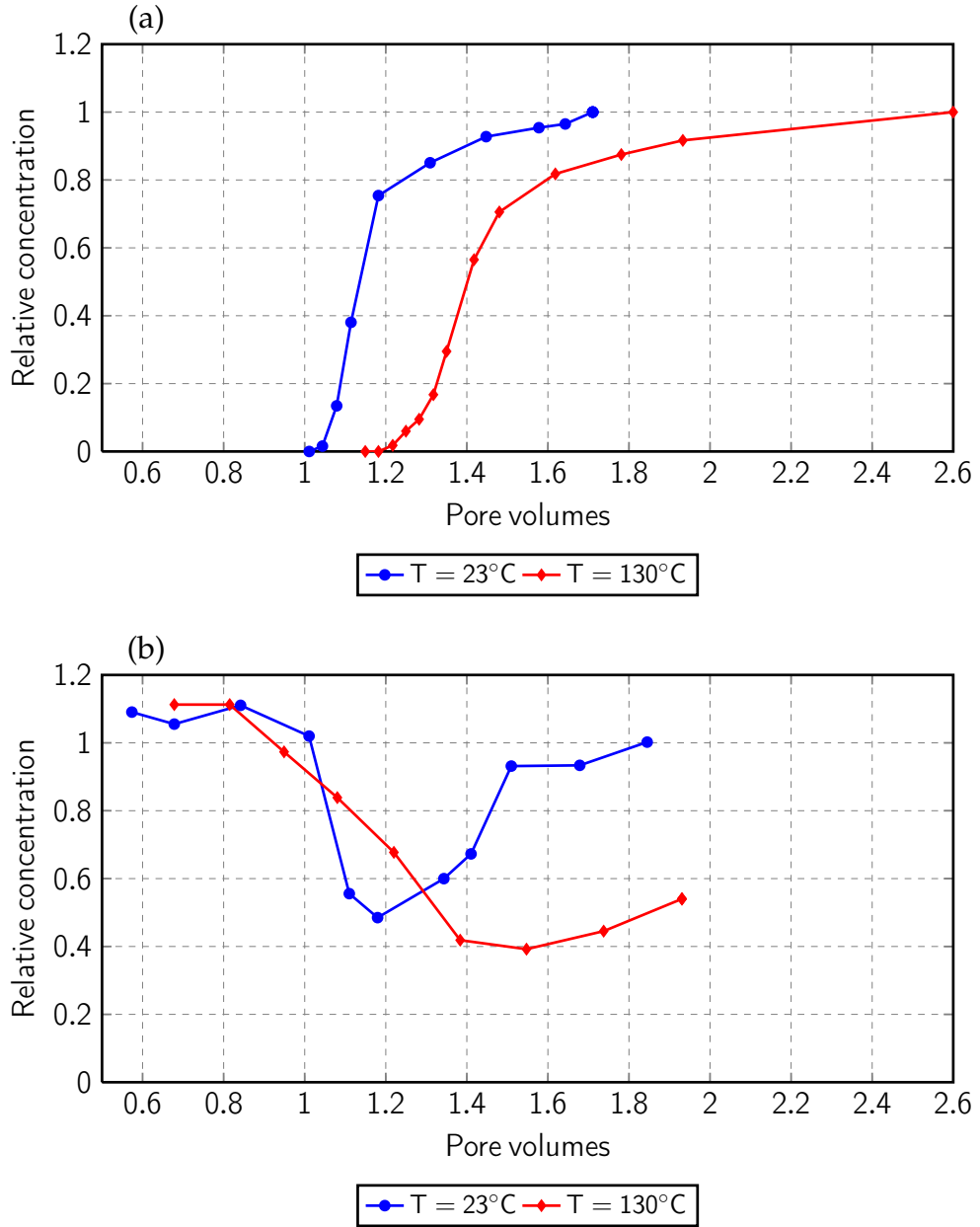


Figure 4.1: Experimentally measured (a) SO_4^{2-} and (b) Ca^{2+} breakthrough curves for 23 and 130 °C reproduced from the work by Strand et al. (2006). Concentrations are normalized with respect to their value in the injected brine. Experimental procedure consisted of injecting 3 PVs of SW_{ss} , followed by 3 PVs of SW_{tr} .

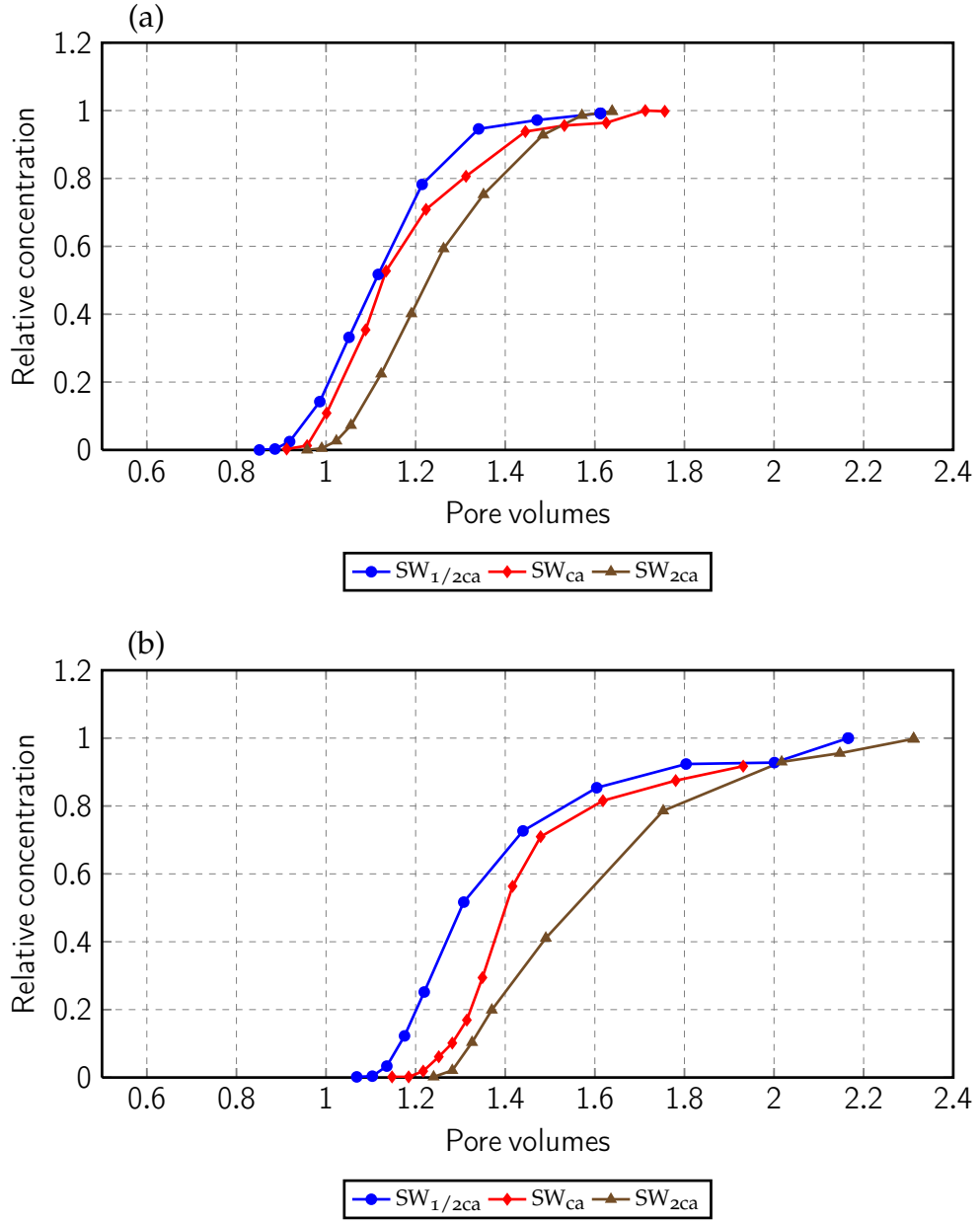


Figure 4.2: Experimentally measured SO_4^{2-} breakthrough curves for (a) 23 and (b) 130 °C and varied $\text{Ca}^{2+}/\text{SO}_4^{2-}$ ratios reproduced from the work by Strand et al. (2006). Concentrations are normalized with respect to their value in the injected brine. Experimental procedure consisted of injecting 3 PVs of SW_{ss} , followed by 3 PVs of either $\text{SW}_{1/2\text{ca}}$, SW_{ca} or $\text{SW}_{2\text{ca}}$, where a number in the subscripts denotes a $\text{Ca}^{2+}/\text{SO}_4^{2-}$ ratio.

To achieve this, a core was first saturated with a 0.573 M NaCl solution (denoted ZP brine in Table 4.2), followed by injection of CF-M brine at a flow rate of 0.2 ml/min for 2 (at 23 °C) or 3 PV (at 130 °C). CF-M is a seawater-like brine with no sulphate and equal amounts of calcium and magnesium. Another type of experiment reported by Zhang et al. (2007) involved saturating the core with seawater (SW) and then flooding it with SW for 4 PVs at a rate of 1 PV/day (0.02 ml/min) and temperatures ranging between 23 and 130 °C. Table 4.2 lists compositions of the utilized brines. Experimental breakthrough curves reported by Zhang et al. (2007) are presented in Fig. 4.3 and Fig. 4.4.

The observed evolution of Ca^{2+} and Mg^{2+} concentration levels demonstrates the following:

1. Fig. 4.3a: Calcium ions at 23 °C were more retarded than magnesium ones.
2. Fig. 4.3b: At 130 °C magnesium ions arrived later than calcium, indicating the possible substitution of Mg^{2+} for Ca^{2+} on the rock surface.
3. Fig. 4.4: At a lower injection rate and at lower temperatures of 23 and 70 (not shown) °C effluent Ca^{2+} concentration was the same as in the brine. At higher temperatures of 100 (not shown) and 130 °C effluent Ca^{2+} concentration was persistently elevated above its original level. The figure shows the results that will be used in the subsequent simulations. The omitted 70 °C curve essentially coincide with the measurements performed at 23 °C, results for 100 °C reach a plateau at the relative concentration of 1.2.

IONS [mol/l]	SW	ZP	CF-M
C(4)	0.002	–	–
Cl^-	0.525	0.573	0.569
SO_4^{2-}	0.024	–	–
Mg^{2+}	0.0445	–	0.013
Ca^{2+}	0.013	–	0.013
Na^+	0.45	0.573	0.504
K^+	0.01	–	0.013

Table 4.2: Ionic compositions of brines used for coreflood experiments by Zhang et al. (2007)

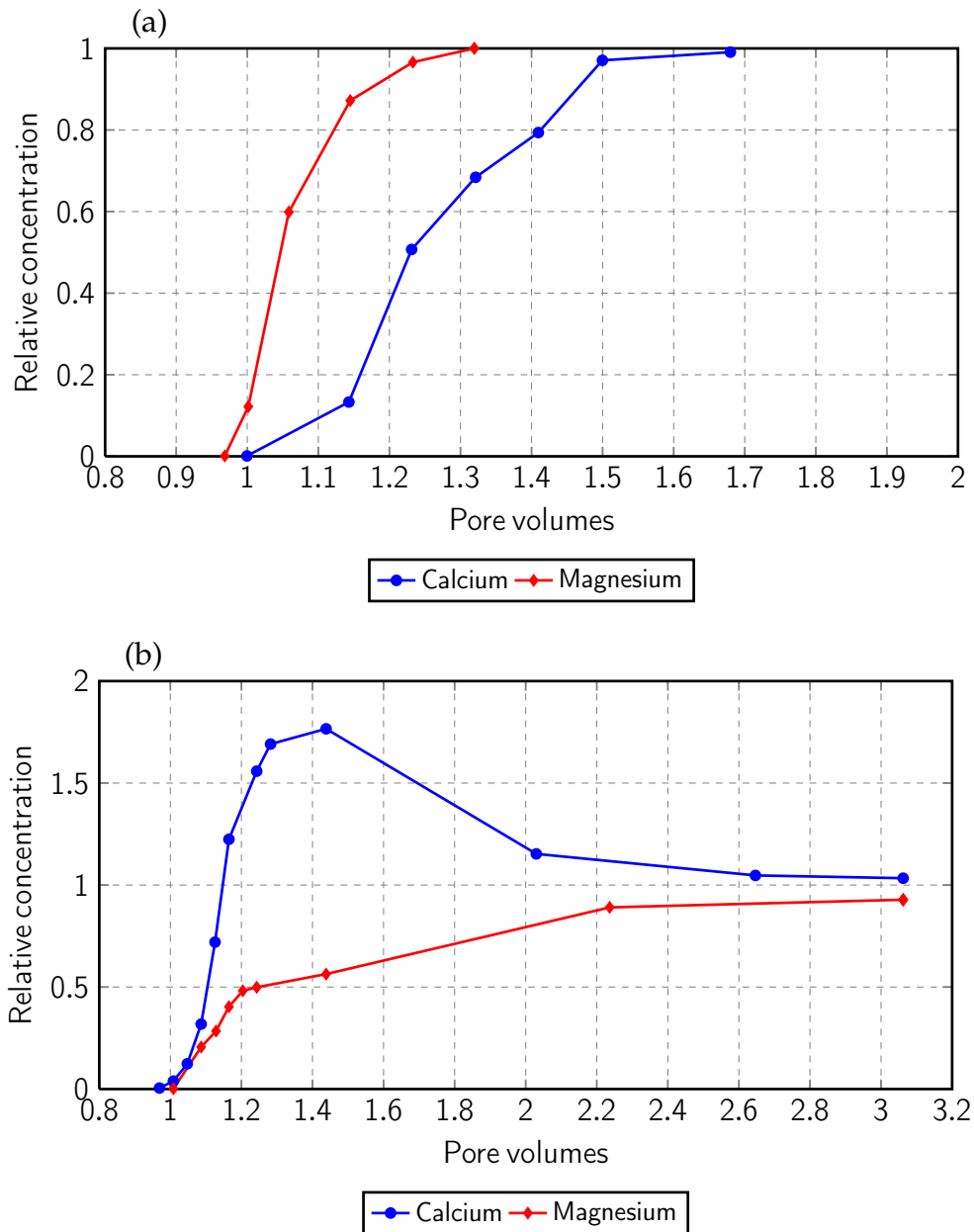


Figure 4.3: Experimentally measured Ca^{2+} and Mg^{2+} breakthrough curves for (a) 23 and (b) 130 °C reproduced from the work by Zhang et al. (2007). Concentrations are normalized with respect to their value in the injected brine. Experimental procedure consisted of saturating the core with a NaCl solution, followed by injecting 2 or 3 PVs of CF-M brine.

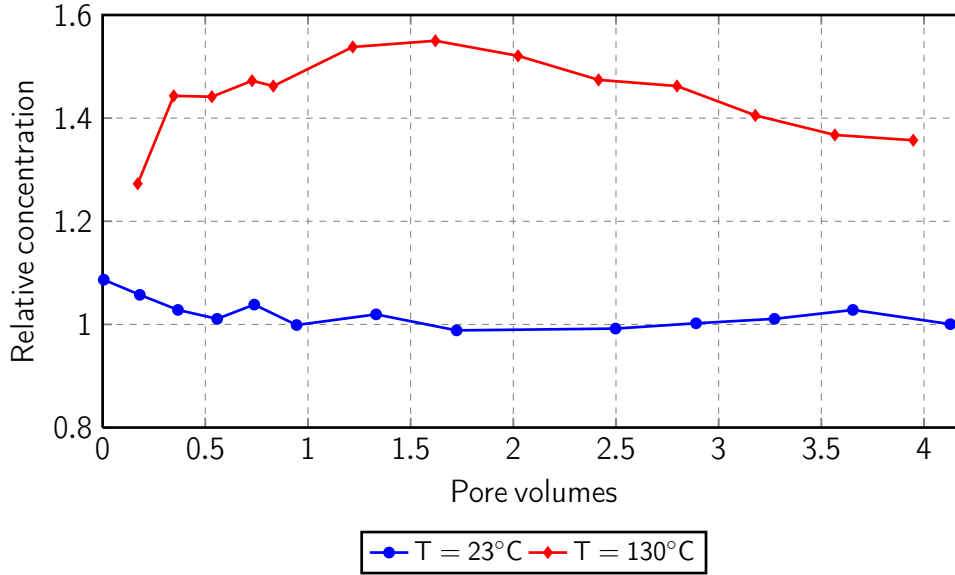


Figure 4.4: Experimentally measured Ca^{2+} breakthrough curves for 23 and 130 °C reproduced from the work by Zhang et al. (2007). Concentrations are normalized with respect to their value in the injected brine. Experimental procedure consisted of saturating the core with seawater, followed by injecting 4 PVs of the same brine.

The final set of experiments we discuss in this section was reported by Madland et al. (2011). In this work chalk cores were obtained from the quarries of Lixhe near Liège, Belgium. Liège chalk is characterized by porosity of 40-43% and permeability of 1–2 mD. The pore volume of all cores was approximately 33 ml.

A key objective of the work of Madland et al. (2011) was to investigate whether chemical interaction between the fluid and the rock occurs when brines with simpler chemical compositions are used. The main emphasis was on studying the rock compaction effects but effluent ionic concentration levels were also analysed. All experiments were conducted at 130 °C and at a constant flow rate of 1 PV/day. Here we consider two flood experiments from that publication, as all other floods demonstrated the same effects. Cores were initially saturated with distilled water. Two brines were used in the presented flood experiments: a MgCl_2 solution (MC) and seawater (SW). Their compositions are listed in Table 4.3. MC brine has been injected for 2 weeks while SW has been injected for three days. After three days the sample was occluded due to mineral precipitation. Experimental breakthrough curves reported by Madland et al. (2011) are presented in Fig. 4.5.

Following conclusions can be inferred from the these results:

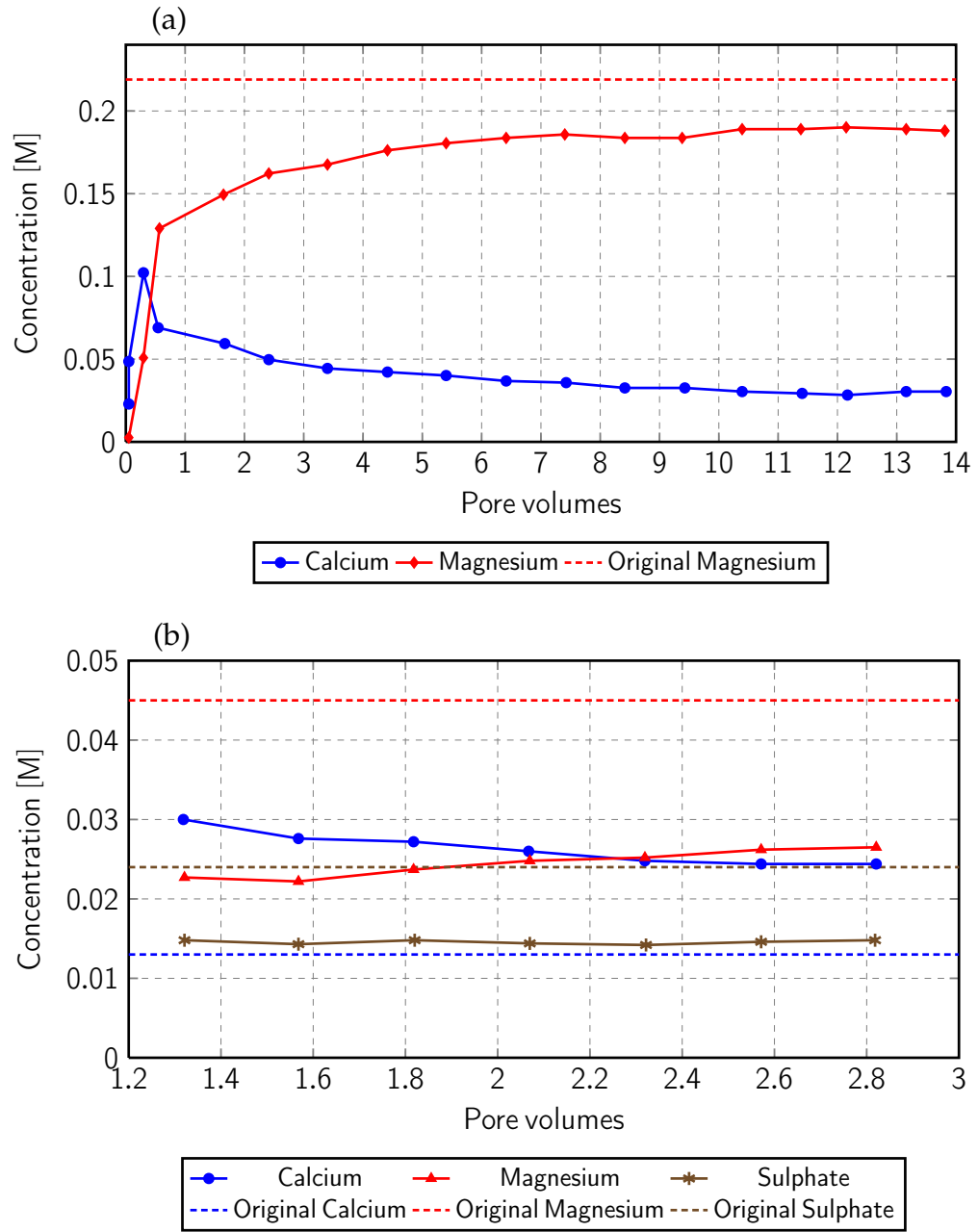


Figure 4.5: Experimentally measured breakthrough curves for (a) MgCl_2 and (b) seawater brines injected into chalk cores reproduced from the work by Madland et al. (2011). Concentrations are reported in mol/l. Experimental procedure consisted of saturating the core with distilled water, followed by injecting 14 or 3 PVs of the corresponding brine.

1. Fig. 4.5a: during the injection of MC brine sustainable loss of Mg^{2+} and equal production of Ca^{2+} were observed throughout the whole duration of the experiment. No loss of Cl^- occurred. Moreover, after an initial surge, the production of Ca^{2+} gradually decreased until about 12 PVs of the brine had been injected.
2. Fig. 4.5b: during the injection of SW brine the production of Ca^{2+} was less than the loss of Mg^{2+} and an additional loss of SO_4^{2-} ions occurred.

4.2.1 Remarks on the published data

It is argued by Strand et al. (2006) and Zhang et al. (2007) that the chemical interaction between seawater-like brines and chalk rocks occurs in the form of adsorption processes, i.e. surface reactions. Namely, SO_4^{2-} adsorbs onto the rock surface and reduces the positive charge of the chalk. This facilitates the co-adsorption of Ca^{2+} and, at higher temperatures, the substitution of Mg^{2+} for Ca^{2+} . Experiments of Madland et al. (2011) demonstrate that: (1) the presence of sulphate ions is not necessary for this substitution to occur; (2) this process can be maintained for many pore volumes. The latter fact implies that the process is more likely to be volumetric in nature, i.e. dissolution/precipitation rather than adsorption. To support this conjecture, we can estimate the total production of calcium during the experiments and compare it to the number of available adsorption sites N_σ . A waterflood with MgCl_2 solution, reported by Madland et al. (2011), stopped when 453.4 ml (14 PVs) of fluid were injected.

IONS [mol/l]	MC	SW
C(4)	–	0.002
Cl^-	0.438	0.525
SO_4^{2-}	–	0.024
Mg^{2+}	0.219	0.0445
Ca^{2+}	–	0.013
Na^+	–	0.45
K^+	–	0.01

Table 4.3: Ionic compositions of brines used for coreflood experiments by Madland et al. (2011)

Throughout the experiment the average effluent concentration of calcium was about 0.035 M. This gives a total of $453 \cdot 0.035/1000 = 1.6 \cdot 10^{-2}$ mol of Ca^{2+} . According to Madland et al. (2011), $N_{\sigma} = 1.9 \cdot 10^{-3}$ mol, which is an order of magnitude less. Moreover, as indicated in the previous chapter, the adsorption preferentially occurs along the high-velocity pathways and hence even less surface sites would be involved in Ca^{2+} desorption when the brine is injected in the sample.

Nevertheless, Ca^{2+} dissolution and anhydrite precipitation do not take place at room temperature and hence a retardation of SO_4^{2-} observed by Strand et al. (2006) and Ca^{2+} and Mg^{2+} observed by Zhang et al. (2007) should probably be ascribed to adsorption. Consequently, based on the initial evidence we formulate the following hypothesis subject to the subsequent verification – *in order to reproduce the observed experimental phenomena in a numerical model, it has to incorporate both surface adsorption and volumetric dissolution/precipitation effects*. This will be discussed in the next section.

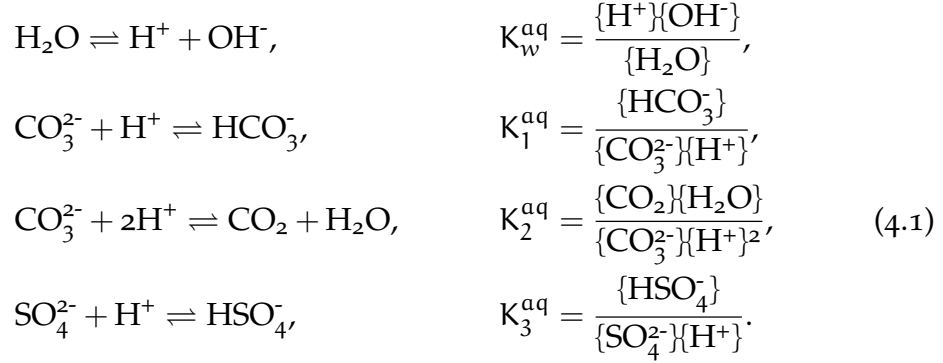
4.3 NUMERICAL MODEL

The model is constructed using PHREEQC (Charlton and Parkhurst, 2011), which is a geochemical modelling programme capable of simulating a wide range of chemical reactions (e.g. aqueous equilibrium, adsorption, kinetic mineral dissolution and precipitation) as well as 1D advection-dispersion-reaction transport, governed by Eq. 3.1. It uses an explicit finite difference scheme to solve the transport part, which is central in space for dispersion and upwind for advection. Chemical equilibrium is calculated using mass-action equations. The Newton-Raphson method with an optimization suggested by Barrodale and Roberts (1980) is used to solve the resulting system of non-linear equations. Kinetic reactions are integrated in time using the CVODE algorithm (Cohen and Hindmarsh, 1996). In the following sections we will concentrate on the chemical reactions we incorporate in our PHREEQC model.

4.3.1 Aqueous chemistry

As a first step, we include chemical reactions in the liquid phase. The dissolved species in the aqueous phase are assumed to be in thermo-

dynamic equilibrium. This equilibrium requires that at every transport node the mass-action equations for all possible association reactions between the master species are satisfied. Master species are those species for which the transport equation is solved. The following master species are considered in our model: H^+ , Ca^{2+} , CO_3^{2-} , H_2O , Na^+ , Cl^- , Mg^{2+} , SO_4^{2-} , K^+ . The resulting association reactions between these species and the corresponding mass-action equations are as follows (master species are on the left hand side of the reactions)



Here $\{\cdot\}$ denotes the dimensionless activity a_i of a specific species; K_w^{aq} , K_1^{aq} , K_2^{aq} , and K_3^{aq} are equilibrium constants for the corresponding aqueous reactions. Notice that the activity of water is explicitly included as it does not necessarily equal unity in PHREEQC. CO_2 in the above equations denotes CO_2 dissolved in the water rather than the gaseous phase. It should also be noted that it is argued by Strand et al. (2006) and Zhang et al. (2007) that the association between Mg^{2+} and SO_4^{2-} ions should take place at higher temperatures. However, SO_4^{2-} breakthrough curves do not reflect a decrease in sulphate due to this reaction. Hence it was excluded from the model.

The activity a_i is related to molality m_i [mol/kgw] as $a_i = \gamma_i m_i / m_i^\ominus$, where m_i^\ominus is the molality at the standard conditions and γ_i is the dimensionless activity coefficient, calculated in PHREEQC with the Davies equation

$$\log_{10} \gamma_i = -Az_i^2 \left(\frac{\sqrt{I_0}}{1 + \sqrt{I_0}} - 0.3I_0 \right), \tag{4.2}$$

where z_i is the dimensionless ionic charge of aqueous species i , A is a temperature-dependent constant and I_0 is the ionic strength of the solution [mol/kgw]

$$I_0 = 0.5 \sum_i m_i z_i^2. \tag{4.3}$$

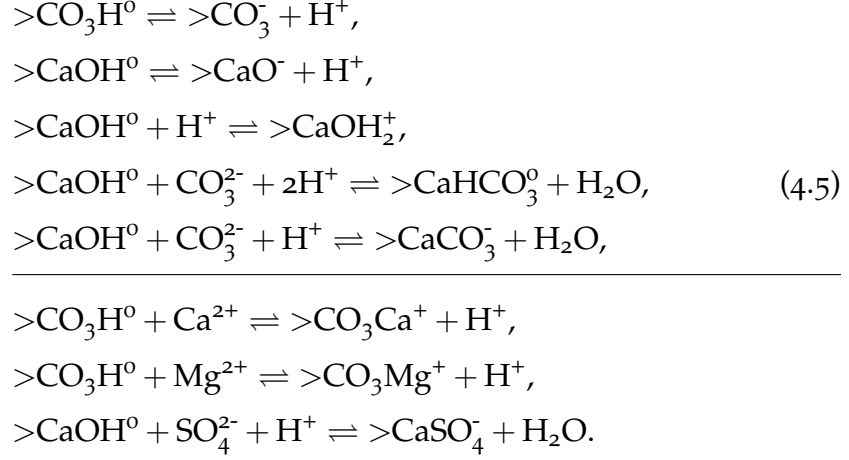
Finally, the following aqueous charge balance equation must also hold for the dissolved species

$$\sum_i m_i z_i = 0. \quad (4.4)$$

4.3.2 *Surface adsorption*

Akin to ion association in the aqueous phase, ions can also form complexes at the solid rock surfaces which are in contact with the fluid. The surface complexes are also assumed to be in thermodynamic equilibrium. The basic theory of surface-complexation reactions was presented by Dzombak and Morel (1990). It requires the following parameters to be specified: the number of active sites T_s [sites/nm²], the specific area [A_s [m²/g]], and the mass of the solid S_s [g]. For every surface reaction the model includes two additional unknowns in its mass-action equation as compared to aqueous reactions: (1) the surface potential Ψ_s [V] and the activity of the surface species. Therefore, the surface potential and, hence, surface charge are explicitly calculated in this method. We consider the surface-complexation model between the fluid and the calcite rock as derived by Pokrovsky and Schott (2002). It assumes that $>\text{CO}_3\text{H}^0$ and $>\text{CaOH}^0$ are the master surface species, present in equal amount on the carbonate surface. We specify $T_s = 2$ sites/nm² for both $>\text{CO}_3\text{H}^0$ and $>\text{CaOH}^0$ (Hiorth et al., 2010a), and the specific area $A_s = 2$ m²/g (Hiemenz and Rajagopalan, 1997). Note that both species are neutral because they share one of the electrons. All other surface complexes can be expressed in terms of the master species with the following reactions

(the horizontal line separates reactions that describe the adsorption of the relevant divalent ions)



Here $>$ denotes a surface species. If we consider, for instance, the last (eighth) reaction from this system, then the following mass-action equation has to be satisfied

$$K_8^{\text{surf}} = \frac{\overbrace{\{>\text{CaSO}_4^-\}\{\text{H}_2\text{O}\}}^{\text{usual mass-action equation}}}{\{>\text{CaOH}^0\}\{\text{SO}_4^{2-}\}\{\text{H}^+\}} \times \overbrace{\exp\left(\frac{F\Psi_s}{RT}\Delta Z\right)}^{\text{charge interaction}}, \tag{4.6}$$

where, in addition to the already defined surface potential Ψ_s ,

K_i^{surf} surface equilibrium constant, $i = 1 \dots 8$

F Faraday's constant, $F = 96485 \text{ C/mol}$

R ideal gas constant, $R = 8.314 \text{ J/(K}\cdot\text{mol)}$

T absolute temperature, K

ΔZ net change in surface charge, $\Delta Z = -1$ in this example

In PHREEQC the activity of a surface species is equal to its mole fraction among all species that can occupy the surface site. In other words, a surface species has activity of one when it completely covers a given surface site. This is different from the work of Dzombak and Morel (1990) where the activity of a surface species is assumed equal to its concentration.

The exponential factor in the mass-action equation accounts for the work required to move the charged ions away from the surface. It effectively reduces activities of ions with the charge of the same sign as that of the surface; and increases activities for ions with the charge of

the opposite sign. The surface potential is related to the surface-charge density σ_s [C/m²] by the Grahame equation (Israelachvili, 2011)

$$\sigma_s = \sqrt{8000\epsilon\epsilon_0RTI_0} \sinh\left(\frac{F\Psi_s}{2RT}\right), \quad (4.7)$$

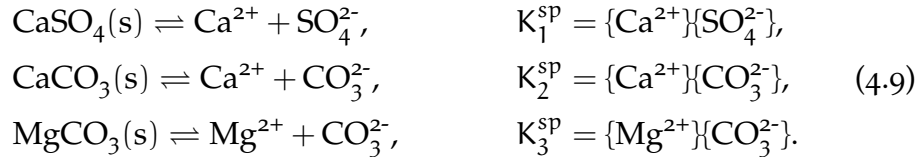
where ϵ is the dielectric constant of water, ϵ_0 is the permittivity of free space, $\epsilon_0 = 8.854 \times 10^{-12}$ C²/(m·J). σ_s is defined as

$$\sigma_s = \frac{F}{A_s S_s} \sum_{i_s} m_{i_s} z_{i_s}, \quad (4.8)$$

where summation is over all surface species.

4.3.3 Mineral dissolution and precipitation

Finally, we incorporate the effects of mineral dissolution and precipitation. We consider three mineral phases: calcite (CaCO₃), which is present initially, magnesite (MgCO₃), and anhydrite (CaSO₄), both of which can precipitate from the aqueous solution. At temperatures below 70 °C gypsum (CaSO₄·2H₂O) is less soluble than anhydrite, but brines from the previous section are not oversaturated with gypsum and hence it was discarded as a potential mineral phase. Reactions that describe equilibrium between the solution and these phases are



Here K_i^{sp} denotes the corresponding solubility product. The time scale associated with dissolution and precipitation is usually comparable with (or even larger than) the pore residence time determined by solute transport. Therefore, it is important to model these effects as kinetic rather than instantaneous reactions (Steefel and Lasaga, 1994). To this end, they

are introduced into the model as the following ordinary differential equations

$$\begin{aligned}\frac{d[\text{CaSO}_4(\text{s})]}{dt} &= k_1 \left(1 - \frac{\{\text{Ca}^{2+}\}\{\text{SO}_4^{2-}\}}{K_1^{\text{sp}}} \right), \\ \frac{d[\text{CaCO}_3(\text{s})]}{dt} &= k_2 \left(1 - \frac{\{\text{Ca}^{2+}\}\{\text{CO}_3^{2-}\}}{K_2^{\text{sp}}} \right), \\ \frac{d[\text{MgCO}_3(\text{s})]}{dt} &= k_3 \left(1 - \frac{\{\text{Mg}^{2+}\}\{\text{CO}_3^{2-}\}}{K_3^{\text{sp}}} \right).\end{aligned}\tag{4.10}$$

Here $[\cdot]$ denotes moles of a solid phase and k_i are the kinetic rate constants of the corresponding heterogeneous reactions [mol/s]. It can be easily seen that at equilibrium, i.e. when some of equations (4.9) are satisfied, the right-hand side of the corresponding equation from (4.10) becomes zero and hence no additional change in moles of the solid phase takes place.

It should be noted that the functional form of Eqns. (4.10) is a typical way to introduce the reaction rates when the exact experimental data about them is lacking. Despite the fact that more detailed studies on description of calcite precipitation and dissolution rates were presented by Plummer et al. (1978), they cannot be directly used in our model because of the difference in temperature and pressure conditions between (Plummer et al., 1978) and the experiments we consider. Moreover, Yoon et al. (2012) demonstrated that the model of Plummer et al. (1978) cannot explain the experimental dynamics of calcite precipitation and dissolution even for idealized porous medium. This is probably due to the fact that the kinetic rates are measured using the finely crushed rock samples which maximizes the available reaction surface. Therefore, we treat all the reaction rates as fitting parameters rather than relying on the published data.

4.4 MODELLING RESULTS

In what follows we will use the constructed model to simulate the experiments presented in Section 4.2. This will allow us to establish whether (and which of) the described components of the chemical model can explain the observed experimental behaviour. There are six variables in the model that we use as fitting parameters and our goal is to seek

what values, when assigned to these parameters, would yield numerical results that satisfactorily and consistently reproduce the complete set of experimental data. Both fitting and fixed parameters will be described in the next subsection. It should be noted that the fitting procedure in this Section is not conducted in a least-squares sense, as in Section 2.3.3, but rather as a manual trial-and-error process. This is due to the fact that there are no means available to automate the PHREEQC simulations.

4.4.1 Fixed parameters

Temperature-dependent equilibrium constants K_w^{aq} , K_1^{aq} , K_2^{aq} , and K_3^{aq} for aqueous reactions were taken from the standard PHREEQC database. Equilibrium constants K_i^{surf} for surface reactions listed above the horizontal line in Section 4.3.2 were taken from the work of Pokrovsky and Schott (2002), where only data for 23 °C is provided. It was found in the course of the modelling that these reactions do not influence the behaviour of the relevant breakthrough curves. Hence their equilibrium constants at 130 °C were modified to reflect the behaviour of the steady-state chemical model presented by Hiorth et al. (2010a) and no further effort was made to adjust these values.

Temperature-dependent solubility products K_i^{sp} in the functional form of Eq. 4.11 were obtained from the literature

$$\log_{10} K = A_1 + A_2 T + \frac{A_3}{T} + A_4 \log_{10} T + \frac{A_5}{T^2}, \quad (4.11)$$

where A_i are the fitting parameters with no particular physical meaning. Data for magnesite was taken from the work of Bénézech et al. (2011). Data for calcite and anhydrite was taken from the work of Kaasa (1998), where experimental measurements by Ellis (1959); Plummer and Busenberg (1982); Wolf et al. (1989) were used to fit (4.11) for CaCO_3 and measurements by Haarberg et al. (1992) were used for CaSO_4 . Results for all minerals are summarized in Table 4.4.

Finally, as mentioned above, reaction rates for mineral dissolution and precipitation were also considered as fitting parameters.

Each 1D numerical grid was discretized in $n = 40$ cells, i.e.

$$\Delta x = L/n, \quad (4.12)$$

MINERAL	A_1	A_2	A_3	A_4	A_5
CaCO_3	1322.11	0.163337	-74008.12	-475.704	4.0908×10^6
CaSO_4	5.0635	-0.020946	-970.388	–	–
MgCO_3	7.267	-0.033918	-1476.604	–	–

Table 4.4: Coefficients in Eq. 4.11 for the relevant thermodynamic solubility products.

where L is the core length [m]. PHREEQC uses explicit time-stepping scheme, therefore defining the time-step simultaneously defines the advecting velocity [m/s], $U = \Delta x / \Delta t$. Velocity for a given experiment can be calculated from an injection rate Q [ml/s] and a pore volume v [ml], $U = QL/v$. Hence,

$$\Delta t = v / Qn. \quad (4.13)$$

PHREEQC uses operator splitting to couple advection with dispersion and reactions, similar to how it is done in Chapters 2 and 3 of this thesis. Since it uses explicit time discretization, the advection time step is automatically subdivided into several dispersion steps to minimize the numerical errors, and for each dispersion step a further subdivision takes place when ODEs for kinetic reactions are integrated. Sample dispersivity D was set to 1.5×10^{-9} for 23 °C and 5×10^{-9} for 130 °C to give a satisfactory fit across all simulations. This value corresponds to a dispersion coefficient of $\alpha = L/100$ (such that $D = \alpha U$), which is within physically justified limits (Gelhar et al., 1992).

4.4.2 Fitting parameters and numerical breakthrough curves

Six parameters are chosen as the fitting parameters: K_6^{surf} , K_7^{surf} , K_8^{surf} , k_1 , k_2 , k_3 . Figures 4.6-4.11 show numerically computed breakthrough curves along with the corresponding experimental data. Values of all fitting parameters are presented in Table 4.5. The first three data columns correspond to simulations ran at $T = 23$ °C, and the remaining ones – to simulations at $T = 130$ °C. We reiterate that the main goal of this chapter was not to reproduce every measurement as closely as possible, each time adjusting the fitting parameters to obtain a perfect match. Rather we wanted to obtain a single set of parameters that would not change (as long as the T is constant) from one run to another and would yield a model capable of reproducing all the measurements, thus confirming or

Table 4.5: Summary of parameters used to fit the numerical model to experimental data. STR refers to Strand et al. (2006), ZH to Zhang et al. (2007), MDL to Madland et al. (2011). Subscript in a model title denotes temperature, sw designates experiments with seawater as the injected brine, MC - with MgCl_2 solution.

PARAMETER	MODEL									
	STR ₂₃	ZH ₂₃	ZH SW ₂₃	STR ₁₃₀	ZH ₁₃₀	ZH SW ₁₃₀	MDL MC ₁₃₀	MDL SW ₁₃₀	MDL SW ₁₃₀	
CaSO_4 rate, k_1	–	–	–	3×10^{-11}	–	3×10^{-11}	–	3×10^{-11}		
CaCO_3 rate, k_2	1×10^{-10}	2.5×10^{-11}	2.5×10^{-11}	1×10^{-10}	3×10^{-10}	2×10^{-10}	complex*	3×10^{-10}		
MgCO_3 rate, k_3	–	–	–	$1 \times 10^{-9\dagger}$	$5 \times 10^{-9\dagger}$	5×10^{-9}	1×10^{-8}	1×10^{-8}		
$>\text{CO}_3\text{Ca}^+$ eq. const., K_6^{surf}	–4.2	–4.2	–4.2	–3.5	–3.5	–3.5	–3.5	–3.5		
$>\text{CO}_3\text{Mg}^+$ eq. const., K_7^{surf}	–4.73	–4.73	–4.73	–2.8	–2.8	–2.8	–2.8	–2.8		
$>\text{CaSO}_4^-$ eq. const., K_8^{surf}	14.15	–	14.15	15.5	–	15.5	–	15.5		

[†] Additionally, the reaction order was modified.

* Ultimate value was 3×10^{-10} , same as in the other experiments at this temperature.

refuting our hypothesis, formulated in Section 4.2.1. It can be seen that for a given value of T the surface reaction constants are the same across different models, and kinetic rates vary by no more than a factor of five. A dash symbol in Table 4.5 means that a particular reaction did not occur in a simulation, e.g. no precipitation of anhydrite or magnesite took place at the room temperature.

As evident from Figs. 4.6-4.11, our 1D reactive transport model qualitatively reproduces the observed experimental evolution of the breakthrough curves:

1. Fig. 4.6a: increased retardation of SO_4^{2-} between 23 and 130 °C was reproduced by increasing the equilibrium constant of the corresponding surface reaction (last row in Table 4.5). These values were adjusted to match the arrival times of SO_4^{2-} . Numerical curves are characterized by higher mechanical dispersion than the experimental ones, probably because the cores used by Strand et al. (2006) had lower dispersivity than the cores utilized in other works.
2. Fig. 4.6b: a dip in calcium was observed at both temperatures, although the shift in the dip position is much smaller in the simulations as compared to the experimental curves. Possible reasons again include the lower sample dispersivity or a different surface affinity towards calcium compared to other samples. At lower temperature the dip is attributed solely to the change in surface affinity towards the Ca^{2+} ions due to the alteration of the surface charge. This is demonstrated in Fig. 4.7, where it is seen that the surface potential becomes more negative once the sulphate-rich brine is injected into the core, hence attracting more calcium. Moreover, the Ca^{2+} dip at the higher temperature could only be reproduced when an order of magnesite precipitation was set to two, i.e. the corresponding ODE assumed the form

$$\frac{d[\text{MgCO}_3(\text{s})]}{dt} = k_3 \left(1 - \frac{\{\text{Mg}^{2+}\}\{\text{CO}_3^{2-}\}}{K_{\text{sp}}^3} \right)^2. \quad (4.14)$$

As indicated by Saldi et al. (2009) magnesite precipitation at temperatures above 100 °C is actually described with a second order kinetic reaction. We found that when modelling experiments with high injection rates (approximately 10 PV/day), the data was reproduced

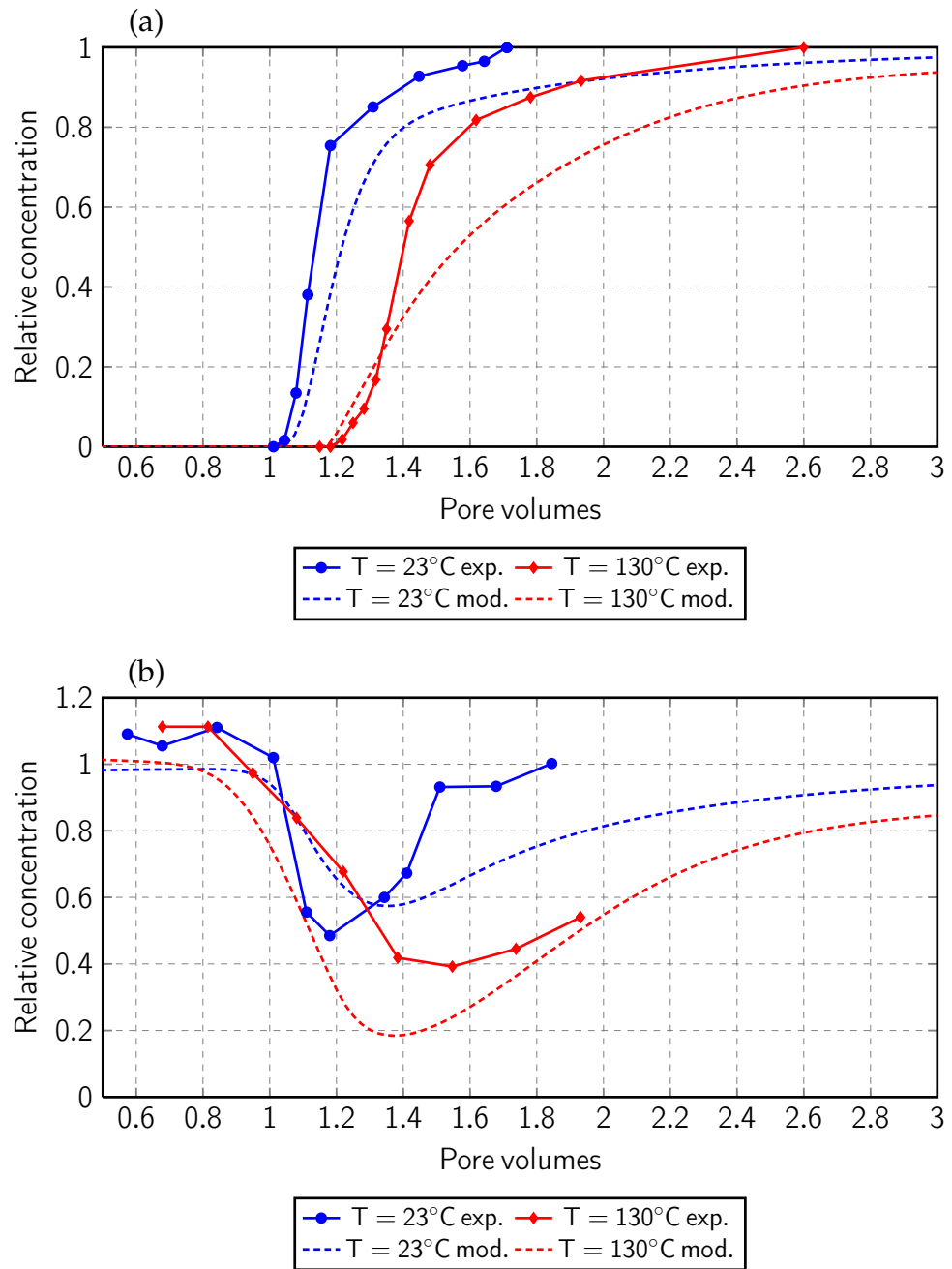


Figure 4.6: Experimentally measured and modelled (a) SO_4^{2-} and (b) Ca^{2+} breakthrough curves for 23 and 130 °C for a chalk core flooded with sw_{tr} brine. Concentrations are normalized with respect to their value in the injected brine. The fluid was injected at a rate of 6.5 PV/day.

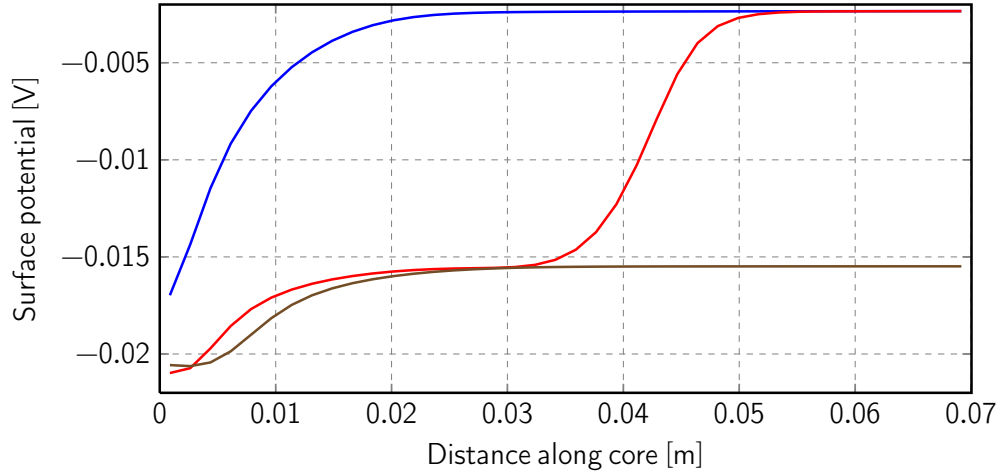


Figure 4.7: Evolution of surface potential along the core during the simulation of the SW_{tr} brine injection at 23 °C. Blue curve corresponds to the initial potential distribution, red curve corresponds to the injection of approximately 0.5 PV of the brine and brown curve shows the potential distribution at the end of the simulation.

when the second order was specified for this reaction. However, experimental data obtained at a lower injection rate of 1 PV/day was reproduced when the order was reverted back to unity. According to Saldi et al. (2009), the first order of a precipitation reaction suggests that the crystal growth is limited by the transport, which is consistent with the fact that when the injection (i.e. transport) was slower, the order had to be reduced.

3. Fig. 4.8: a shift of sulphate breakthrough curves with varying Ca^{2+}/SO_4^{2-} ratios was reproduced. As described in Section 4.3.2, the activity of species involved in a surface reaction is affected by the surface potential. Increased Ca^{2+}/SO_4^{2-} ratio makes the surface more positive as more Ca^{2+} is adsorbed and hence increases the amount of adsorbed SO_4^{2-} , thus shifting the sulphate breakthrough curves to the right.
4. Fig. 4.9: the equilibrium constant for the calcium adsorption is slightly higher than that for the adsorption of magnesium. At 130 °C the opposite is true (rows 4 and 5 in Table 4.5) and the difference between the constants is increased. At 23 °C this results in the Ca^{2+} curve being displaced to the right compared to the Mg^{2+} one. At the higher temperature the Mg^{2+} curve is positioned to the right of the Ca^{2+} one and the calcium concentration goes above its initial level as Ca^{2+} ions from the rock surface are substituted with Mg^{2+} .

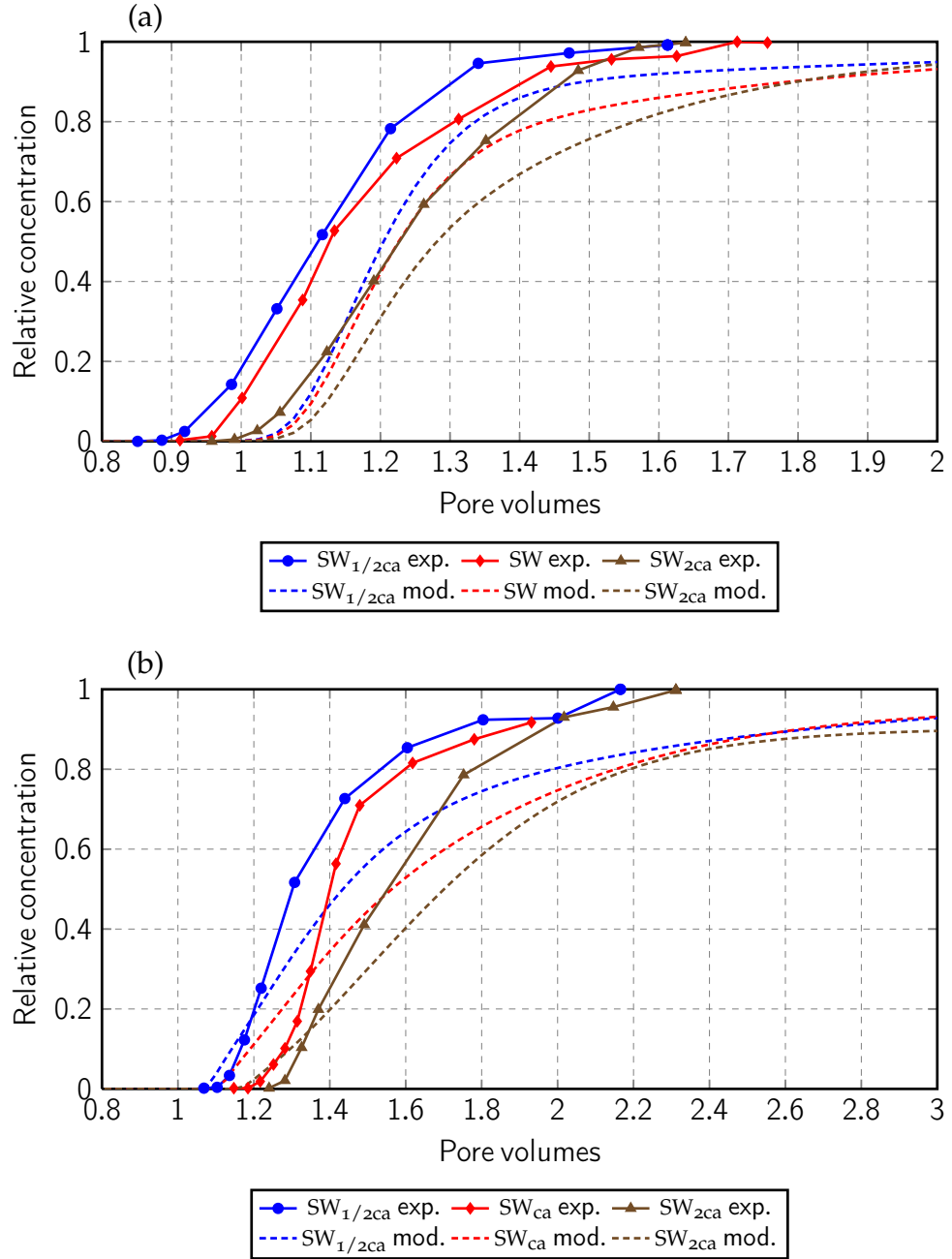


Figure 4.8: Experimentally measured and modelled SO_4^{2-} breakthrough curves for (a) 23 and (b) 130 °C and varied $\text{Ca}^{2+}/\text{SO}_4^{2-}$ ratios for a chalk core flooded with either $\text{SW}_{1/2\text{ca}}$, SW_{ca} or $\text{SW}_{2\text{ca}}$ brine. Concentrations are normalized with respect to their value in the injected brine. The fluid was injected at a rate of 6.5 PV/day.

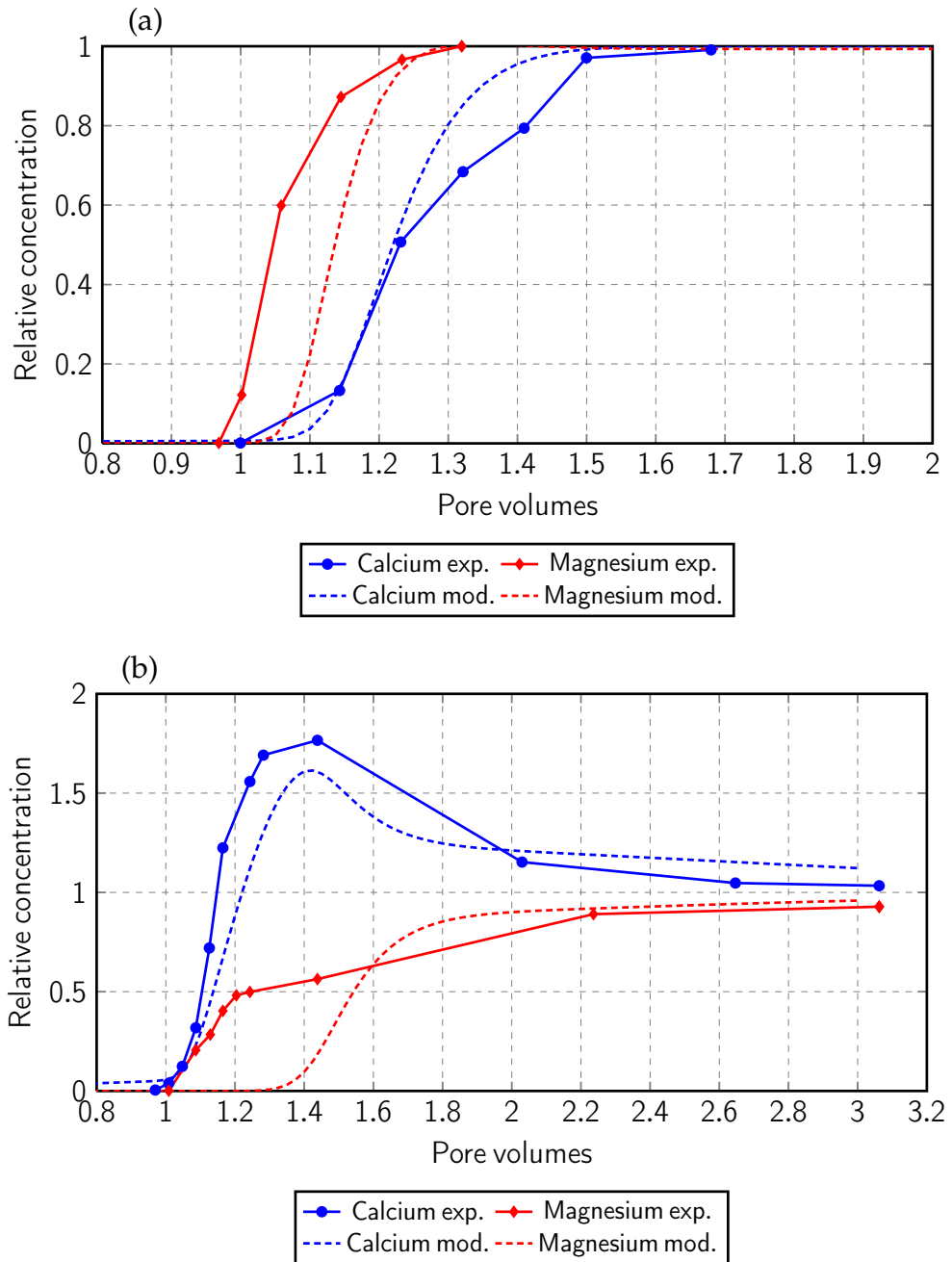


Figure 4.9: Experimentally measured and modelled Ca^{2+} and Mg^{2+} breakthrough curves for (a) 23 and (b) 130 °C for a chalk core flooded with CF-M brine. Concentrations are normalized with respect to their value in the injected brine. The fluid was injected at a rate of 10 PV/day.

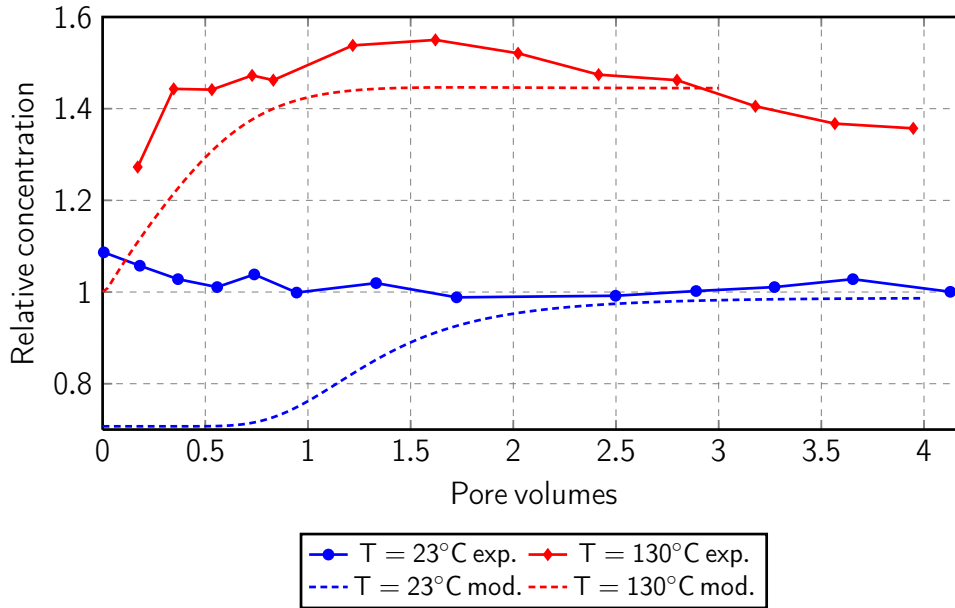


Figure 4.10: Experimentally measured and modelled Ca^{2+} breakthrough curves for 23 and 130 °C for a chalk core flooded with seawater. Concentrations are normalized with respect to their value in the injected brine. The fluid was injected at a rate of 1 PV/day.

It is not clear why at 130 °C experimentally measured concentration levels for both Ca^{2+} and Mg^{2+} rise above zero at the same time.

5. Fig. 4.10: at 23 °C seawater is in equilibrium with calcite and no persistent loss or production of Ca^{2+} ions takes place. At 130 °C the precipitation of MgCO_3 and the concomitant dissolution of CaCO_3 engenders the continuous production of Ca^{2+} . The initial difference between numerically computed and experimentally measured Ca^{2+} levels at 130 °C can be probably attributed to the difference in pH levels. Numerical levels of pH were calculated by specifying the full ionic composition of the solutions and then satisfying the charge conservation law 4.4. However, pH also depends on the partial pressure of CO_2 in equilibrium with the brine and this parameter is not reported in the literature. This can result in the discrepancy between the initial regions of the experimental and numerical breakthrough curves.
6. Fig. 4.11a: the production of Ca^{2+} and loss of Mg^{2+} were numerically observed during the slow injection of the MgCl_2 solution. However, an initial surge of calcium and its subsequent gradual decline along with a slow buildup of magnesium could not be reproduced with the constant reaction rates. As suggested by Hiorth et al.

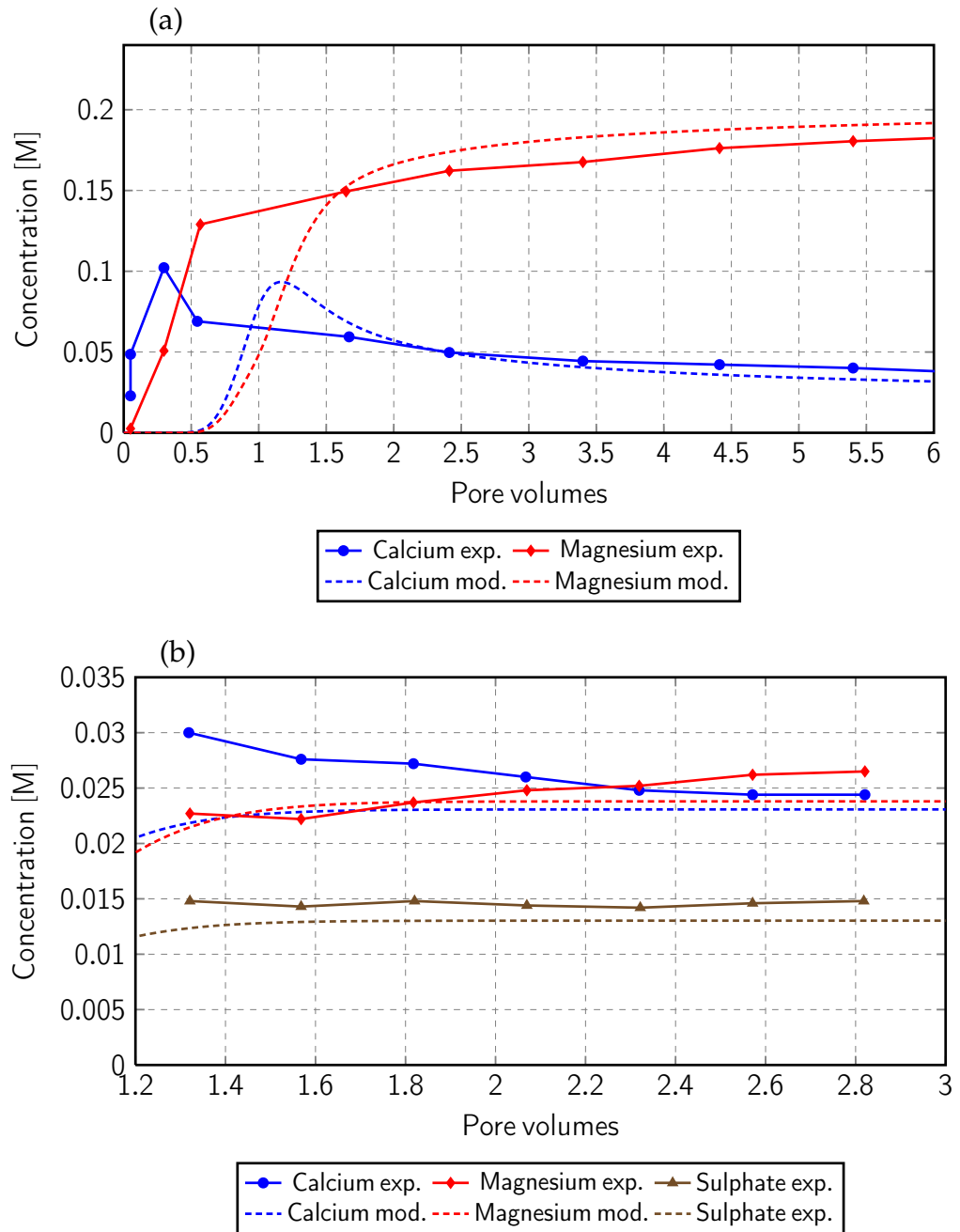


Figure 4.11: Experimentally measured and modelled breakthrough curves for (a) MgCl_2 and (b) seawater brines injected into chalk cores. Concentrations are reported in mol/l. The fluid was injected at a rate of 1 PV/day.

(2010b) magnesium can inhibit the dissolution of calcite and that the following expression should be used for a calcite dissolution rate

$$k = k_0 \frac{1 + k^*[\text{MgCO}_3]}{1 + k^{**}[\text{MgCO}_3]}. \quad (4.15)$$

To obtain the numerical breakthrough curves we used the above expression with $k_0 = 1.5 \times 10^{-7}$, $k^* = 5 \times 10^3$, $k^{**} = 5 \times 10^6$, determined by trial-and-error. At the end of the experiment there was about 2×10^{-4} moles of magnesite precipitated in every grid cell. It can be easily verified that it corresponds to the final calcite dissolution rate of $k = 3 \times 10^{-10}$, i.e. the same value as in the other numerical calculations. This also suggests that the rate of calcite dissolution declines drastically, by three orders of magnitude, throughout the experiment. Additionally, an observed shift between the experimental and simulated curves is probably due to the fact that the experimental results of Madland et al. (2011) we plotted starting from the time when the concentration front approached the sample's outlet, rather than from the actual start of the experiment.

7. Fig. 4.11b: when a MgCl_2 solution was used as the injection fluid, the sum of effluent Ca^{2+} and Mg^{2+} equalled the initial concentration of Mg^{2+} because of the concomitant magnesite precipitation and calcite dissolution. When seawater is used as the injection fluid this is not the case anymore because the additional loss of Ca^{2+} due to anhydrite precipitation takes place. An experimental occlusion of the pore space was reported for this experiment. In our numerical model with 40 cells each cell had a pore volume of 0.82 ml. With the density of anhydrite being 2.97 g/ml and its molecular weight being 136 g/mol, it requires about 0.018 moles of anhydrite to occupy the whole volume of a single cell and thus prevent the fluid flow. However, only 2.7×10^{-5} moles or 0.15% of that amount was actually precipitated during the numerical simulation. Although precipitation does not occur simultaneously in all pores and thus the average continuum-scale description of this phenomena is not appropriate, our results tentatively suggests that the sample's occlusion is unlikely to occur. On the other hand, the experimental results shown in Fig. 4.10 (red curve) were obtained at exactly the

same conditions but no occlusion was reported even after 4 days of continuous flooding of the sample.

The resulting values for adsorption equilibrium constants for Ca^{2+} and Mg^{2+} ions at the room temperature are less than what was reported by Pokrovsky and Schott (2002). This is consistent with the fact that the measurements of Pokrovsky and Schott (2002) were made using finely ground rocks with a much higher adsorbing surface area. Moreover, the measurements in that work were conducted at the atmospheric pressure, while the simulated experiments were performed at 10-20 bar. Therefore, we compare the values from Table 4.5 with the values reported by Hiorth et al. (2010a). These workers used a different set of surface reactions but they can be converted to the reactions employed in this thesis. The following conclusions can be drawn:

- Equilibrium constants for Ca^{2+} and Mg^{2+} adsorption for 23/130 °C obtained in this work are $10^{-4.2}/10^{-3.5}$ and $10^{-4.73}/10^{-2.8}$. Calculations of Hiorth et al. (2010a) give the same values for both of these constants, $10^{-3.2}/10^{-3.1}$. Their results are much closer to ours for the high temperature and differ stronger for the room temperature. This might mean that the adsorption is weaker at the room temperature in real experiments as opposed to thermodynamical derivations, maybe due to stronger solvation of ions at the room temperature.
- Equilibrium constants for SO_4^{2-} adsorption are $10^{14.15}/10^{15.5}$ in this work and $10^{15}/10^{12.54}$ in Hiorth et al. (2010a). The figures for the room temperature are relatively close, while it is not clear why the value of Hiorth et al. decreases with growing temperature, which is in contradiction with the experimental results of increasing retardation of the sulphate breakthrough curves with increasing temperature.

Comparing our values for kinetic rates with other published results is more complicated because authors usually publish results on specific rates, measured in $\text{mol}/(\text{cm}^2 \cdot \text{s})$, and our continuum-scale rates implicitly include the rock surface available for reactions, i.e. the total rates are measured M/s. Moreover, the reaction surface does not equal the available rock surface, but is rather a surface of the mineral crystals in contact with water, which, for instance, is much smaller than the rock surface when a new mineral is precipitated within the pore space. Therefore, it is only

possible to compare the rates if they were measured in real porous rocks with an estimated value of the reaction surface. Hence, the following indirect comparisons with other published results were made:

- No published results on magnesite precipitation in real porous rocks were found. A precipitation rate for anhydrite at 123 °C in a sandstone core was reported by Wagner et al. (2005) with the value of 2.2×10^{-9} M/s, compared to our estimated rate of 3×10^{-11} M/s. A significant difference can be attributed, among other things, to the co-precipitation of magnesite, which can compete with anhydrite's precipitation.
- Calcite dissolution rates are usually studied in the context of real seawater systems and hence results for elevated temperatures are not presented in the literature. Calcite dissolution rate at the room temperature is approximately 10^{-11} mol/(cm²·s) (Plummer et al., 1978) and a specific surface for calcite rocks is approximately 1 – 100 cm²/l (Appelo, 2005). This yields a total rate of $10^{-11} - 10^{-9}$ M/s, which covers our value of about 10^{-10} M/s.

Perhaps the most puzzling result of our numerical modelling is the fact that a temperature increase of more than 100 °C resulted in at most tenfold increase in the calcite dissolution rate. As indicated above, dependency of an (initially much higher) rate on the amount of precipitated magnesite can explain certain experimental results but it is not clear why the same dependency is not applicable to the models corresponding to other experiments.

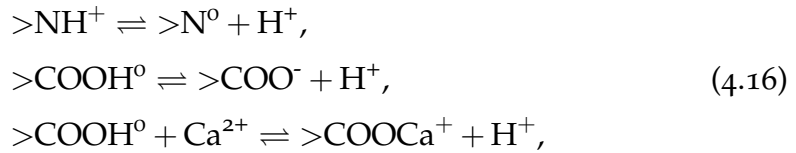
Another key question is the choice of mineral phases. Results of this section, namely Fig. 4.11, suggest that the choice of MgCO₃ was correct because its presence allowed us to reproduce the experimentally measured equal amounts of calcium loss and magnesium production. It is however possible that other magnesium-bearing mineral phases, such as brucite (Mg(OH)₂) or huntite (CaMg₃(CO₃)₄), precipitate instead of or along with magnesite. This can be clarified by experimental studies, such as scanning electron microscopy or X-ray diffraction analysis.

Despite these issues, our results imply that the chemical interaction between seawater and a calcite rock occurs in the form of both ion adsorption and alteration of mineral phases. Therefore, when considering the possible chemical cause of wettability modification it is important to examine both phenomena.

4.4.3 Outlook for two-phase flow problems

It is possible to extend the reactive transport model to two-phase flows. This case is much more complex as one has to account for two additional interactions – the water-oil interaction and the oil-rock interaction. We consider it as a future work and in this section we will briefly describe one possible approach to this task. We closely follow the procedure presented by Brady and Krumhansl (2012), where a similar approach was suggested for sandstones.

The ionic composition of a brine influences the oil-brine interface. This can be described using the same surface complexation approach as with the rock-brine interaction. Namely, (Brady and Krumhansl, 2012) specify the following surface reactions



where $>\text{NH}^+$ and $>\text{COOH}^0$ represent the dangling nitrogen base and carboxylate groups located at the oil-water interface. By employing the surface complexation model, we can calculate the surface charge and the prevailing surface complexes at the oil-water interface alongside the same calculations performed for the rock-water interface. It is then possible to analyse the relative change in the oil-rock affinity by calculating the concentration of “electrostatic bridges”, i.e. paired oppositely charged species from both interfaces. The key question of this stage is which of all possible bridges actually define a wettability state. For chalk, as proposed by Zhang et al. (2007), these are bonds between the $>\text{COO}^-$ groups on the oil interface and the positively charged components of chalk, i.e. $>\text{CaOH}^+$. Figure demonstrates the dependence of the concentration of this particular type of bridge on the concentration of SO_4^{2-} in seawater for a range of pH between 4 and 8. The brine compositions correspond to those reported by Strand et al. (2006), i.e. seawater with no sulphate, with an average seawater concentration of SO_4^{2-} , and with three times the average concentration. The concentration of bridges is plotted as a product of surface species that form it, which corresponds to a first-order equilibrium reaction $\text{A} + \text{B} \rightleftharpoons \text{C}$.

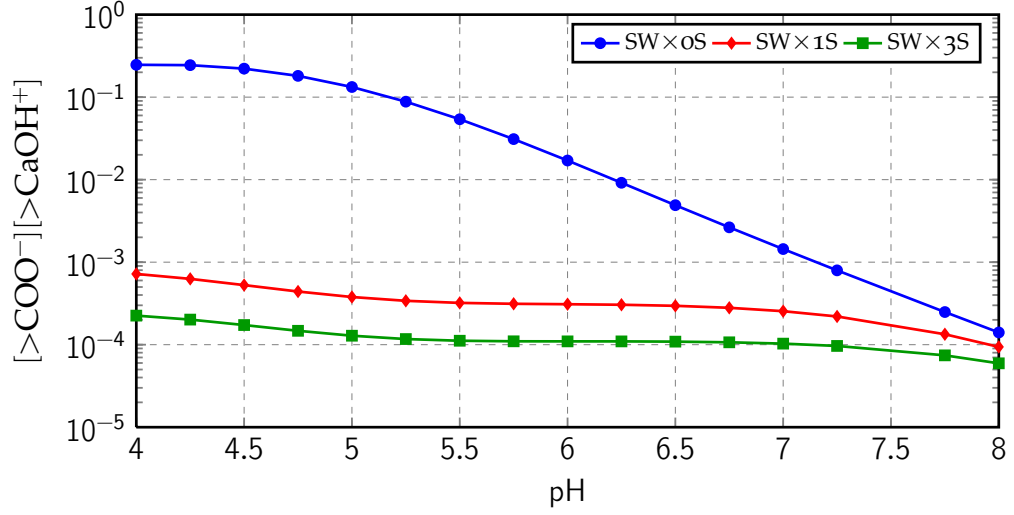


Figure 4.12: Simulated dependency of the electrostatic interaction between oil and rock, measured as $[>\text{COO}^-][>\text{CaOH}^+]$ product, on the sulphate concentration in seawater at different values of pH. $\text{sw} \times s$ denotes a multiple of an average seawater concentration of SO_4^{2-} .

It can be seen that increasing the sulphate concentration indeed reduces the $[>\text{COO}^-][>\text{CaOH}^+]$ product. However, the same model still cannot explain why the oil recovery increased in the experiments of Yousef et al. (2010) with the injection of progressively diluted seawater, as it predicts a higher $[>\text{COO}^-][>\text{CaOH}^+]$ product when seawater is mixed with distilled water. It means that the physical wettability state cannot be described only by the formation of the bonds of this type. While this remains a question for future work, we note that the described surface complexation models can be readily incorporated in our pore-scale flow simulator based on the unstructured FE - FV method because of its separate treatment of the elements that comprise grain and oil surfaces.

4.5 SUMMARY

In this chapter we presented a 1D numerical model for the continuum-scale simulation of the transport of seawater-like brines through chalk cores. It accounts for aqueous chemistry, surface adsorption and kinetic dissolution and precipitation of mineral phases. The model was implemented using the PHREEQC software.

We reviewed available experimental data on the chemical interaction between seawater and chalk cores and used our model to reproduce

the experimental findings. To achieve this, several parameters of the model were set as the degrees of freedom: equilibrium constants for the adsorption of Ca^{2+} , Mg^{2+} and SO_4^{2-} ions and rates of dissolution and precipitation of the included mineral phases (CaCO_3 , MgCO_3 , CaSO_4). The model successfully reproduced the experimental measurements with a very small variation of these parameters between different experiments. The main conclusions that we draw from this work are as follows

1. At low temperature the breakthrough curves are affected by the adsorption of SO_4^{2-} , Ca^{2+} and Mg^{2+} onto the chalk surface; seawater is in equilibrium with the rock and no change in mineral phases occurs.
2. At high temperature seawater becomes supersaturated with respect to magnesite and anhydrite and these phases precipitate during the coreflooding process. The precipitation of MgCO_3 and CaSO_4 reduces the aqueous concentrations of CO_3^{2-} and Ca^{2+} ions which causes the dissolution of CaCO_3 . Ionic adsorption also takes place at high temperatures.
3. The relative affinity of Ca^{2+} and Mg^{2+} towards the calcite surface changes with temperature: calcium is more readily adsorbed at room temperature and magnesium – at elevated temperature. This results in the substitution of Mg^{2+} for Ca^{2+} at the rock surface at high temperature.
4. Experimental breakthrough curves cannot be reproduced without considering the mineral dissolution and precipitation as kinetic processes. This implies that the interaction between seawater and a chalk rock depends of the fluid injection rate. Therefore the relevant results that are true for spontaneous imbibition of seawater into chalk samples cannot be directly extrapolated to the experiments that involve the forced fluid injection.
5. The mechanism of magnesite precipitation changes with respect to the fluid injection rate: at low rates it is dominated by the magnesite transport and at high rates – by the crystal growth.
6. The calcite surface area that determines the rate of calcite dissolution seems to be much less in the coreflooding experiments when compared to the experiments on crushed rocks. We explain this

result as a consequence of magnesite precipitation over the calcite surface.

7. Finally, it is rather instructional that even such intuitively simple experiments, involving a single homogeneous rock type and a single-phase brine of known ionic composition are still poorly constrained and are non-trivial to simulate numerically. This highlights a major hurdle in simulating the diagenesis of the geological systems which are described with a much higher level of uncertainty than a set of simple laboratory experiments presented in this chapter.

We suggest that both adsorption and mineral dissolution and precipitation would occur during the two-phase reactive transport. At this stage we can only speculate on their specific impact on oil recovery. In doing so, it is important to mention the result of Standnes and Austad (2000a), which showed that chalk samples that were fully saturated with oil (i.e. no connate water) could resist water imbibition after aging only when the oil was characterized by an acid number (AN) of more than 1.73 mg KOH/g. Also, ANs below this value still reduced the rate of imbibition as compared to the AN of zero. This implies that the wettability of chalk is related to this particular characteristic of crude oil. It is therefore possible that the wettability states of rocks used in two-phase experiments, reviewed in Chapter 1, were very different. Tables 1.1-1.3 reveal a tenfold reduction in AN between crude oils used by Fathi et al. (2010); Strand et al. (2006); Zhang et al. (2007) and by Gupta et al. (2011); Yousef et al. (2010). Importantly, all experiments with high AN manifest an increase in oil recovery with increasing concentration of divalent ions, while experiments with low AN demonstrate the improvement when their concentration is reduced. In addition to that, high AN experiments are also characterized by slow flow rates, i.e. either being spontaneous imbibition experiments or coreflood experiments flooded at a rate of 1 PV/day. Experiments of Gupta et al. (2011); Yousef et al. (2010) were conducted at a flow rate of about 10 PV/day. In this chapter we saw that it is important to consider mineral dissolution and precipitation as kinetic processes.

Therefore, based on the indirect evidence we hypothesize that in the experiments described by Fathi et al. (2010); Strand et al. (2006); Zhang et al. (2007) the affinity of oil to the rock was high and the oil recovery was affected by calcite dissolution; in the experiments reported by Gupta et al. (2011); Yousef et al. (2010) core samples were less oil-wet and the

flow rate was high, hence the recovery improvement was due to surface charge alteration. The experimental procedures to confirm or refute this hypothesis are clear: for crude oils with low AN the recovery should be observed with both high (as a result of surface charge alteration) and low (due to calcite dissolution) flow rates, so for high rates the recovery should improve with seawater dilution (as reported by Yousef et al. (2010)) and have lower sensitivity to temperature, while for low rates it should improve with the increase of SO_4^{2-} , Ca^{2+} and Mg^{2+} levels and have higher sensitivity to temperature; for crude oils with high AN the recovery should be observed only at slow flow rates and increased levels of SO_4^{2-} , Ca^{2+} and Mg^{2+} and manifest a high sensitivity to temperature changes.

SUMMARY, CONCLUSIONS AND FUTURE WORK

5.1 SUMMARY AND CONCLUSIONS

Understanding what controls the enhanced oil recovery during waterflooding of carbonate rocks is essential as the majority of the world's remaining hydrocarbon reserves are contained in carbonate rocks. To further this understanding, in this work we addressed the problem of the numerical pore-scale investigation of the mechanisms that facilitate the oil release from carbonate rocks during waterflooding. This problem involves three components – (1) reactive solute transport, (2) two-phase fluid flow, (3) chemical reaction between three (two fluids and one solid) phases. To this date, no work has been published that demonstrates the successful combination of all three components of this programme. The main complications include the computational limitations, i.e. both limitations of hardware speed and deficiencies of utilized algorithms, and incomplete understanding of physics and chemistry behind the relevant EOR processes themselves. In this thesis, we attempted to address these issues with respect to carbonate rocks. More specifically,

- In Chapter 2 we presented *a direct pore-scale procedure for modelling the single-phase fluid flow and transport in reconstructed 3D porous medium*. Our implementation of the pore-scale simulation includes (1) a FE solution of the stationary Stokes equation on unstructured meshes for an accurate representation of domain geometry; (2) an AMG method for solving the resulting FE linear problem, which offers a linear number-of-operations scalability with respect to mesh refinement and hence significantly mitigates the computer resources limitation factor; (3) an optional domain decomposition for problem parallelization. Therefore, the main novelty of this approach is the implementation of numerical methods that are best capable of tackling and making some progress with the complex problem described above. By utilizing an unstructured mesher that works directly on the CT data, stable first-order discretization schemes for

the governing PDEs and a state-of-the-art algebraic multigrid solver, we for the first time bring the problem of direct pore-scale fluid flow within the reach of research groups that do not have access to computer clusters with hundreds of computing nodes. By applying this procedure to a reconstructed Fontainebleau sandstone sample we were able to demonstrate that the FE solution yields the same permeability value as the LB method while requiring a fraction of time necessary for the LB solution to converge. We also highlighted the detrimental effect of reducing the amount of geometrical data by means of excessive domain boundary smoothing. This implies that given an accurate mesh of a domain it is much more preferable to use the FE-based method of calculating the resulting permeability than the currently more wide-spread LB approach.

- In Chapter 2 we then presented *a method for solving the transient problem of the pore-scale inert solute transport*. For its implementation we employed a combined FE-FV technique. Transport modelling in Chapter 2 demonstrated the correct transition between various flow regimes from diffusion- to convection-dominated and gave quantitatively similar results when upscaled sample dispersivity was compared to other published results. It also showed a slight decrease in the sample dispersivity as well as in the relative contribution of diffusion in the mixed flow regime in the case of a mesh with inflated pore throats. Finally, we observed that a mesh reconstruction procedure determines the onset of the breakthrough curves tailing with respect to the Peclet number.
- In Chapter 3 we presented *a computational method for the direct pore-scale simulation of the reactive solute transport*. The method extends the tools of the previous chapter, with the chemical reactions being decoupled from the transport calculations which allows us to link any stand-alone chemical solver to our simulator. We applied the procedure to a reconstructed Fontainebleau sandstone sample and showed the retardation behavior of the averaged breakthrough curves in the presence of the solute adsorption on the grain walls.
- We then showed *the method for simulating the presence of the second immiscibly trapped fluid phase based on calculating the distance map of the pore space*. We demonstrated how it can be combined together with

the solute transport computation to model the possible mechanism for the enhanced model recovery when part of the pore space is occupied by a second immiscibly trapped fluid phase. We showed that even in such a simple model the interaction between the transport and the chemical reactions is non-trivial, i.e. the competition between diffusion and adsorption can prevent the solute from being dispatched to the oil/water/rock contact line. In reality the affinity of an ion towards the surface is influenced among other things by the surface charge which in turn depends on the ionic composition of the brine. This may be one of the reasons for the sensitivity of the oil recovery to the ionic composition of the brine.

The major advantage of using the FE-FV method for the fluid flow simulations is its capability to simulate the transport phenomena along the 2D surfaces within a 3D domain. Due to this capability it is possible to formally include the micron-scale water films at the rock surface without modifying the mesh itself, as well as to model the solute diffusion along the oil-water or oil-rock interfaces, which are suggested to be the crucial mechanisms for dispatching the wettability altering agents to the oil-rock interface (Hammond and Unsal, 2009). We see this as a compelling reason to choose the FE-FV method over other alternatives to simulate the pore-scale reactive transport phenomena relevant to wettability alteration.

The tools that we presented in Chapters 2 and 3 essentially laid the groundwork for the simulation of the pore-scale propagation of the reactive solutes and their chemical interaction with both the oil phase and the rock.

- In Chapter 4 *we considered a specific seawater/chalk system and identified what chemical interactions can be inferred from the published experimental studies of this particular combination of the porous medium and the injected fluid.* To this end, we presented a 1D numerical model for the continuum-scale simulation of the transport of seawater-like brines through chalk cores. It accounts for aqueous chemistry, surface adsorption and kinetic dissolution and precipitation of mineral phases. The model was implemented using the PHREEQC software. We reviewed available experimental data on the chemical interaction between seawater and chalk cores in Chapter 4 and used our model to reproduce the experimental findings. To achieve this, several parameters of the model were set as the degrees of freedom: equilib-

rium constants for the adsorption of Ca^{2+} , Mg^{2+} and SO_4^{2-} ions and rates of dissolution and precipitation of the included mineral phases (CaCO_3 , MgCO_3 , CaSO_4). The model successfully reproduced the experimental measurements with a very small variation of these parameters between different experiments. We concluded that these measurements can be explained by a combination of the adsorption of ions onto the rock surface and the dissolution and precipitation of mineral phases. Based on the indirect evidence, we suggested how these results can be extrapolated to the two-phase spontaneous imbibition and forced injection experiments to explain the observed trends.

Although the dependency of the upscaled two-phase flow properties on the reactive transport was not analysed in the present work, certain conclusion about the link between our results and the large-scale reservoir simulations can still drawn. Presently all attempts to simulate the enhanced oil recovery mechanisms at the field scale in either sandstones or carbonates resort to linking the capillary pressure and/or relative permeability curves to a single abstract solute concentration in the bulk or the amount of solute adsorbed at the rock surface. As evident from the results of Chapter 4, both bulk and surface concentration levels of all participating ions are products of a complex chemical interplay that depends on the initial concentrations, temperature and flow rate, and potentially the crude oil properties. It is, therefore, necessary to incorporate the effect of all these factors rather than a single salinity level. Moreover, it is important to acknowledge that the mechanism that facilitates the oil release during the spontaneous imbibition may be different from what liberates oil during the forced injection, i.e. rock dissolution vs. surface charge alteration. This should be reflected in modelling the EOR processes in fractured vs. non-fractured reservoirs.

5.2 FUTURE WORK

Obviously, the subject of enhanced oil recovery in carbonates is far from being fully studied. The directions in which this particular work can be extended include the following:

- Oil-water and oil-rock interactions or, more generally, a chemical theory of wettability of carbonate rocks. We have already mentioned at

the end of the previous chapter how a surface complexation model can be used to analyze the link between the brine composition and the concentration of surface species at the water-oil interface.

- Inclusion of all relevant chemical reactions into the pore-scale model. Our pore-scale simulator with a rule-based method for determining the oil occupancy does not account for an accurate flow of the oil phase, but it can be used to determine whether or in what cases the included chemical reactions lead to conditions, favourable for the enhanced oil recovery. Ideally, EOR phenomena should be described by the full two-phase transient Navier-Stokes equations together with the reactive solute transport.
- Considering that we have identified the dissolution and precipitation as the key chemical effects that occur during the injection of seawater into chalk rocks, an ideal pore-scale simulator should be able to account for the changes in the geometry of the pore space.
- An influence of the rock surface charge on the flow of charged ions can be incorporated in our model to simulate the electrokinetic flows. This can be done by recasting the advection-diffusion equation in the form of the Nernst-Planck equation, that accounts for the motion of ions subject to electric potential.
- A recent study by Jackson and Vinogradov (2012) showed a link between the wettability state of carbonate rocks and various electrokinetic parameters, such as the streaming potential coupling coefficient, zeta potential and transported excess of charge. A hypothesis based on the local variations of the surface charge due to the presence of sandwiched oil layers has been proposed by the authors to explain the observed results. The measurements were conducted at residual oil saturation, i.e. the oil phase was immobile. Hence, by using the PHREEQC software to calculate the surface charge and potential and by coupling it with the Stokes and Nernst-Planck equations, it will be possible to investigate the proposed hypothesis numerically.
- Ultimately, finite element pore-scale simulations should be used to pursue the second objective outlined in the introduction to this thesis, namely what is the link between the reactive transport in

carbonates and the upscaled characteristics of the two-phase flow through them, i.e. residual oil saturation, relative permeability and capillary pressure curves. It should be also used to highlight the difference in the enhanced recovery during the spontaneous imbibition and forced injection experiments, proposed at the end of the previous chapter. This will make it possible to use the pore-scale modelling results in the large-scale simulations, such as discrete fracture-matrix simulations where the fluid transport is modelled explicitly only through fractures and the exchange between fractures and the porous matrix is assumed to occur due to the spontaneous imbibition.

- It is important to experimentally investigate the influence of crude oil properties on the outcome of the wettability alteration in carbonates. This has largely been neglected in all the published experimental investigations. Suggestions for the possible experimental design were provided at the end of Chapter 4.

BIBLIOGRAPHY

- R. C. Acharya, M. I. J. Van Dijke, K. S. Sorbie, S. Van der Zee, and A. Leijnse. Quantification of longitudinal dispersion by upscaling Brownian motion of tracer displacement in a 3D pore-scale network model. *Advances in Water Resources*, 30(2):199–213, 2007.
- P. M. Adler, C. G. Jacquin, and J. Quiblier. Flow in simulated porous media. *International Journal of Multiphase Flow*, 16(4):691–712, 1990.
- L. T. Akanji and S. K. Matthäi. Finite element-based characterization of pore-scale geometry and its impact on fluid flow. *Transport in Porous Media*, 81(2):241–259, 2010.
- E. Aker, K. J. Måløy, and A. Hansen. Simulating temporal evolution of pressure in two-phase flow in porous media. *Physical Review E*, 58(2):2217–2226, 1998.
- A. Al-Dhahli, S. Geiger, and M. I. J. van Dijke. Three-phase pore-network modelling for mixed-wet carbonate reservoirs. SPE-147991. In *SPE Reservoir Characterization and Simulation Conference. Abu Dhabi, U.A.E. 9-11 October.*, 2011.
- L. Algive, S. Bekri, and O. Vizika. Pore-Network Modeling Dedicated to the Determination of the Petrophysical-Property Changes in the Presence of Reactive Fluid. *SPE Journal*, 15(3):618–633, 2010.
- C. A. J. Appelo. *Geochemistry, groundwater and pollution*. Taylor & Francis, 2005.
- T. Austad. Seawater in chalk: An EOR and compaction fluid. In *The 42nd US Rock Mechanics Symposium (USRMS)*, 2008.
- I. Babuška. Error-bounds for finite element method. *Numerische Mathematik*, 16(4):322–333, 1971.
- I. Barrodale and F. D. K. Roberts. Algorithm 552: Solution of the Constrained I_1 Linear Approximation Problem [F4]. *ACM Transactions on Mathematical Software (TOMS)*, 6(2):231–235, 1980.

- D. Bauer, S. Youssef, M. Fleury, S. Bekri, E. Rosenberg, and O. Vizika. Improving the Estimations of Petrophysical Transport Behavior of Carbonate Rocks Using a Dual Pore Network Approach Combined with Computed Microtomography. *Transport in Porous Media*, pages 1–20, 2012.
- P. Bénézech, G. D. Saldi, J.-L. Dandurand, and J. Schott. Experimental determination of the solubility product of magnesite at 50 to 200 °C. *Chemical Geology*, 286(1–2):21–31, 2011.
- B. Bijeljic, A. H. Muggeridge, and M. J. Blunt. Pore-scale modeling of longitudinal dispersion. *Water Resources Research*, 40(11):W11501, 2004.
- M. J. Blunt. Flow in porous media – pore-network models and multiphase flow. *Current Opinion in Colloid & Interface Science*, 6(3):197–207, 2001.
- P. V. Brady and J. L. Krumhansl. A surface complexation model of oil–brine–sandstone interfaces at 100 °C: Low salinity waterflooding. *Journal of Petroleum Science and Engineering*, 81:171–176, 2012.
- A. Brandt, S. F. McCormick, and J. W. Ruge. Algebraic multigrid (AMG) for automatic multigrid solutions with application to geodetic computations. *Report. Institute for Computational Studies, Fort Collins, Colorado*, 1982.
- H. Brenner. Dispersion Resulting from Flow through Spatially Periodic Porous Media. *Philosophical Transactions of the Royal Society of London. Series A, Mathematical and Physical Sciences*, 297(1430):81–133, 1980.
- F. Brezzi. On the existence, uniqueness and approximation of saddle-point problems arising from Lagrangian multipliers. *RAIRO Anal. Numer*, 8(2):129–151, 1974.
- M. B. Cardenas. Three-dimensional vortices in single pores and their effects on transport. *Geophysical Research Letters*, 35(18):L18402, 2008.
- M. B. Cardenas. Direct simulation of pore level Fickian dispersion scale for transport through dense cubic packed spheres with vortices. *Geochemistry Geophysics Geosystems*, 10(12):Q12014, 2009.
- P. C. Carman. Fluid flow through granular beds. *Transactions-Institution of Chemical Engineers*, 15(2):150–166, 1937.

- P. C. Carman. *Flow of gases through porous media*. Butterworths Scientific Publications, 1956.
- M. A. Celia, P. C. Reeves, and L. A. Ferrand. Recent advances in pore scale models for multiphase flow in prous media. *Reviews of Geophysics*, 33:1049–1058, 1995.
- Scott R. Charlton and David L. Parkhurst. Modules based on the geochemical model PHREEQC for use in scripting and programming languages. *Computers & Geosciences*, 2011. In Press, Corrected Proof.
- S. Chen and G. D. Doolen. Lattice Boltzmann method for fluid flows. *Annual Review of Fluid Mechanics*, 30(1):329–364, 1998.
- J. M. Chern and Y. W. Chien. Competitive adsorption of benzoic acid and p-nitrophenol onto activated carbon: isotherm and breakthrough curves. *Water Research*, 37(10):2347–2356, 2003. ISSN 0043-1354.
- R. Codina. On stabilized finite element methods for linear systems of convection-diffusion-reaction equations. *Computer Methods in Applied Mechanics and Engineering*, 188(1-3):61–82, 2000.
- S. D. Cohen and A. C. Hindmarsh. CVODE, a stiff/nonstiff ODE solver in C. *Computers in physics*, 10(2):138–143, 1996.
- R. E. Collins and C. E. Cooke. Fundamental basis for the contact angle and capillary pressure. *Transactions of the Faraday Society*, 55:1602–1606, 1959.
- D. Coumou, S. K. Matthäi, S. Geiger, and T. Driesner. A parallel FE–FV scheme to solve fluid flow in complex geologic media. *Computers and Geosciences*, 34(12):1697–1707, 2008.
- D. d’Humières. Generalized Lattice-Boltzmann Equations. *Rarefied Gas Dynamics – Theory and Simulations*, 159:450–458, 1994.
- J. Donea and A. Huerta. *Finite element methods for flow problems*. John Wiley & Sons Inc, 2003.
- J. H. Dunsmuir, S. R. Ferguson, K. L. D’Amico, and J. P. Stokes. X-ray microtomography: a new tool for the characterization of porous media. SPE-22860. In *SPE Annual Technical Conference and Exhibition*, 1991.

- S. Durucan and J. Q. Shi. Improving the CO₂ well injectivity and enhanced coalbed methane production performance in coal seams. *International Journal of Coal Geology*, 77(1-2):214–221, 2009. ISSN 0166-5162.
- D. A. Dzombak and F. Morel. *Surface complexation modeling: Hydrous ferric oxide*. Wiley-Interscience, 1990.
- A. J. Ellis. The solubility of calcite in carbon dioxide solutions. *American Journal of Science*, 257(5):354, 1959.
- S. Evje and A. Hiorth. A mathematical model for dynamic wettability alteration controlled by water-rock chemistry. *Networks and Heterogeneous Media*, 5(2):217–256, 2010.
- S. Evje, A. Hiorth, M. V. Madland, and R. I. Korsnes. A mathematical model relevant for weakening of chalk reservoirs due to chemical reactions. *Networks and Heterogeneous Media*, 4(4):755–788, 2009.
- E. Fares and W. Schröder. A differential equation for approximate wall distance. *International journal for numerical methods in fluids*, 39(8):743–762, 2002.
- S. J. Fathi, T. Austad, and S. Strand. "Smart Water" as a Wettability Modifier in Chalk: The Effect of Salinity and Ionic Composition. *Energy & Fuels*, 24(4):2514–2519, 2010.
- W. Fourie, R. Said, P. Young, and D. L. Barnes. The simulation of pore-scale fluid flow with real world geometries obtained from X-ray computed tomography. In *Proceedings of the COMSOL Conference*, 2007.
- J. J. Fried and M. A. Combarous. Dispersion in porous media. *Advances in Hydroscience*, 7:169–282, 1971.
- G. Garmeh, R. Johns, and L. Lake. Pore-scale simulation of dispersion in porous media. *SPE Journal*, 14(4):559–567, 2009.
- S. Geiger, S. Roberts, S. K. Matthäi, C. Zoppou, and A. Burri. Combining finite element and finite volume methods for efficient multiphase flow simulations in highly heterogeneous and structurally complex geologic media. *Geofluids*, 4(4):284–299, 2004.
- L. W. Gelhar, C. Welty, and K. R. Rehfeldt. A critical review of data on field-scale dispersion in aquifers. *Water resources research*, 28(7):1955–1974, 1992.

- O. Gerbaux, F. Buyens, V. V. Mourzenko, A. Mempoiteil, A. Vabre, J. F. Thovert, and P. M. Adler. Transport properties of real metallic foams. *Journal of colloid and interface science*, 2009.
- G. A. Gist, A. H. Thompson, A. J. Katz, and R. L. Higgins. Hydrodynamic dispersion and pore geometry in consolidated rock. *Physics of Fluids A: Fluid Dynamics*, 2:1533, 1990.
- S. K. Godunov. A difference method for numerical calculation of discontinuous solutions of the equations of hydrodynamics. *Matematicheskii Sbornik*, 89(3):271–306, 1959.
- W. Gropp, E. Lusk, N. Doss, and A. Skjellum. A high-performance, portable implementation of the MPI message passing interface standard. *Parallel Computing*, 22(6):789–828, 1996.
- R. Gupta, G. Smith, L. Hu, T. Willingham, M. Lo Cascio, J. Shyeh, and C. Harris. Enhanced Waterflood for Carbonate Reservoirs-Impact of Injection Water Composition. SPE-142668. In *SPE Middle East Oil and Gas Show and Conference*, 2011.
- T. Haarberg, I. Selm, D. B. Granbakken, T. Østvold, P. Read, and T. Schmidt. Scale formation in reservoir and production equipment during oil recovery: An equilibrium model. *SPE Production Engineering*, 7(1):75–84, 1992.
- R. Haggerty and S. M. Gorelick. Multiple-rate mass transfer for modeling diffusion and surface reactions in media with pore-scale heterogeneity. *Water Resources Research*, 31(10):2383–2400, 1995.
- P. S. Hammond and E. Unsal. Spontaneous and forced imbibition of aqueous wettability altering surfactant solution into an initially oil-wet capillary. *Langmuir*, 25(21):12591–12603, 2009.
- P. S. Hammond and E. Unsal. A Dynamic Pore Network Model for Oil Displacement by Wettability-Altering Surfactant Solution. *Transport in Porous Media*, pages 1–29, 2012.
- J. Happel and H. Brenner. *Low Reynolds number hydrodynamics: with special applications to particulate media*. Springer, 1983.

- J. G. Heywood, R. Rannacher, and S. Turek. Artificial boundaries and flux and pressure conditions for the incompressible Navier-Stokes equations. *International Journal for Numerical Methods in Fluids*, 22(5): 325–352, 1996.
- P. C. Hiemenz and R. Rajagopalan. *Principles of colloid and surface chemistry*, volume 14. CRC, 1997.
- A. Hiorth, L. M. Cathles, and M. V. Madland. The Impact of Pore Water Chemistry on Carbonate Surface Charge and Oil Wettability. *Transport in Porous Media*, 85(1):1–21, 2010a.
- A. Hiorth, E. Jøttestuen, L. M. Cathles, R. I. Korsnes, and M. V. Madland. A fully Coupled Geochemical Model with a Pore Scale Lattice Boltzmann Simulator-Principles and First Results. SCA, 2010b.
- C. W. Hirt and B. D. Nichols. Volume of fluid (VOF) method for the dynamics of free boundaries. *Journal of computational physics*, 39(1): 201–225, 1981.
- P. J. Hoogerbrugge and J. Koelman. Simulating microscopic hydrodynamic phenomena with dissipative particle dynamics. *EPL (Europhysics Letters)*, 19:155, 1992.
- T. J. R. Hughes and L. P. Franca. A new finite element formulation for computational fluid dynamics. VII: The Stokes problem with various well posed boundary conditions: symmetric formulations that converge for all velocity, pressure spaces. *Computer Methods in Applied Mechanics and Engineering*, 65(1):85–96, 1987.
- N. A. Idowu and M. J. Blunt. Pore-Scale Modelling of Rate Effects in Waterflooding. *Transport in porous media*, 83(1):151–169, 2010.
- J. N. Israelachvili. *Intermolecular and Surface Forces: Revised Third Edition*. Academic press, 2011.
- J. Istok. *Groundwater modeling by the finite element method*. American Geophysical Union, 1989.
- M. D. Jackson and J. Vinogradov. Impact of wettability on laboratory measurements of streaming potential in carbonates. *Colloids and Surfaces A: Physicochemical and Engineering Aspects*, 393:86–95, 2012.

- D. Jacqmin. Calculation of two-phase Navier-Stokes flows using phase-field modeling. *Journal of Computational Physics*, 155(1):96–127, 1999.
- Z. Jiang. *Quantitative characterisation of the geometry and topology of pore space in 3D rock images*. PhD thesis, Heriot-Watt University, 2008.
- V. Joekar-Niasar, S. M. Hassanizadeh, and H. K. Dahle. Non-equilibrium effects in capillarity and interfacial area in two-phase flow: dynamic pore-network modelling. *Journal of Fluid Mechanics*, 655(1):38–71, 2010a.
- V. Joekar-Niasar, M. Prodanovic, D. Wildenschild, and S. M. Hassanizadeh. Network model investigation of interfacial area, capillary pressure and saturation relationships in granular porous media. *Water Resources Research*, 46(6):W06526, 2010b.
- B. Kaasa. *Prediction of pH, mineral precipitation and multiphase equilibria during oil recovery*. PhD thesis, Norwegian University of Science and Technology, 1998.
- Q. Kang, D. Zhang, and S. Chen. Unified lattice Boltzmann method for flow in multiscale porous media. *Physical Review E*, 66(5):056307, 2002.
- Q. Kang, P. C. Lichtner, and D. Zhang. Lattice Boltzmann pore-scale model for multicomponent reactive transport in porous media. *Journal of geophysical research*, 111(B5):B05203, 2006.
- Q. Kang, P. C. Lichtner, H. S. Viswanathan, and A. I. Abdel-Fattah. Pore scale modeling of reactive transport involved in geologic CO₂ sequestration. *Transport in porous media*, 82(1):197–213, 2010.
- O. Karoussi and A. A. Hamouda. Imbibition of sulfate and magnesium ions into carbonate rocks at elevated temperatures and their influence on wettability alteration and oil recovery. *Energy & fuels*, 21(4):2138–2146, 2007.
- G. Karypis and V. Kumar. MeTiS—A Software Package for Partitioning Unstructured Graphs, Partitioning Meshes, and Computing Fill-Reducing Orderings of Sparse Matrices—Version 4.0. *University of Minnesota*, 102, 1998.
- D. L. Kinzel and G. A. Hill. Experimental study of dispersion in a consolidated sandstone. *The Canadian Journal of Chemical Engineering*, 67(1):39–44, 1989.

- M. A. Knackstedt, A. P. Sheppard, and M. Sahimi. Pore network modelling of two-phase flow in porous rock: the effect of correlated heterogeneity. *Advances in Water Resources*, 24(3-4):257–277, 2001.
- S. Koshizuka, H. Tamako, and Y. Oka. A particle method for incompressible viscous flow with fluid fragmentation. *Computational Fluid Dynamics Journal*, 4(1):29–46, 1995.
- J. Kozeny. Ueber kapillare leitung des wassers im boden. *Wien, Akad. Wiss*, 136(2a):271, 1927.
- A. Krechel and K. Stüben. Parallel algebraic multigrid based on subdomain blocking. *Parallel Computing*, 27(8):1009–1031, 2001.
- D. Kulik, U. Berner, and E. Curti. Modelling chemical equilibrium partitioning with the GEMS-PSI code. *PSI Scientific Report*, 4:109–122, 2003.
- A. Kuzmin and A. A. Mohamad. Multirange multi-relaxation time Shan-Chen model with extended equilibrium. *Computers & Mathematics with Applications*, 59(7):2260–2270, 2010.
- A. Kuzmin, A. A. Mohamad, and S. Succi. Multi-relaxation time Lattice Boltzmann Model for multiphase flows. *International Journal of Modern Physics C*, 19(6):875–902, 2008.
- O. A. Ladyzhenskaya. The mathematical theory of viscous incompressible flow. *Gordon and Breach Science, New York*, 1969.
- A. Lager, K. J. Webb, C. J. J. Black, M. Singleton, and K. S. Sorbie. Low salinity oil recovery-an experimental investigation. *Petrophysics*, 49(1):28, 2008.
- L. W. Lake. *Enhanced oil recovery*. Prentice Hall, 1989.
- C. J. Landry, Z. T. Karpyn, and M. Piri. Pore-scale analysis of trapped immiscible fluid structures and fluid interfacial areas in oil-wet and water-wet bead packs. *Geofluids*, 11(2):209–227, 2011.
- L. Li, C. A. Peters, and M. A. Celia. Upscaling geochemical reaction rates using pore-scale network modeling. *Advances in Water Resources*, 29(9):1351–1370, 2006.

- O. Lopez, A. Mock, J. Skretting, E.B. Petersen Jr, P.E. Øren, and A.B. Rustad. Investigation into the reliability of predictive pore-scale modeling for siliciclastic reservoir rocks. In *paper SCA2010-41 presented at the 2010 SCA International Symposium, Halifax*, pages 4–7, 2010.
- W. E. Lorensen and H. E. Cline. Marching cubes: A high resolution 3D surface construction algorithm. page 169, 1987.
- L. B. Lucy. A numerical approach to the testing of the fission hypothesis. *The Astronomical Journal*, 82:1013–1024, 1977.
- J. Ma, K. Wu, Z. Jiang, and G. D. Couples. SHIFT: An implementation for lattice Boltzmann simulation in low-porosity porous media. *Physical Review E*, 81(5):56702, 2010.
- M. V. Madland, A. Hiorth, E. Omdal, M. Megawati, T. Hildebrand-Habel, R. I. Korsnes, S. Evje, and L. M. Cathles. Chemical Alterations Induced by Rock–Fluid Interactions When Injecting Brines in High Porosity Chalks. *Transport in porous media*, pages 1–24, 2011.
- I. Malinouskaya, V. V. Mourzenko, J. F. Thovert, and P. M. Adler. Wave propagation through saturated porous media. *Physical Review E*, 77(6):66302, 2008.
- E. Manrique, M. Gurfinkel, and V. Muci. Enhanced Oil Recovery Field Experiences in Carbonate Reservoirs in the United States. In *25th Annual Workshop and Symposium*, 2004.
- S. K. Matthäi, S. Geiger, S. G. Roberts, A. Paluszny, M. Belayneh, A. Burri, A. Mezentsev, H. Lu, D. Coumou, T. Driesner, et al. Numerical simulation of multi-phase fluid flow in structurally complex reservoirs. *Geological Society London Special Publications*, 292(1):405, 2007.
- M. Matyka, A. Khalili, and Z. Koza. Tortuosity-porosity relation in porous media flow. *Physical Review E*, 78(2):26306, 2008.
- P. Meakin and A. M. Tartakovsky. Modeling and simulation of pore-scale multiphase fluid flow and reactive transport in fractured and porous media. *Reviews of Geophysics*, 47(3):RG3002, 2009.
- P. Mostaghimi, B. Bijeljic, and M. Blunt. Simulation of Flow and Dispersion on Pore-Space Images. SPE-135261. In *SPE Annual Technical Conference and Exhibition*, 2010.

- C. Nardi, O. Lopez, P. E. Øren, R. Held, and E. B. Petersen Jr. Pore-scale modeling of three-phase flow: Comparative study with experimental reservoir data. In *Paper SCI2009-30 presented at the International Symposium of the Society of Core Analysts, Noordwijk, The Netherlands*, pages 27–30, 2009.
- G. A. Narsilio, O. Buzzi, S. Fityus, T. S. Yun, and D. W. Smith. Upscaling of Navier–Stokes equations in porous media: Theoretical, numerical and experimental approach. *Computers and Geotechnics*, 36(7):1200–1206, 2009.
- A. Narváez, T. Zauner, F. Raischel, R. Hilfer, and J. Harting. Quantitative analysis of numerical estimates for the permeability of porous media from lattice-Boltzmann simulations. *Journal of Statistical Mechanics: Theory and Experiment*, 2010:P11026, 2010.
- J. M. Nordbotten, M. A. Celia, H. K. Dahle, and S. M. Hassanizadeh. Interpretation of macroscale variables in Darcy’s law. *Water Resources Research*, 43(8):Wo8430, 2007.
- A. Ogata and R. B. Banks. A solution of the differential equation of longitudinal dispersion in porous media. Prof. Paper 411-A. *US Geological Survey, US Government Printing Office, Washington, DC*, 1962.
- H. Okabe and M. J. Blunt. Prediction of permeability for porous media reconstructed using multiple-point statistics. *Physical Review E*, 70(6):66135, 2004.
- P. E. Øren and S. Bakke. Process based reconstruction of sandstones and prediction of transport properties. *Transport in Porous Media*, 46(2):311–343, 2002.
- S. Ovaysi and M. Piri. Pore-scale modeling of dispersion in disordered porous media. *Journal of Contaminant Hydrology*, 124(1-4):68–81, 2011.
- A. Paluszny, S. K. Matthai, and M. Hohmeyer. Hybrid finite element-finite volume discretization of complex geologic structures and a new simulation workflow demonstrated on fractured rocks. *Geofluids*, 7(2):1–23, 2007.
- C. Pan, L. S. Luo, and C. T. Miller. An evaluation of lattice Boltzmann schemes for porous medium flow simulation. *Computers and Fluids*, 35(8-9):898–909, 2006. On LB dependence on the relaxation parameter.

- A. Parmigiani, C. Huber, O. Bachmann, and B. Chopard. Pore-scale mass and reactant transport in multiphase porous media flows. *Journal of Fluid Mechanics*, 686(1):40–76, 2011.
- G. Peng, H. Xi, C. Duncan, and S. H. Chou. Lattice Boltzmann method on irregular meshes. *Physical Review E*, 58(4):4124–4127, 1998.
- L. N. Plummer and E. Busenberg. The solubilities of calcite, aragonite and vaterite in CO_2 - H_2O solutions between 0 and 90 °C, and an evaluation of the aqueous model for the system CaCO_3 - CO_2 - H_2O . *Geochimica et Cosmochimica Acta*, 46(6):1011–1040, 1982.
- L. N. Plummer, T. M. L. Wigley, and D.L. Parkhurst. The Kinetics of Calcite Dissolution in CO_2 -Water Systems at 5 to 60 °C and 0.0 to 1.0 ATM CO_2 . *American Journal of Science*, 278, 1978.
- O. S. Pokrovsky and J. Schott. Surface chemistry and dissolution kinetics of divalent metal carbonates. *Environmental science & technology*, 36(3):426–432, 2002.
- G. A. Pope. Cation Exchange in Chemical Flooding: Part 1 - Basic Theory Without Dispersion. *SPE*, 6771:418–434, 1978.
- M. Prodanovic and S. L. Bryant. A level set method for determining critical curvatures for drainage and imbibition. *Journal of colloid and interface science*, 304(2):442–458, 2006.
- T. Ramstad, N. Idowu, C. Nardi, and P. E. Øren. Relative Permeability Calculations from Two-Phase Flow Simulations Directly on Digital Images of Porous Rocks. *Transport in Porous Media*, pages 1–18, 2011.
- L. Rineau, S. Tayeb, and M. Yvinec. 3D Mesh Generation. In *CGAL User and Reference Manual*. CGAL Editorial Board, 2010. URL http://www.cgal.org/Manual/3.8/doc_html/cgal_manual/Mesh_3/Chapter_main.html.
- A. P. Roberts. Statistical reconstruction of three-dimensional porous media from two-dimensional images. *Physical Review E*, 56(3):3203–3212, 1997.
- A. V. Ryazanov, M. I. J. van Dijke, and K. Sorbie. Two-Phase Pore-Network Modelling: Existence of Oil Layers During Water Invasion. *Transport in Porous Media*, 80:79–99, 2009.

- M. Sahimi and M. R. Islam. *Flow and transport in porous media and fractured rock*. Wiley-VCH Verlag GmbH, 1995.
- G. D. Saldi, G. Jordan, J. Schott, and E. H. Oelkers. Magnesite growth rates as a function of temperature and saturation state. *Geochimica et Cosmochimica Acta*, 73(19):5646–5657, 2009.
- J. Salles, J. F. Thovert, R. Delannay, L. Prevors, J. L. Auriault, and P. M. Adler. Taylor dispersion in porous media. Determination of the dispersion tensor. *Physics of Fluids A: Fluid Dynamics*, 5:2348, 1993.
- Schlumberger. Carbonate Reservoirs, 2007.
- J. A. Sethian. *Level set methods and fast marching methods: evolving interfaces in computational geometry, fluid mechanics, computer vision, and materials science*. Number 3. Cambridge Univ Pr, 1999.
- X. Shan and H. Chen. Lattice Boltzmann model for simulating flows with multiple phases and components. *Physical Review E*, 47(3):1815, 1993.
- D. Silin and T. Patzek. Pore space morphology analysis using maximal inscribed spheres. *Physica A: Statistical and Theoretical Physics*, 371(2):336–360, 2006.
- K. Skagius and I. Neretnieks. Porosities and diffusivities of some non-sorbing species in crystalline rocks. *Water Resour. Res.*, 22(3):389–398, 1986.
- P. K. Smolarkiewicz and C. Larrabee Winter. Pores resolving simulation of Darcy flows. *Journal of Computational Physics*, 2010.
- K. Sorbie. A General Coupled Kinetic Adsorption/Precipitation Transport Model for Scale Inhibitor Retention in Porous Media: I. Model Formulation. SPE-130702. In *SPE International Conference on Oilfield Scale*, 2010.
- K. S. Sorbie and P. J. Clifford. Inclusion of molecular diffusion effects in the network modelling of hydrodynamic dispersion in porous media. *Chemical Engineering Science*, 46(10):2525–42, 1991.
- K. S. Sorbie and A. Skauge. Can Network Modelling Predict Two-Phase Flow Functions? In *International Symposium of the Society of Core Analysts*, 2011.

- K. S. Sorbie, A. Ryazanov, and M. I. J. van Dijke. The Structure of Residual Oil as a Function of Wettability Alteration using Pore-Scale Network Modelling. *SCA Paper A*, 64, 2011.
- P. Spanne, J. F. Thovert, C. J. Jacquin, W. B. Lindquist, K. W. Jones, and P. M. Adler. Synchrotron computed microtomography of porous media: topology and transports. *Physical Review Letters*, 73(14):2001–2004, 1994.
- D. C. Standnes and T. Austad. Wettability alteration in chalk:: 1. Preparation of core material and oil properties. *Journal of Petroleum Science and Engineering*, 28(3):111–121, 2000a.
- D. C. Standnes and T. Austad. Wettability alteration in chalk:: 2. Mechanism for wettability alteration from oil-wet to water-wet using surfactants. *Journal of Petroleum Science and Engineering*, 28(3):123–143, 2000b.
- C. I. Steefel and A. C. Lasaga. A coupled model for transport of multiple chemical species and kinetic precipitation/dissolution reactions with applications to reactive flow in single phase hydrothermal systems. *American Journal of Science*, 294(5):529–592, 1994.
- S. Strand, D. C. Standnes, and T. Austad. Spontaneous imbibition of aqueous surfactant solutions into neutral to oil-wet carbonate cores: Effects of brine salinity and composition. *Energy & fuels*, 17(5):1133–1144, 2003.
- S. Strand, E. J. Høgnesen, and T. Austad. Wettability alteration of carbonates—Effects of potential determining ions (Ca^{2+} and SO_4^{2-}) and temperature. *Colloids and Surfaces A: Physicochemical and Engineering Aspects*, 275(1-3):1–10, 2006.
- K. Stüben. Algebraic multigrid (AMG): An introduction with Applications. *GMD Report 70*, 1999.
- K. Stüben. A review of algebraic multigrid. *Journal of Computational and Applied Mathematics*, 128:281–309, 2001.
- K. Stüben and T. Clees. SAMG user’s manual, 2005.
- A. M. Tartakovsky and S. P. Neuman. Effects of Peclet number on pore-scale mixing and channeling of a tracer and on directional advective porosity. *Geophysical Research Letters*, 35(21):L21401, 2008.

- A. M. Tartakovsky, P. Meakin, T. D. Scheibe, and R. M. Eichler West. Simulations of reactive transport and precipitation with smoothed particle hydrodynamics. *Journal of Computational Physics*, 222(2):654–672, 2007a.
- A. M. Tartakovsky, A. L. Ward, and P. Meakin. Pore-scale simulations of drainage of heterogeneous and anisotropic porous media. *Physics of Fluids*, 19:103301, 2007b.
- P. G. Tucker, C. L. Rumsey, P. R. Spalart, R. E. Bartels, and R. T. Biedron. Computations of wall distances based on differential equations. *AIAA journal*, 43(3):539–549, 2005.
- S. Unverdi and G. Tryggvason. A front-tracking method for viscous, incompressible, multi-fluid flows. *Journal of Computational Physics*, 100(1):25–37, 1992.
- M. I. J. van Dijke and K. S. Sorbie. Three-phase capillary entry conditions in pores of noncircular cross-section. *Journal of Colloid and Interface Science*, 260(2):385–397, 2003.
- M. I. J. van Dijke and K. S. Sorbie. Existence of fluid layers in the corners of a capillary with non-uniform wettability. *Journal of Colloid and Interface Science*, 293(2):455–463, 2006.
- R. Wagner, M. Kühn, V. Meyn, H. Pape, U. Vath, and C. Clauser. Numerical simulation of pore space clogging in geothermal reservoirs by precipitation of anhydrite. *International Journal of Rock Mechanics and Mining Sciences*, 42(7):1070–1081, 2005.
- T. W. Willingham, C. J. Werth, and A. J. Valocchi. Evaluation of the effects of porous media structure on mixing-controlled reactions using pore-scale modeling and micromodel experiments. *Environ. Sci. Technol*, 42(9):3185–3193, 2008.
- M. Wolf, O. Bretkopf, and R. Puk. Solubility of calcite in different electrolytes at temperatures between 10 and 60 °C and at CO₂ partial pressures of about 1 kPa. *Chemical geology*, 76(3-4):291–301, 1989.
- K. Wu, N. Nunan, J. W. Crawford, I. M. Young, and K. Ritz. An efficient Markov chain model for the simulation of heterogeneous soil structure. *Soil Science Society of America Journal*, 68(2):346, 2004.

- K. Wu, M. I. J. van Dijke, G. D. Couples, Z. Jiang, J. Ma, K. S. Sorbie, J. Crawford, I. Young, and X. Zhang. 3D Stochastic Modelling of Heterogeneous Porous Media—Applications to Reservoir Rocks. *Transport in Porous Media*, 65(3):443–467, 2006.
- K. Wu, Z. Jiang, J. Ma, G. Couples, M. I. J. van Dijke, and K. S. Sorbie. Multiscale pore system reconstruction and integration. In *International Symposium of the Society of Core Analysts*, 2011.
- H. Xia and P. G. Tucker. Finite volume distance field and its application to medial axis transforms. *International Journal for Numerical Methods in Engineering*, 82(1):114–134, 2010. ISSN 1097-0207.
- R. Xu, S. Luo, and P. Jiang. Pore scale numerical simulation of supercritical CO₂ injecting into porous media containing water. *Energy Procedia*, 4: 4418–4424, 2011.
- J. Yao, J. F. Thovert, P. M. Adler, V. N. Burganos, A. C. Payatakes, J. C. Moulou, and F. Kalaydjian. Characterization, reconstruction and transport properties of Vosges sandstones. *Revue-Institut Francais du Petrole*, 52:3–22, 1997.
- H. O. Yildiz and N. R. Morrow. Effect of brine composition on recovery of Moutray crude oil by waterflooding. *Journal of Petroleum Science and Engineering*, 14(3-4):159–168, 1996.
- H. Yoon, A. J. Valocchi, C. J. Werth, and T. Dewers. Pore-scale simulation of mixing-induced calcium carbonate precipitation and dissolution in a microfluidic pore network. *Water Resources Research*, 48(2):W02524, 2012.
- A. Yousef, S. Al-Saleh, A. Al-Kaabi, and M. Al-Jawfi. Laboratory Investigation of Novel Oil Recovery Method for Carbonate Reservoirs. In *Canadian Unconventional Resources and International Petroleum Conference*, 2010.
- P. Zhang and T. Austad. Waterflooding in chalk: Relationship between oil recovery, new wettability index, brine composition and cationic wettability modifier. SPE-94209. In *SPE Europe/EAGE Annual Conference*, 2005.

- P. Zhang, M. T. Tweheyo, and T. Austad. Wettability alteration and improved oil recovery by spontaneous imbibition of seawater into chalk: Impact of the potential determining ions Ca^{2+} , Mg^{2+} , and SO_4^{2-} . *Colloids and Surfaces A: Physicochemical and Engineering Aspects*, 301(1-3): 199–208, 2007.
- T. X. Zhou and M. F. Feng. A least squares Petrov-Galerkin finite element method for the stationary Navier-Stokes equations. *Mathematics of Computation*, 60(202):531–543, 1993.

